

RATE EQUATION ANALYSIS OF NANOCRYSTAL-ENHANCED UPCONVERSION IN NEODYMIUM-DOPED GLASSES

DISSERTATION

zur Erlangung des
Doktorgrades der Naturwissenschaften (Dr. rer. nat.)
der

Naturwissenschaftlichen Fakultät II
der Martin-Luther-Universität
Halle-Wittenberg



vorgelegt

von Herrn Dipl.-Phys. (Med.) Hans Ulrich Skrzypczak
geb. am 17.12.1984 in Stralsund

Hans Ulrich Skrzypczak: *Rate Equation Analysis of Nanocrystal-Enhanced Up-conversion in Neodymium-doped Glasses*, Dissertation,
Halle (Saale), © July 2014.

REVIEWERS

1. PD Dr. Gerhard Seifert, Martin-Luther-Universität Halle-Wittenberg, Germany
2. Dr. Jan Christoph Goldschmidt, Fraunhofer ISE, Freiburg, Germany
3. Prof. Grant V. M. Williams, Victoria University Wellington, New Zealand

DEFENCE

This work was defended on 17 April 2015 in Halle (Saale).

ABSTRACT

A remarkable increase of photoluminescence from neodymium arises from the growth of hexagonal BaCl_2 nanocrystals in fluorozirconate-based glasses. A rate equation model is introduced to describe the excitation and relaxation dynamics in this material system comprehensively. The enhancement mechanisms due to the nanocrystals are analysed with a focus on their impact on the upconversion of near-infrared photons to the visible spectral range. After validating the description of Stokes and Anti-Stokes processes with a range of selective experiments considering the time-, power- and concentration dependence, the model is used to make a prediction on the feasibility of an upconverting bottom-layer below a bifacial solar cell. Such device may be used to convert the near-infrared fraction of the solar spectrum transmitted by a silicon solar cell to wavelengths that can contribute to the photoelectric conversion. Neodymium-doped glasses and glass ceramics turn out to be particularly interesting upconverting layers because of neodymium's electronic structure that allows for a broadband absorption of the solar near-infrared.

KURZBESCHREIBUNG

Das Wachsen von hexagonalen BaCl_2 -Nanokristallen in Fluorozirkonatbasierten Gläsern führt zu einer drastischen Steigerung der Photolumineszenz des darin eingebetteten Neodyms. Ein Ratengleichungssystem wird entwickelt, um die Anregungs- und Relaxationsdynamik auf ein Modell abzubilden. Die durch die Nanokristalle bedingten Verstärkungsmechanismen werden hinsichtlich ihres Einflusses auf die Hochkonversion von nahinfraroten Photonen in den sichtbaren Spektralbereich analysiert. Nachdem die korrekte Beschreibung der Stokes- und Anti-Stokes-Prozesse mittels verschiedener selektiver Experimente nachgewiesen ist, wird das Modell dazu genutzt, um eine Vorhersage für die Nutzbarkeit einer hochkonvertierenden Schicht unter einer bifazialen Solarzelle zu machen. Ein solches System kann genutzt werden, um den nahinfraroten Anteil des Sonnenlichts, der gewöhnlich durch eine Solarzelle durchgelassen wird, zu Wellenlängen zu konvertieren, die zur photoelektrischen Konversion beitragen können. Es stellt sich heraus, dass insbesondere neodym-dotierte Gläser und Glaskeramiken als hochkonvertierende Schichten interessant sein könnten, da die elektronische Struktur von Neodymium eine breitbandige Absorption des nahinfraroten Sonnenlichts ermöglicht.

CONTENTS

1	INTRODUCTION	1
1.1	Aim of this work	1
1.2	Map of this work	2
2	PHYSICAL SETTING	5
2.1	Introduction and state of the art	5
2.2	Neodymium as technological material	8
2.3	Glassy hosts for neodymium	9
2.3.1	Sample preparation	10
2.3.2	Observation of crystal growth by X-ray diffraction	11
2.4	Optical spectroscopy	13
2.4.1	Absorption spectroscopy	14
2.4.2	Emission spectroscopy	19
2.4.3	Spectral characterization of broadened lines	26
2.5	Discussion	28
2.5.1	Origin of emission increase	28
2.5.2	Spectral identification of transitions	29
2.5.3	Order of Anti-Stokes population mechanisms	29
2.5.4	Linewidths and spectral overlaps	32
2.6	Summary	33
3	EINSTEIN COEFFICIENTS FOR SPONTANEOUS EMISSION	35
3.1	Judd-Ofelt theory for effective refractive index medium	35
3.1.1	Overview of Judd-Ofelt theory in glass and glass ceramics	35
3.1.2	Determination of intensity parameters	36
3.1.3	Calculation of radiative properties	38
3.2	Results	39
3.2.1	Oscillator strengths	39
3.2.2	Intensity parameters	41
3.2.3	Einstein coefficients	42
3.3	Experimental verification of Judd-Ofelt results	44
3.3.1	Overview	44
3.3.2	Photoluminescence lifetime measurements	45
3.3.3	McCumber theory and Füchtbauer-Ladenburg-Equation	46
3.4	Discussion	48
3.4.1	Nanocrystal growth and inclusion of neodymium	48
3.4.2	On Judd-Ofelt accuracy and error margins	52
3.5	Summary	54
4	RATE EQUATION MODEL - STOKES PROCESSES	57
4.1	Modelling Stokes processes with rate equations	57
4.1.1	Spontaneous emission	58
4.1.2	Processes involving phonons	59
4.1.3	Ground state absorption	62
4.2	Comparison with experimental photoluminescence decays	63
4.2.1	Stokes emissions under the influence of glass phonons	65

4.2.2	Stokes emissions in the glass ceramics	67
4.3	Discussion	68
4.3.1	Influence of Einstein coefficients	68
4.3.2	Nanocrystal influence on Stokes emissions	70
4.3.3	Evaluation of effective-medium model	72
4.3.4	Coefficients for phonon emission and absorption	74
4.4	Summary	75
5	RATE EQUATION MODEL - ANTI-STOKES PROCESSES	77
5.1	Modelling Anti-Stokes emissions	77
5.1.1	Excited-state absorption	78
5.1.2	Ion-ion interactions	80
5.2	Simulation of continuous-wave excitation	82
5.3	Comparison to experimental upconversion spectra	85
5.3.1	Estimation of experimental photon flux	85
5.3.2	Continuous infrared laser excitation	86
5.4	Discussion	87
5.4.1	Population mechanisms	87
5.4.2	Nanocrystal influence	90
5.4.3	Summary	93
6	CONVERSION OF SOLAR RADIATION	95
6.1	Motivation	95
6.2	Broadband excitation	96
6.2.1	Overlaps in steady-state neodymium	96
6.2.2	Modelling broadband continuous NIR excitation	97
6.2.3	Concentration-dependent solar upconversion yield	98
6.3	Discussion	99
6.3.1	Interpretation of the results	99
6.3.2	Comparison of neodymium with other rare earths	100
6.3.3	Conclusions for neodymium in glass and glass ceramics	103
6.3.4	Impact of the host properties	104
6.3.5	Optimisation of composition	104
6.3.6	Optimisation of Temperature	106
6.4	Summary	108
7	SUMMARY	111
	APPENDIX	115
A	DETAILS	115
A.1	Equation system	115
A.2	Laser parameters	117
A.2.1	Determination of beam waists from beam profiling	117
A.2.2	Pulse durations: FROG	117
A.2.3	Control of repetition rate with frequency division	119
A.3	Theoretical details	120
A.3.1	Metastable level branching ratios	120
A.3.2	Conversion of electric signals to experimental photon flux	121
A.4	Error estimation	122
A.4.1	Errors in volume fraction	122
	BIBLIOGRAPHY	125

1 | INTRODUCTION

1.1 AIM OF THIS WORK

The discovery of the rare earths (RE) commenced during the end of the 18th century with yttrium and lasted until the middle of the 20th century when promethium was found to complete the list of strange metals. Since then, a broad technological scope of these materials has emerged encompassing applications in metallurgical alloys, in strong magnets, as chemical catalysts and as converters of radiation.

In particular, RE doped glasses may be used to make the solar infrared radiation normally unexploited by silicon solar cells available to them with the help of optical upconversion. Embedded into a bottom layer below a bifacial solar cell, this unused fraction of the sunlight is upconverted to photon energies above the silicon bandgap and reflected back to the cell. This particular technological aspect will be further investigated in this work.

The wide diversity of technological applications in general is due to the RE's peculiar spectroscopic properties: Their 4f orbitals, among which the optical transitions occur, are effectively screened by the higher lying 5s-, 5p-, or even 6s-orbitals. When embedded into a host matrix, the originally forbidden electric dipole transitions among electronic states become partially allowed by the crystal field of the host. Still, the radiative transition probabilities remain low calling for a photon management to ensure efficient emission.

Increasing emission means manipulation of the photoactive ion such that the spectroscopic lifetimes increase. These comprise of the sum of the radiative emission rate A_{rad} and all individual loss probabilities W_i ,

$$\frac{1}{\tau} = A_{\text{rad}} + \sum_i W_{i,\text{nonrad}}.$$

Hence, to achieve long luminescence lifetimes, the probabilities for nonradiative losses have to be minimised. The primary loss mechanisms of excitation for RE ions are phonon emission and ion-ion interactions such as energy transfer. While the latter is a consequence of the doping itself, losses to the matrix are defined by the kind and strength of the coupling of the excited electrons to the phonons of the host.

The key parameter for the description of phonon losses is the cut-off phonon frequency. The maximum energy phonons govern the decay because they are associated to the process that involves the least number of phonons to be emitted simultaneously. Several glasses already have low cut-off phonon energies. One example with a particularly low cut-off energy of 580 cm^{-1} [1-3] is ZBLAN. It is of the form $\text{ZrF}_4-\text{BaF}_2-\text{LaF}_3-\text{AlF}_3-\text{NaF}$ [4] and part of the heavy-metal-fluoride-glass (HMFG) family that was first described in 1975 by M. Poulain *et al.* [5]. In addition to their favourable phonon spectrum, they feature a relatively low refractive index, transparency over a

broad wavelength range, and low melting temperatures. Also, these glasses are relatively stable and their ingredients comparably cheap.

RE ions have already proven to emit efficiently, when embedded into ZBLAN glasses [6–8]. However, in the case of neodymium most of the research pursued the properties of the laser level ${}^4F_{3/2}$ that is characterised by its slow and exclusively radiative decay. Other technologically interesting transitions have not received much attention as their radiative decay rate is often smaller than that of phonon emission by several orders of magnitude. To make use of these emissions in technologies including photovoltaic upconversion, the host must be configured for the realisation of the lowest phonon emission probability possible [9]. Most notably, the introduction of hexagonal BaCl_2 nanocrystals into neodymium-doped ZBLAN-based glasses has shown to significantly improve the emission intensity of these levels [10, 11]. The enhancement is assigned to a fractional inclusion of the neodymium into the nanocrystals, which is associated to a coupling to its uniquely low phonon energies of 220 cm^{-1} [12, 13].

Most research towards photovoltaic upconversion focused on the RE erbium, which also showed advantageous emission properties in ZBLAN [14–16]. However, erbium does not enter the nanocrystals [17] and is also naturally limited to monochromatic upconversion due to its electronic structure. This turns out to be a constraint to upconversion of broadband solar radiation. Neodymium on the other hand, has several nearly equally spaced energy levels. Embedded into an amorphous host with significant inhomogeneous line broadening, such as fluorozirconate glasses or glass ceramics, it may be able to convert broad distributions of nearly the whole near-infrared part of the sunlight.

On this basis two targets are set for this work:

1. Develop a quantitative model for the optically excited electronic dynamics of neodymium embedded into ZBLAN-based glasses and glass ceramics. The parameter sets involved have to be proven by selective experiments.
2. Simulate an upconverting bottom layer for broadband, near-infrared sunlight, based on neodymium-doped glasses and glass ceramics. Use the model in order to evaluate possible advance material optimisations.

1.2 MAP OF THIS WORK

The work is divided into six thematically separated chapters:

PHYSICAL SETTING This chapter gives an introduction to neodymium and its incorporation into the glasses and glass ceramics. This includes the observation of nanocrystal growth and their size determination. Experimental evidence for the positive nanocrystal effect on photoluminescence is presented with spectroscopic measurements that are characterised in the view of the neodymium energy level structure. After the population routes for regular and upconversion excitation are established, spectroscopic base data is gathered for use in the rate equation model.

EINSTEIN COEFFICIENTS FOR SPONTANEOUS EMISSION The parameters for spontaneous emission describe the intrinsic decay probability of RE ions. They are determined with the Judd-Ofelt (JO) theory that exploits the weak effect of the host on the RE. In addition to the parameter calculation, the analysis quantitatively describes the matrix alteration upon nanocrystal growth using the RE ion as a probe for the remaining weak host influence. The analysis concludes with the verification of several JO results with complementary experiments and a discussion of the JO accuracy.

RATE EQUATION MODEL – STOKES PROCESSES The scope of this chapter is the development of a rate equation system to model the electronic dynamics in neodymium embedded into ZBLAN-based glasses and glass ceramics. At this point it is limited to Stokes-type emissions, i. e. to wavelengths longer than that of the excitation. For this, Einstein coefficients from the previous chapter and nonradiative parameters from the literature are involved. While spontaneous emission is almost independent from host influence, the hereby introduced phonon relaxation channels are not. The description of neodymium in glass is extended to glass ceramics with an effective-medium approach. The model is verified by comparing simulated decays to time-resolved photoluminescence measurements on weakly doped samples.

RATE EQUATION MODEL – ANTI-STOKES PROCESSES Having established the model and the coefficients needed to describe Stokes-type photoluminescence, this chapter moves on to the extension to Anti-Stokes processes, i. e. processes leading to emissions at wavelengths shorter than the excitation. Ion-ion interactions and excited-state absorption are introduced, both of which are responsible for upconversion. Keeping the Stokes parameters fixed, the model is extended in a self-consistent fashion. The power-dependence of the simulated stationary states are compared with power-dependent upconversion spectra from continuous laser excitation at high neodymium doping levels. The discussion identifies the governing processes and analyses the nanocrystal influence on upconversion. The limitations of the rate equation description are set into a context of the results.

CONVERSION OF SOLAR RADIATION The previous chapters were focused on the development of the rate equation model and its experimental verification. Now, the model is used to give a prognosis on the usability of a neodymium-doped glass or glass ceramic as an upconverting bottom layer under a bifacial solar cell. Sunlight with wavelengths reaching beyond the silicon bandgap (>1100 nm) is normally lost from the photoelectric conversion and merely transmits the solar cell. The simulation describes how an upconverting layer below the cell converts this near-infrared light up to wavelengths above the bandgap (<1100 nm). The prognosis estimates an additional photon flux of around 2% using the glass ceramics. On this foundation it is discussed perspectively, how the material parameters may be engineered or the environmental parameters be chosen to optimise the conversion efficiencies.

The summary briefly recaps the results and motivates further research.

2 | PHYSICAL SETTING

A rate equation system is developed to evaluate the feasibility of a neodymium-based glass (-ceramic) upconverter. This chapter gathers related work from the literature. Furthermore, physical information and measured data are compiled that form the basis of the subsequent model assembly. This includes relevant optical parameters of neodymium and the glass (ceramic).

2.1 INTRODUCTION AND STATE OF THE ART

SPECTRAL MISMATCH The research field of spectral conversion of sunlight gathered a lot of attention lately. Since conventional solar cells can only effectively convert photons to electricity, whose energies is closely above the band gap, significant efficiency drawbacks exist with regard to the wide spectral distribution of photons in the sunlight [18, 19].

Photons exceeding the energy of the band gap are absorbed and converted to charge carriers generating an electric current. The excess energy $E_g - \hbar\omega$ is lost as kinetic energy of the carriers and converted to heat. These so-called thermalization losses can be a significant part of the total losses in the cell [19, 20]. On the other hand, photons with energies below the band gap are not absorbed. For a crystalline silicon solar cell this means that the part of the sunlight with wavelengths longer than around 1100 nm (corresponding to an energy of roughly 1.1 eV), which equals about 20 % of the total integrated solar spectral irradiance¹ (around 180 W/m^2), is immediately lost and merely passes the cell, which appears transparent for this light.

SPECTRAL CONVERSION One technological avenue to the spectral mismatch problem is the conversion of above- or below-bandgap photons with a down- or upconverter, respectively. Downconverters generally absorb the short-wavelength light and convert it to near-bandgap photons, ideally just above the bandgap. Several investigations on downconverters can be found in the literature [21–25]. However, downconversion is not within the scope of this work, which on upconversion. A solar upconverter [26, 27] absorbs photons from the near-infrared part of the sunlight below 1100 nm. After a certain time, determined by the electronic structure and the host material, it converts the excitation energy of two or more of them into one photon in the visible spectral range. Ideally, the resulting photon carries an energy just above the band gap with little excess energy being lost. For different solar cell materials with different bandgaps the situation extends accordingly, for example amorphous silicon with a bandgap at around 1.8 eV (around

¹ The total integrated solar spectral irradiance is called *solar constant* and has a value of around 1.37 kW/m^2 .

700 nm, for a-Si:H) [19]. For photovoltaic applications, Trupke *et al.* evaluated the possibility of a significant improvement of solar cell performance, when the cell is equipped with an upconverter device [26].

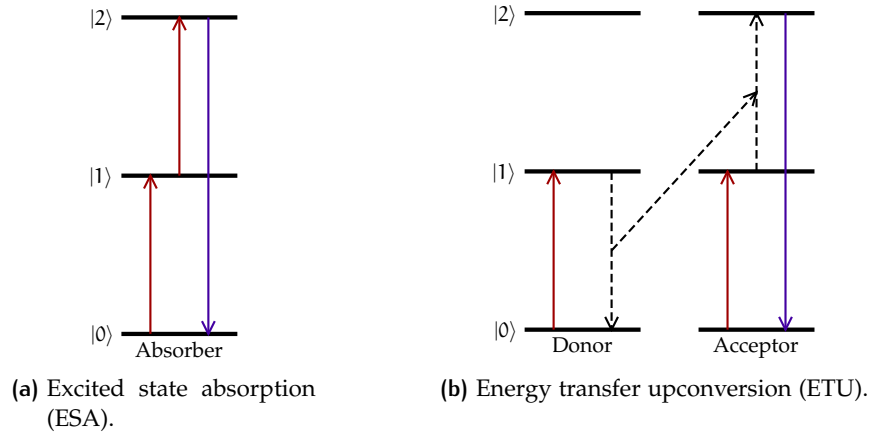


Figure 2.1: Upconversion mechanisms in RE ions. Adapted from Ref. [28].

The effect of upconversion in general was first demonstrated by Bloembergen in 1959 for application in „Solid State Infrared Quantum Counters” [29]. It was focused exclusively on the sequential absorption of these photons, involving an intermediate excited state (ESA), as shown in Fig. 2.1a. The second main upconversion mechanism is based on a direct electric-dipole interaction between two (or more) ions. It is called energy transfer upconversion (ETU) and was found years later [30]. Here, an excited ion (donor) transfers its energy to another excited ion (acceptor) finally carrying the sum energy (see Fig. 2.1b). There are other mechanisms for photon upconversion such as photon avalanche and nonlinear optical effects including the simultaneous absorption of several photons, called multiphoton absorption. However, these are not efficient under the external conditions inherent to regular photovoltaics (intensity and distribution of sunlight, etc.) and hence, this work focuses only on the main mechanisms, ESA and ETU.

LANTHANIDE UPCONVERSION Upconversion was found to be most efficient in lanthanide ions aiming at a lot of different technological fields besides photovoltaics [28, 31–35] including both biological and medical applications [36–41], upconversion lasers [42, 43], or 3D-displays [44]. The reason is the general upconversion requirement of long-lived persistence of the primary excitation energy before spontaneous decay. The energy has to be stored long enough in an intermediate state until the second excitation step may proceed from there adding up the individual energies. In rare earth (RE) ions such as erbium, ytterbium or neodymium, optical transitions take place between 4f-states of the ions. These are forbidden by several selection rules, among which Laporte’s rule is particularly important. It states that during any transition, no change in parity may occur between initial and final 4f-state. This rule is partially lifted by the crystal field that the host matrix applies to the RE ion. Further important selection rules are $\Delta J \leq 6$, $\Delta S = 0$, and $\Delta L \leq 6$ [45]. As a consequence, RE transitions have low probabilities, which translates to long-lived states, as long as no loss channels drain their population.

CHOICE OF AN OPTIMAL HOST However, as the relaxation of the selection rules strongly depends on the crystal field, the choice of the optimal host material must proceed carefully. A suitable host must not only show a good RE solubility, high transparency over all relevant spectral ranges, it must rather also be stable and cheap. But most importantly, its phonon spectrum must be such that excitation losses to thermal energy of the host are minimal.

In a review of host materials for upconverting RE ions, Strümpel *et al.* showed that BaCl_2 might be a particularly beneficial host [46]. However, although crystals including BaCl_2 give good conversion results, they only partially fulfil the other criteria. In particular, crystals are usually unstable under atmospheric conditions, brittle, comparably expensive and complex to manufacture [11, 47]. Optical glasses, on the other hand, are cheap, stable and easy to produce. The site-to-site variations in glasses induce strong line broadening, while in crystals, only narrow bands exist. Glasses based on the ZBLAN composition [4] are transparent over a broad wavelength window, show good RE solubility and feature the important low maximum phonon energies that are required for efficient emission of the upconverted excitation energy. This is the reason, upconversion with a ZBLAN host attracted a lot of attention and in particular erbium-based (fiber) lasers [42, 48–50] and photovoltaic upconverters [14–16]. The maximum phonon energy of about 580 cm^{-1} in ZBLAN [12, 51] however, is still not as low as that in BaCl_2 suggested by Strümpel *et al.* [46].

The idea of implementing BaCl_2 nanocrystals into ZBLAN glasses, to profit from the beneficial properties of both, was initially pursued with the focus on X-ray storage phosphors [52, 53]. The uniform growth of BaCl_2 nanocrystals was shown inside a ZBLAN-derived fluorochlorozirconate matrix with favourable effect on europium luminescence therein. However, this luminescence enhancement requires the inclusion of the RE into the nanocrystals. Until now, the inclusion of erbium into BaCl_2 nanocrystals was not fully accomplished [17]. However, a dramatic increase in photoluminescence accompanied by hints at nanocrystal inclusion were found for neodymium ions embedded into ZBLAN-based glasses with BaCl_2 nanocrystals [10, 11]. On the other hand, the idea of a monochromatic upconversion scheme in neodymium appears unlikely as the upconversion step is at 800 nm and already above the band gap of c-Si solar cells. Also, the main emissions at 870 nm and 1050 nm in ZBLAN appear unsuitable for narrow-bandwidth upconversion of 800 nm light. For this, erbium is the ideal choice as its ladder structure features three to four almost equal energy steps into the visible spectral range, viable for photons of either 1.54 μm or 980 nm. Conversion of sunlight with erbium has been demonstrated experimentally with 20 mol % inside NaYF_4 [54], which leads to a 2.5 % increase of the external quantum efficiency (EQE) [19].

BROADBAND ILLUMINATION Nonetheless, for continuous, broadband illumination, for example with sunlight, the situation may be different. Due to the continuous irradiation, the RE ion reaches a stationary state where all states become more or less populated. When multiple levels are populated for longer times, ESA and ETU take place not only upon monochromatic excitation implied by the equally spaced ladder system mentioned above for erbium. Rather, they proceed at any wavelength that corresponds to any of the $\binom{N}{2}$ energy differences between N states available in the RE

level scheme. The only precondition is the availability of suitable pump wavelengths in the near-infrared part of the sunlight. This is met for several RE ions and especially for neodymium. In addition, the neodymium level scheme features several low lying energy levels with comparably small interlevel spacing and a comparably small gap below the main emission level. Details on these favourable properties are discussed later in this work.

ZBLAN is a suitable host for neodymium embedment as the huge line broadening extends the spectral absorption range of upconversion. Moreover, neodymium takes advantage of the beneficial phonon spectrum of BaCl₂ nanocrystals within ZBLAN glass ceramics.

MODELLING OF UPCONVERSION The model description of erbium- and neodymium-based upconversion has been established thoroughly by Pollnau *et al.* [55–58] and Bogdanov *et al.* [50, 59–61]. In their exhaustive studies, aspects of upconversion such as its power dependence are covered. However, no rate equation model of a glass ceramic or broadband illumination appears in the literature, although for both, experimental studies on similar systems do exist [62–64]. A rate equation model of broadband upconversion with a neodymium-doped glass ceramic with BaCl₂ nanocrystals is the focus of this work.

2.2 NEODYMIUM AS TECHNOLOGICAL MATERIAL

OVERVIEW The metal neodymium was discovered by Auer von Welsbach in 1885 [65]. Its name originates from the ancient Greek words *neos* and *didymos* and means something like „new twin“ [66]. The overall history of its discovery can be found in a detailed review [67]. Neodymium is the second-most abundant of the lanthanides (after Ce) and is found more than ten times more often on the earth’s crust than erbium or europium [66, 68]. In the periodic table of elements ⁶⁰Nd is located between praseodymium (₅₉Pr) and promethium (₆₁Pr).

The electronic configurations of the neutral lanthanides [69] are all based on the xenon structure (1s²2s²2p⁶3s²3p⁶3d¹⁰4s²4p⁶4d¹⁰5s²5p⁶). Neutral neodymium (Nd-I) features two outer electrons (6s²) above the following 4f⁴ shell. In its triply ionized (Nd-IV) form [Xe]4f³, three electrons are missing. Whenever the word *neodymium* is used further in this work, it shall refer to the triply ionized form. Due to the contraction of its eigenfunctions, the f shell becomes an inner shell enclosed by the 5s²5p⁶ orbitals. The resultant screening of the f electrons from external fields leads to their rather weak interactions with the local environment.

PRODUCTION AND ENVIRONMENTAL ISSUES Neodymium is industrially extracted from monazite² and bastnasite³ sands as well as from mischmetal, a naturally occurring alloy of REs, comprised of large amounts of Ce and La, together with Nd, Pr, and Sm. The extraction methods are hydro- and electrometallurgic [68]. The separation processes are rather complex for all

² (Ce,La,Th,Nd,Y)PO₄

³ (Ce,La,Th,Nd,Y)(CO₃)F

REs due to their chemical similarity, and caused severe environmental damage in the production countries (mostly China) in the past [68]. Damage especially arises from the produced dust, waste-rock, ore stockpiles, and waste water, all of which may be toxic, radioactive and potentially harmful in different ways. Due to the RE market mindshare however, careful and ecologically sensitive extraction methods or even RE recycling strategies are, unfortunately, nowadays still no common practice yet.

APPLICATIONS Nonetheless, neodymium is one of the most important high-technology materials. Already used as pigment in glasses since as early as 1927 by Moser [70], neodymium became most famous for its application in high-power magnets. Implementation into an alloy together with boron and iron produces the strongest permanent magnets available today. Such strong magnets are then used in massive amounts in wind turbines and electromobiles, but also in audio systems and computer hard drives. There is also widespread use as chemical catalyst, for example in fluid-fracking or even in fertilizers [68]. The most important optical technology however, is the use of neodymium as the active ion in solid-state lasers. Nd:YAG-based lasers are among the most frequently sold laser systems. On the other hand, terawatt lasers on the basis of Nd:glass are employed for inertial confinement fusion [71].

This work focuses on the optical properties of neodymium that are related to upconversion photoluminescence.

2.3 GLASSY HOSTS FOR NEODYMIUM

The formation of hexagonal BaCl_2 inside a fluorochlorozirconate (FCZ) precursor glass (illustrated in Fig. 2.2) was accomplished with a special thermal treatment procedure. These nanometric crystals form from the chlorine added to the FCZ with respect to the fluorozirconate base glass (FZ). Transmission electron microscopy images from similar samples can be found in Refs. [52, 53]. Depending on the treatment temperature, the size of the

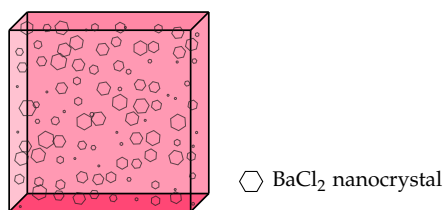


Figure 2.2: Neodymium-doped fluorochlorozirconate glass ceramic containing BaCl_2 nanocrystals. The hexagonal BaCl_2 was grown by thermal treatment of the fluorochlorozirconate precursor glass.

generated nanocrystals can be controlled within a certain range. For comparison, one untreated FCZ precursor glass, and one FZ glass were kept. The samples are (co-)doped with different percentages of neodymium. The residual effect of the crystal field on its optical properties make it a probe for alterations of the host matrix. There are also hints that neodymium aids nanocrystal formation as a nucleating seed in glass ceramics [62].

2.3.1 Sample preparation

The samples [10–12] subject to this analysis belong to the class of FCZ glasses and are $(53-x)\text{ZrF}_4-10\text{BaF}_2-10\text{BaCl}_2-(20-x)\text{NaCl}-x\text{KCl}-3.5\text{LaF}_3-3\text{AlF}_3-0.5\text{InF}_3-x\text{NdF}_3$ (all coefficients in mol %), where the doping level is specified by x . This composition is the same as for the FZ base glass $(52-x)\text{ZrF}_4-20\text{BaF}_2-20\text{NaF}-3.5\text{LaF}_3-3\text{AlF}_3-0.5\text{InF}_3-x\text{NdF}_3$, but received additional chloride at the expense of fluoride. This is a requirement for the later nanocrystal formation therein [10, 11]. Additional KCl fixes uncompensated charges. The chemical composition of all samples is summarised in Table 2.1, which also includes the specific sample abbreviations. While the FZ1 samples and the FCZ1 sample were doped with 1 mol % neodymium, series FCZ5 features a content of 5 mol %.

The ingredients were melted in a glassy carbon crucible at a temperature of 745 °C under a chemically inert atmosphere. The cast was then poured into a mold of brass, prepared at a temperature of 200 °C. This is below the glass temperatures of the FCZ glass $T_g(\text{FCZ}) = 210$ °C [10] and the FZ glass $T_g(\text{FZ}) = 260$ °C [11, 48], respectively. There it was left to cool down to room temperature. Subsequently, the cut and polished samples were heat treated at temperatures between 240 °C and 290 °C for a duration of 20 min under an inert atmosphere.

Differential scanning calorimetry has shown a BaCl_2 crystallization peak centred at $T_c = 260$ °C [10]. This temperature range was therefore chosen for the annealing temperatures. Whenever the abbreviation FCZ-c is further mentioned during this work referring to a single sample, it means the sample heat treated at 260 °C. In addition, XRD measurements clearly show BaCl_2 peaks starting from around 240 °C as discussed later in section 2.3.2. The upper treatment temperature was limited by the onset of partial glass crystallization and the phase change of the hexagonal BaCl_2 symmetry to the more stable orthorhombic phase [6, 10].

Table 2.1: Sample compositions (all values in mol %).

	FZ1	FCZ1	FCZ5
AlF_3	3.0	3.0	3.0
LaF_3	3.5	3.5	3.5
BaCl_2	0.0	10.0	10.0
BaF_2	20.0	10.0	10.0
NaF	20.0	0.0	0.0
NaCl	0.0	19.0	15.0
InF_3	0.5	0.5	0.5
ZrF_4	52.0	52.0	48.0
KCl	0.0	1.0	5.0
NdF_3	1.0	1.0	5.0

Based on this procedure, different glass series were prepared with different doping concentration [10–12]. During the preparation of the sample series, special attention was paid to achieve high optical quality by using only recently ordered, highly pure and finely powdered materials. Avoidance of inclusions and bubbles was attempted by using a fast pour out method. The visual appearances of the as-made, i. e. not thermally treated glasses,

and the samples heat treated at 240 °C to 270 °C were transparent. At temperatures of 280 °C and 290 °C the samples became milky white, while the FZ1 reference glass did not. For optical measurements the samples were polished to optical quality.

2.3.2 Observation of crystal growth by X-ray diffraction

SCHERRER METHOD Size determination of nanometric crystals is usually carried out on the basis of the Scherrer method [72], where elastic scattering of X-radiation at the periodic lattice planes of crystals is used for structural analysis with the help of the Bragg condition. For a sample containing a distribution of nanocrystal sizes this method yields an ensemble average information [73].

X-ray diffractometry (XRD) was performed here using copper K_{α} radiation⁴ with 40 kV at 40 mA. The Scherrer formula

$$d = \frac{K\lambda}{\Delta\vartheta \cos \vartheta} \quad (2.3.1)$$

connects the Bragg angle ϑ and the corresponding full-width at half-maximum $\Delta\vartheta$ to the size d of the crystal along the spatial direction of the reflection perpendicular to the lattice plane with Miller indices hkl . In Eq. (2.3.1) $\lambda = 1.5418 \text{ \AA}$ further denotes the X-ray wavelength. The crystallite-shape factor K was set to 0.9, as reported best approximation in absence of detailed shape information [74]. Possible stress or strain in the nanoparticles is also capable of significant line broadening. Such effects can not be fully excluded here, and hence multiple peaks were included into the analysis to remedy larger errors [73].

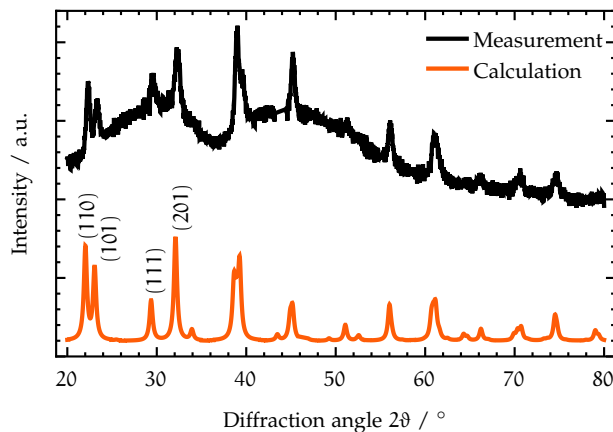


Figure 2.3: XRD spectrum of an FCZ-c glass ceramic containing 20 nm hexagonal BaCl_2 nanocrystals (black curve). These give rise to several sharp diffraction peaks that appear in addition to the broad background from the amorphous glass matrix, which is also responsible for the offset. The second graph (orange curve) shows a calculated XRD pattern for this case. The numbers in brackets are the hkl -indices of the single-peak lines used during the Scherrer analysis.

⁴ The Bruker AXS D8 Advance diffractometer was used.

NANOCRYSTAL IDENTIFICATION Figure 2.3 shows a typical XRD pattern of FCZ-c containing hexagonal BaCl_2 nanocrystals [75] (black curve). A simulation of the BaCl_2 XRD signal⁵ (orange curve) is also given in Fig. 2.3 (with crystallographic data from Refs. [13, 77]). The peaks are broadened as they stem from nanometric scatterers. In addition to the BaCl_2 peaks, the measurement graph in Fig. 2.3 also shows a broad background from the glassy (amorphous) part of the host matrix. Contributions to this background from the PMMA sample holder are already filtered.

A comprehensive study of the XRD patterns of the FCZ-c samples has been published [12]. It is shown that up to thermal treatment temperatures of 260 °C there are only diffraction peaks from hexagonal BaCl_2 . Also, their full-width at half-maximum is decreasing with treatment temperature, indicative of the nanocrystal growth [12]. Note that the line widths remain larger than the instrumental resolution. In the sample treated at 270 °C additional peaks appear and a mixed crystal phase comprised of both hexagonal and orthorhombic BaCl_2 is starting to manifest itself at this temperature [12]. In the samples with even higher treatment temperatures the phase transition from hexagonal (space group $\text{P}\bar{6}2\text{m}$ (189), ditrigonal dipyramidal) to orthorhombic (space group Pnma (62), orthorhombic bipyramidal) has been performed completely. Also, in the 290 °C sample the glass background starts to vanish, indicating an at least partial glass crystallization. As the intensity of several peaks decreases again there, the nanocrystals are believed to dissolve at such temperatures [7], which is also reflected in a slight decrease of the volume fractions of either of the crystalline BaCl_2 phases (see Ref. [75]). The correct assignment of the peaks to the correct phases was verified by also calculating mixed phases of orthorhombic and hexagonal as well as purely orthorhombic XRD patterns. These simulations are consistent to observations elsewhere [12] and the nanocrystal size dependence this work is based on [75].

NANOCRYSTAL VOLUME FRACTION The volume fraction δ_i of nanocrystals can be estimated from XRD measurements by dividing the area A_{peaks} under the crystalline peaks by the area A_{glass} under the total XRD graph including the broad background originating from the amorphous glass [78] as

$$\delta_i = \frac{A_{\text{peaks}}}{A_{\text{peaks}} + A_{\text{glass}}}.$$

The results start at approximately 15 % for the 240 °C sample, increase to their maximum of 20 % for the 260 °C sample and finally decrease again towards again 15 % for the 280 °C sample. Such values in the range of around 20 % for all 1 mol % samples [75] are comparable to values determined elsewhere [53]. This value is also the maximum possible volume fraction, as limited by the mole-fraction of BaCl_2 included into the samples (see Table 2.1). In Ref. [75] it is shown that the lower temperature samples have lower values indicating that not all Cl^- ions are used up to form BaCl_2 nanocrystals yet. The volume fraction is staying almost constant for higher treatment temperatures, while the particle sizes rise. This apparently shows that the nanoparticles initially grow independently at lower temperatures and that their further growth proceeds from the precipitation of the smallest [79].

⁵ Calculations were performed with the powder diffraction software *Powdercell* (2.4) [76].

LIMITATIONS OF THE SCHERRER METHOD The usual method of size determination on the basis of the Scherrer formula [72] often considers only the most intense reflection. This might be disadvantageous as the accuracy of a single-peak analysis is probably comparably low. Also, as XRD returns peaks only from isotropically crystalline structures without any common large scale defects, only a lower boundary of the average particle sizes can be obtained in that way. Furthermore, the assumption of spherically shaped particles is also often unjustified. As the single XRD reflection is related only to the extent along one particular spatial direction, for non-spherical nanometric crystals, it is uncertain how close the extent of the measured axis is to the average size [72, 74].

In order to achieve sufficient accuracy, the diffraction angles as well as the corresponding line widths were determined for several isolated peak (see Fig. 2.3). Subsequently, the resulting crystal sizes are averaged to obtain the mean particle size. These values must be treated as a lower boundary of the nanocrystal average size, since the crystal could have grown anisotropically or possibly with large crystal defects. Crystal clusters are also not correctly considered. Note further that analysis with the Scherrer formula is limited to nanoparticles smaller than 100 nm [74].

An alternative method for XRD-independent size determination of the nanocrystals based on Rayleigh scattering is shown in section 2.4.1.

RESULTS OF SIZE DETERMINATION Figure 2.4 shows the nanocrystal sizes obtained from X-ray diffraction and another method based on Rayleigh scattering as outlined later in section 2.4.1. The figure shows that after a slow

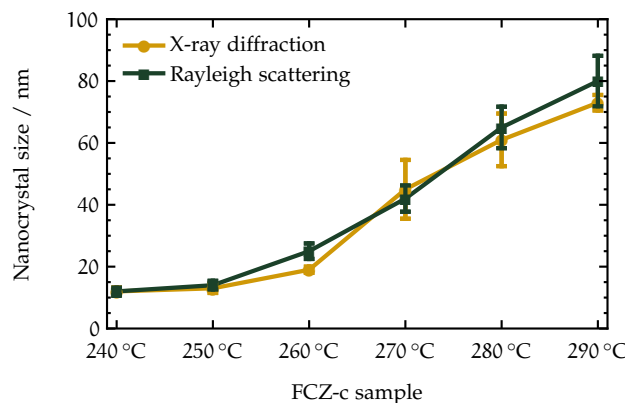


Figure 2.4: Results of nanocrystal size determination as deduced from X-ray diffraction and Rayleigh scattering (described in section 2.4.1).

nanocrystal growth for the lower treatment temperatures the slope of the graphs indicates a considerable change in growth speed. This apparently decreases again at the highest treatment temperatures.

2.4 OPTICAL SPECTROSCOPY

OVERVIEW This chapter presents, how absorption and emission spectroscopy were used during this work to determine the energy level positions

of neodymium embedded into a composite material, namely the FCZ-c glass ceramic. It is described how cross sections for ground-state absorption and emission are obtained. From the spectral data, the energy level scheme of neodymium in this host is established, the energy positions are collected, and transitions are identified in emission spectra. While the time dependence of the level population is discussed separately later in chapter 3 and chapter 4, it is already used here, together with regular and upconversion photoluminescence spectra to gather hints at a drastic emission enhancement through nanocrystal growth within the matrix. Finally, the line broadening is discussed as an important feature of RE inclusion into this host matrix which will later prove quite beneficial to the photovoltaic application of the system as a spectral upconverter of broadband illumination (see chapter 6).

SPECTROSCOPIC UNITS In the literature on optical spectroscopy there is unfortunately a mixture of conventions in place regarding the choice of physically equivalent physical units or quantities. The prominent example is the representation of spectral coordinates, where the units eV, THz, cm^{-1} , but also nm, are all in use in parallel. In the case of the first three mentioned, the actual choice does not make much of a difference, for e.g. the presentation in a graph, as their relation is merely a factor. Nonetheless, displaying spectral dependencies over the wavelength in nm is in inverse relation to those. In this work, both wavenumbers in cm^{-1} and wavelengths in nm were used for spectroscopic relations. They are related by the conversion $\lambda(\text{nm}) = 10^7/k(\text{cm}^{-1})$. The choice which of both is adequate still depends on the respective context. Moreover, SI units were used everywhere else in this work.

2.4.1 Absorption spectroscopy

NEODYMIUM ABSORPTION LINES Absorption spectra of neodymium feature characteristic peaks that arise from absorption from the ground state $4^1I_{9/2}$ to one of the numerous excited states within the 4f orbital, see Fig. 2.5. The spectra were measured with a dual-beam photospectrometer.⁶ These characteristics of neodymium vary only slightly with changing host material due to the shielding of the 4f shell. However, in Ref. [49] it is reported that the band at $12\,500\text{ cm}^{-1}$ ($|5\rangle$) is comparable to the one at $17\,200\text{ cm}^{-1}$ ($|9\rangle$) only in fluoride glasses, while $|9\rangle$ dominates in more covalent glass matrices. Figure 2.5 therefore shows features typical for an ionic glass. The absorption spectrum is comparable to spectra from the literature [49]. From Fig. 2.5 the SLJ manifolds, states with the same spin, angular momentum and total angular momentum quantum numbers, are identified. Each SLJ manifold consists of $J + 1/2$ Stark levels, whose degeneracy is lifted partially by the crystal field applied by the host matrix. The SLJ manifolds are assigned level numbers that will be used exclusively in the remainder of this work. The classification is consistent with what is usually found in the literature [80–83], including the spectral positions [84, 85].

As the RE levels are distributed along a broad spectral range, a combination of several different detector types and light sources is necessary to

⁶ Perkin Elmer Lambda 1050

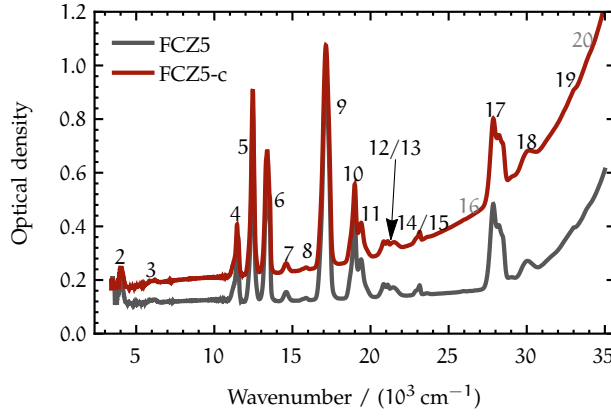


Figure 2.5: Optical density of neodymium doped (5 mol %) FCZ glass and FCZ-glass ceramic. The numbers $|N\rangle$ denote the identified SLJ manifolds, which are listed in Table 2.2. The grey numbers stand for manifolds that are to be expected but are too weak to be resolved in this graph. Note that the graphs are from the FCZ5-c sample annealed at 240 °C since Rayleigh scattering was already too strong in the case of the 260 °C sample.

be sensitive for light in the different spectral regions. To be able to calculate extinction spectra from the measurements, the two-beam spectrometer setup was deployed. Light is attenuated per length element throughout the sample (of thickness l) with an absorption coefficient α_0 such that

$$\partial_z I(z, \lambda) = -I(z, \lambda) \sum_j \alpha_{0,j}(\lambda) \quad \text{with} \quad I(0, \lambda) = I_0(\lambda) .$$

The solution to this yields the transmittance,

$$T(\lambda) := \frac{I(l_0, \lambda)}{I_0(\lambda)} = e^{-l_0 \sum_j \alpha_{0,j}(\lambda)},$$

as a function of the wavelength. Another quantity common in this context is the optical density, $OD = -\log_{10} T$, which – just like the transmittance T – includes losses not only from absorption of either of the constituents of the sample (RE ions, glass matrix, nanometric crystals) but also losses $\sim (1 - R)^2$ due to reflections at the refractive index changes at both sample surfaces of the form

$$R(\lambda) = \left(\frac{n(\lambda) - n_{\text{air}}}{n(\lambda) + n_{\text{air}}} \right)^2 .$$

The transmission and derived quantities were reflection-corrected whenever a quantitative information such as absorption cross section is deduced from them.

EFFECTIVE-REFRACTIVE INDEX MODEL For the ZBLAN-based matrix the Sellmeier-coefficients are known [86] to be

$$\begin{aligned} A &= 1.35123 \cdot 10^{-5} \mu\text{m}^4 \\ B &= 2.94780 \cdot 10^{-3} \mu\text{m}^2 \\ C &= 1.48965 \\ D &= -1.30933 \cdot 10^{-3} \mu\text{m}^{-2} \\ E &= -3.23335 \cdot 10^{-6} \mu\text{m}^{-4} \end{aligned}$$

Table 2.2: Neodymium level assignment. The abbreviated SLJ manifolds are assigned here (cf. Fig. 2.5, too) to state symbols $|N\rangle$ and used later on in this document for the sake of brevity. In the table, the spectral positions are given as approximate values.

$ N\rangle$	term symbol $^{2S+1}L_J$	λ/nm	k/cm^{-1}
$ 0\rangle$	$^4I_{9/2}$	ground state	
$ 1\rangle$	$^4I_{11/2}$	5000	2000
$ 2\rangle$	$^4I_{13/2}$	2500	4000
$ 3\rangle$	$^4I_{15/2}$	1700	5900
$ 4\rangle$	$^4F_{3/2}$	870	11 500
$ 5\rangle$	$^4F_{5/2} + ^2H_{9/2}$	800	12 500
$ 6\rangle$	$^4F_{7/2} + ^4S_{3/2}$	740	13 500
$ 7\rangle$	$^4F_{9/2}$	675	14 800
$ 8\rangle$	$^2H_{11/2}$	625	16 000
$ 9\rangle$	$^4G_{5/2} + ^2G_{7/2}$	580	17 200
$ 10\rangle$	$^2K_{13/2} + ^4G_{7/2}$	530	18 900
$ 11\rangle$	$^4G_{9/2}$	515	19 400
$ 12\rangle$	$^2K_{15/2} + ^2G_{9/2} + ^2(D,P)_{3/2}$	475	21 100
$ 13\rangle$	$^4G_{11/2}$	465	21 500
$ 14\rangle$	$^2P_{1/2}$	430	23 300
$ 15\rangle$	$^2D_{5/2}$	425	23 500
$ 16\rangle$	$^2(P,D)_{3/2}$	380	26 300
$ 17\rangle$	$^4D_{3/2} + ^4D_{5/2} + ^2I_{11/2} + ^4D_{1/2}$	350	28 600
$ 18\rangle$	$^2L_{15/2} + ^2I_{13/2} + ^4D_{7/2} + ^2L_{17/2}$	330	30 300
$ 19\rangle$	$^2H_{9/2} + ^2D_{3/2}$	300	33 300
$ 20\rangle$	$^2H_{11/2} + ^2D_{5/2}$	290	34 500

and are used to compute the refractive index dispersion with

$$n(\lambda) = \frac{A}{\lambda^4} + \frac{B}{\lambda^2} + C + D\lambda^2 + E\lambda^4. \quad (2.4.1)$$

Figure 2.6 shows a graph of $n(\lambda)$. The effective refractive index n of a composite material comprised of an FCZ glass matrix with BaCl_2 nanocrystal inclusions has been calculated on the basis of the effective dielectric function approach by J. C. M. Garnett [88, 89],

$$\varepsilon_{\text{eff}} = \frac{\varepsilon_m(\varepsilon_i(1 + 2\delta_i) - 2\varepsilon_m(\delta_i - 1))}{\varepsilon_m(2 + \delta_i) + \varepsilon_i(1 - \delta_i)}, \quad (2.4.2)$$

where ε_m and ε_i are the dielectric constants of the matrix and the inclusion, respectively (with data from Refs. [86, 87]) and δ_i the volume fraction. The refractive index follows as $n_{\text{eff}} = \sqrt{\varepsilon_{\text{eff}}}$.

SCATTERING AT NANOCRYSTALS The type of scattering in usual linear absorption measurements is elastic. Therefore no energy is lost inside the sample but is merely deviated away from the optical axis of the spectrometer and thus missing in I and hence, in T . The wavelength dependency of the scattering is determined mostly by the size of the scatterer. In the

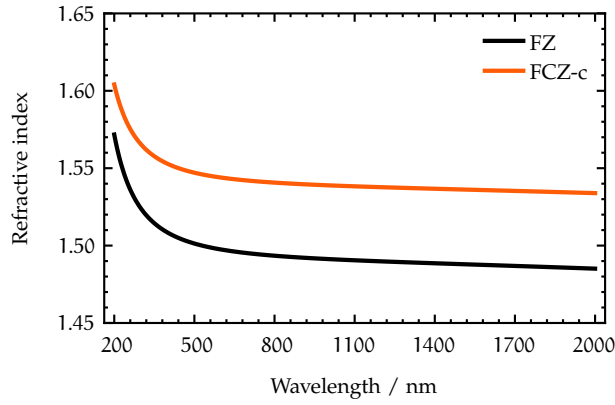


Figure 2.6: Refractive index dispersion of FZ and FCZ-c as calculated with Eq. (2.4.1) and Eq. (2.4.2), respectively, using data from Refs. [86, 87].

given samples, scattering mostly arises from the nanometric crystals grown inside the glass ceramics. Certain scattering might also arise from small bubbles and imperfections from the glass production process or scratches at the sample surfaces.

The Mie scattering theory [89] describes scattering at randomly distributed spheres with sizes near the order of the respective excitation wavelengths. Depending on the size of the object, this can be approximated by classical scattering from geometrical optics for very large objects and Rayleigh scattering for objects smaller than approximately $\lambda/5$. The latter case is present for most of the nanometric crystals in the glass ceramics, and they are also responsible for almost all of the scattering discussed in this work.

Rayleigh scattering at particles of diameter D can be attributed an extinction coefficient of the form

$$\alpha_{\text{Rayleigh}} \propto \frac{D^6}{\lambda^4} . \quad (2.4.3)$$

For the nanometric crystals in this work the scattering is therefore contributing significantly to the extinction spectra in the whole visible part of the spectrum. In Fig. 2.7 an exemplary extinction spectrum of a glass ceramic with Rayleigh scattering due to embedded nanometric crystals is shown. Towards smaller wavelengths, the absorption of the glass matrix is superposed to the scattering baseline and completely prohibits light transmission below 350 nm. Beyond 800 nm Rayleigh scattering is negligible.

ABSORPTION CROSS SECTIONS To be able to determine absorption cross section spectra for the ground state absorptions of neodymium, the effects discussed above need to be eliminated from the extinction spectra. Correction for surface reflections is carried out by multiplication of the transmittance data by $(1 - R)^2$, where the exponent of two covers the reflections at the entrance and exit surfaces of the sample.

After application of a baseline correction of the form shown in Eq. (2.4.3), the absorption cross section spectra can be determined from the absorption coefficient spectra by division by the dopant concentration N_0 ,

$$\sigma_{\text{abs}}(\lambda) = \frac{\alpha_0(\lambda)}{N_0} . \quad (2.4.4)$$

The number density N_0 in Eq. (2.4.4) is calculated from the compositional parameters [90] and is $1.76 \cdot 10^{26} \text{ m}^{-3}$ and $8.79 \cdot 10^{26} \text{ m}^{-3}$ for FCZ1 and FCZ5, respectively. The resulting integrated ground-state absorption cross sections σ_{GSA} are compiled in Table 2.3.

Table 2.3: Integrated ground state absorption cross sections σ_{GSA} for several pump levels used in this work. The spectral positions are given as approximate values.

$ N\rangle \leftarrow 0\rangle$	λ/nm	$\sigma_{\text{GSA}}/\text{pm}^2$	
		FCZ	FCZ-c
$ 4\rangle \leftarrow 0\rangle$	870	0.70	2.04
$ 5\rangle \leftarrow 0\rangle$	800	2.18	2.13
$ 6\rangle \leftarrow 0\rangle$	740	2.57	2.28
$ 7\rangle \leftarrow 0\rangle$	675	0.24	0.19
$ 8\rangle \leftarrow 0\rangle$	625	0.10	0.07
$ 9\rangle \leftarrow 0\rangle$	580	3.65	2.44
$ 10 + 11\rangle \leftarrow 0\rangle$	520	0.95	0.84
$ 12 + 13\rangle \leftarrow 0\rangle$	470	0.23	0.22
$ 14 + 15\rangle \leftarrow 0\rangle$	430	0.07	0.06

Note that the σ_{GSA} of $|4\rangle$ is remarkably larger in the FCZ-c sample than in the untreated FCZ sample, presumably due to an imperfect normalisation of the transmittance spectrometer in the region of $|4\rangle$, where the VIS detector changes to the near-infrared (NIR) detector. As this value is only used in a small fraction of the simulations of the Stokes-type transients in chapter 4, where absolute values do not matter, no further errors are imposed to the more complex simulations and the overall model. The remaining σ_{GSA} are in good agreement to values from the literature [49].

OBSERVATION OF CRYSTAL GROWTH BY RAYLEIGH SCATTERING Considering the limitations of the XRD method mentioned in section 2.3.2 another measure for the particle size appears valuable. As was discussed in the context of Eq. (2.4.3), Rayleigh-scattering at nanometric particles is connected to their size. This leads to the idea of fitting this Rayleigh-scattering extinction coefficient to the baseline of absorption spectra around the neodymium absorption features to find a second, alternative measure for the nanocrystal average sizes [75].

Fig. 2.7 clearly shows how Rayleigh scattering drastically reduces the transmittance in the visible spectral range. Measurements utilizing an integrating sphere have verified that the baseline of the transmittance spectra originates from scattering only and that no additional absorptions are introduced by the thermal treatment. It is important to note that the observed scattering provides a measure not only for the size of crystalline, but potentially any inclusion embedded into the host with a different refractive index.

With respect to the scattering analysis carried out in this work the measured transmittance spectra were corrected for surface reflections as discussed earlier in section 2.4.1. According to Shepilov [91, 92], the scattering baseline can be determined with an extinction coefficient for scattering at nanometric

crystals of diameter D , volume fraction δ_i , and refractive index n_c , embedded into a glass matrix with refractive index n_m of the form

$$\alpha_{\text{Rayleigh}}(\lambda) = 4\pi^4 \delta_i (1 - \delta_i) D^3 n_m^4(\lambda) \frac{1}{\lambda^4} \left(\frac{(n_c/n_m)^2 - 1}{(n_c/n_m)^2 + 2} \right)^2. \quad (2.4.5)$$

This equation was fit to the baselines of the absorption spectra of glass ceramics in the visible spectral range between 400 nm and 800 nm. These limits are caused by the glass absorption edge and the sensitive range of the transmittance detector. The refractive indices were defined above in the context of Eq. (2.4.1) and Eq. (2.4.2). Volume fractions were determined with the integration method as discussed in section 2.3.2. While these are only very rough estimates, possible small errors in the volume fraction are never really significant for the size determination. A detailed explanation for this as well as an error estimation is deferred to appendix A.4.1.

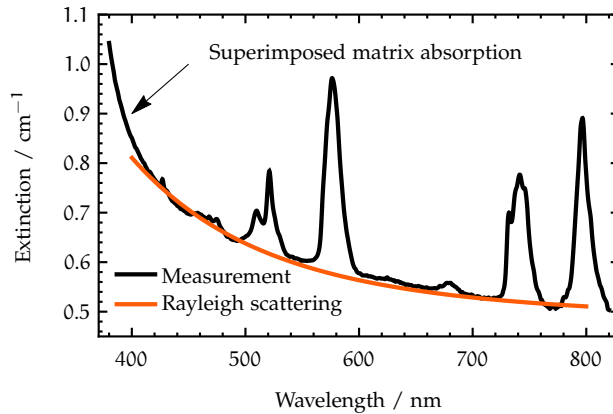


Figure 2.7: Example extinction spectrum of an FCZ1-c glass ceramic with 20 nm nanocrystals and a function according to Eq. (2.4.5) used for scattering analysis.

Fig. 2.7 shows an example of a scattering baseline fit for the sample heat treated at 260 °C yielding nanocrystal average sizes of 25 nm. The analysis fits the measurement baseline appropriately well in the whole region except from the short-wavelength edge where the glass absorption sets in.

The overall results of the Rayleigh scattering method for the size determination of the nanocrystals is shown graphically in Fig. 2.4. It shows the particle sizes obtained from both Rayleigh scattering and X-ray diffraction. The sizes obtained from either method correspond fairly well. The results of the XRD and Rayleigh-scattering based nanocrystal size investigations have also been published separately [75]. The implications of possible scattering impurities from the glass preparation, as well as the influence of the sample quality in general, are not the scope of this thesis and are discussed there.

2.4.2 Emission spectroscopy

METHOD Figure 2.8 shows the setup used for emission spectroscopy and photoluminescence transient recording. The light source is a power-stabilized femtosecond Yb:KGW laser⁷ operating at 1030 nm. Its beam is used to

⁷ Lightconversion Pharos

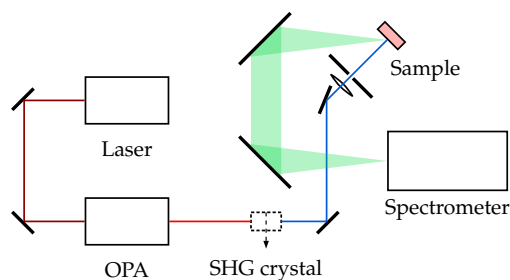


Figure 2.8: Experimental setup for room temperature photoluminescence spectroscopy. In the case of cw laser excitation, a laser diode replaces Laser, OPA, and SHG crystal.

pump an optical parametric amplifier.⁸ Together with an additional second-harmonic crystal this system produces arbitrary excitation wavelengths in the range between 300 nm to 3 μm . The characterisation of the pulse and beam parameters is shown in appendix A.2.2 and appendix A.2.1.

The pulse repetition frequency was usually set to 100 Hz or less by controlling the Pockels cell pulse picker of the femtosecond laser with a specially designed frequency division system in order to ensure the stationary state of the neodymium ions prior to each subsequent excitation pulse. A more detailed description of this system is given in appendix A.2.3. In addition, the laser intensity has usually been kept as low as possible in order to avoid any nonlinear optical effects such as $\chi^{(3)}$ self-focusing, multi-photon-absorption or saturation [93]. Another reason is that second harmonic generation at the surfaces of samples containing nanocrystals turned out to be generated relatively easily.

Attached to the monochromator⁹ in Fig. 2.8 were a cooled photomultiplier tube (PMT) for detection of visible¹⁰ or near-infrared¹¹ radiation. Gratings with 500 nm and 1.2 μm blaze angle with 600 mm^{-1} each were used, respectively. For the photoluminescence lifetime measurements the PMT output was attached to a photon counting device¹² with 32 ns time resolution after passing a preamplifier module.¹³

EMISSION ENHANCEMENT UPON NANOCRYSTAL GROWTH In Fig. 2.9, photoluminescence emission spectra from the 1 mol % doped FCZ1 glasses and several FCZ1-c glass ceramics upon pulsed excitation are shown. Fig. 2.10 shows photoluminescence and upconversion spectra from the 5 mol % doped FCZ5 glasses and FCZ5-c glass ceramics upon pulsed and continuous excitation, respectively. Fig. 2.11 shows two photoluminescence decays, one from a higher lying level (590 nm) and one from $|4\rangle$ (1050 nm). The former has contributions from the main transitions $|10\rangle \rightarrow |1\rangle$ and $|9\rangle \rightarrow |0\rangle$. The latter is mainly due to the transition $|4\rangle \rightarrow |1\rangle$, known from the main neodymium laser process.

The emission spectra of weakly doped samples under 515 nm pulsed excitation in Fig. 2.9a show only very weak emission in the visible spectral

⁸ *Lightconversion Orpheus*

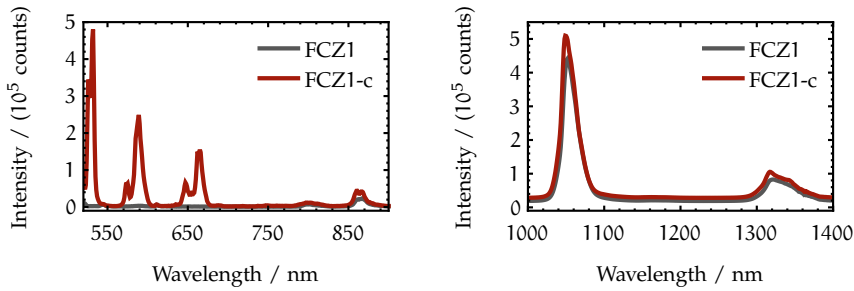
⁹ *Acton SP2500*

¹⁰ *Hamamatsu R943*

¹¹ *Hamamatsu H10330A*

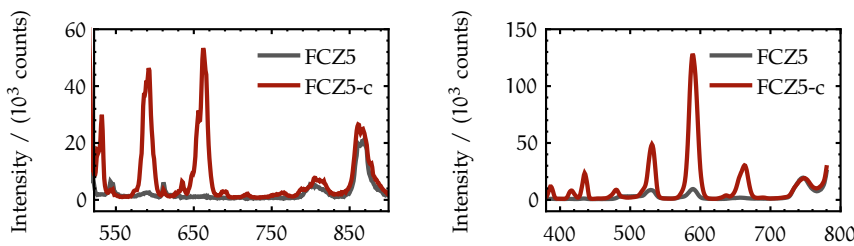
¹² *PicoQuant NanoHarp 250*

¹³ *Picoquant PAM102*



(a) VIS emission spectra upon 515 nm pulsed excitation with 20 mW. (b) NIR emission spectra upon 800 nm pulsed excitation with 5 mW.

Figure 2.9: Visible (VIS) and near-infrared (NIR) emission spectra from FCZ1 and FCZ1-c samples upon pulsed excitation. The emissions in the VIS range are affected by the nanocrystal growth and see a significant increase in emission intensity. The NIR emissions stem from the metastable level $|4\rangle$ and are not much affected.



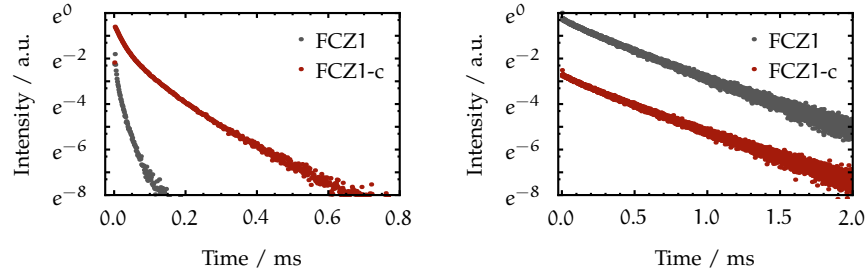
(a) Pulsed excitation at 515 nm with 20 mW. (b) Continuous excitation at 800 nm with 85 mW.

Figure 2.10: Stokes- and Anti-Stokes emission spectra from FCZ5 and FCZ5-c samples. The glass ceramics containing nanocrystals see a significant increase in emission intensity.

range from the FZ glass and the untreated FCZ precursor glass. The main part of the population is transferred via multi-phonon relaxation to the thermally coupled level subsystem comprised of $|5\rangle$ and $|4\rangle$. The corresponding ground-state transitions from there are visible in the spectrum and lie at around 800 nm and 870 nm, respectively. Their coupling will be elaborated in more detail later in section 4.1.2 and section 4.2.1.

A strong emission increase in the visible range, mainly around 500, 580 and 660 nm sets in upon thermal annealing starting with 240 °C, increasing monotonously with 250 °C to reach its maximum at 260 °C. Not shown is that the emission intensity drops again with annealing temperatures further above.

Also the photoluminescence decays from Fig. 2.11a show a huge lifetime increase induced by the nanocrystal growth. The emission at 590 nm exhibit a decay of the order of 100 μ s in the FCZ-c samples which decreases to values of the order of 10 μ s for the precursor FCZ sample. From Fig. 2.9b one can see that emissions that belong to $|4\rangle$ (or the whole thermally coupled subsystem, see Fig. 2.9a) experience no change in emission intensity upon nanocrystal growth. This is also evident from the unchanged lifetimes in Fig. 2.11b. The emission spectra of the highly doped samples under 515 nm pulsed excitation in Fig. 2.10a are similar to the weak doping scenario while the weaker emissions are slightly stronger here.



(a) Photoluminescence decays at 590 nm from FCZ1 (c) upon pulsed excitation at 515 nm with 50 mW. Growing nanocrystals leads to a significant increase in level lifetime. (b) Photoluminescence decays at 1050 nm from FCZ1 (c) upon pulsed excitation at 800 nm with 5 mW. The curves were vertically displaced for better perceptibility.

Figure 2.11: Photoluminescence decays of different transitions from weakly doped glasses (FCZ1) and glass ceramics (FCZ1-c), recorded upon pulsed excitation.

In addition, Fig. 2.10b shows the upconverted emission spectrum under continuous excitation at 800 nm (see Fig. 5.5 in section 5.2 for a process scheme). In principle, the same emission bands show up, only their relative amounts change. Additional upconverted emissions appear at 380, 420, 440 and 490 nm. The emission from $|6\rangle$ at 750 nm shows up here more strongly as it is efficiently populated from the pump level by absorption of phonons in contrast to the pulsed excitation at higher wavelengths discussed previously. $|6\rangle$ also belongs to the thermally coupled subsystem and again there is no obvious influence of the nanocrystal growth on its intensity. The emissions at shorter wavelengths see a similar drastic increase in emission intensity that was there in the Stokes photoluminescence spectra. Further examples that highlight the nanocrystal influence on lifetimes are the subject of another work [94].

POWER DEPENDENCE OF STOKES AND ANTI-STOKES TRANSITIONS The power-dependence gives hints at the population mechanism and is discussed in detail in the following section. Plotting the intensity of an emission over the excitation power on a doubly logarithmic scale and fitting a linear function to the data gives the order of the process as the slope:

Consider a process, where ETU from a lower level $|L\rangle$ is responsible for a two-step upconversion to a higher level $|H\rangle$ after GSA, originating from the ground state level $|G\rangle$, has populated the pumping level $|L\rangle$, see Fig. 2.12. The equation for the population density N of intermediate level $|L\rangle$ and receiving level $|H\rangle$ can then be written as [58]

$$\begin{cases} \partial_t N_L = \rho_{\text{GSA}} N_G - 2w_{\text{ETU}} N_L^2 - A_L N_L \\ \partial_t N_H = w_{\text{ETU}} N_L^2 - A_H N_H \end{cases} \quad (2.4.6)$$

The coefficients A_L and A_H describe the spontaneous emission and w_{ETU} the energy transfer, respectively. The pump rate is proportional to the pump power, $\rho_{\text{GSA}} \propto P$. If this is time-independent, i. e. a cw pumping source, the problem becomes stationary and the steady-state solution (where $\partial_t N_j = 0 \forall j$) implies

$$N_H = \frac{w_{\text{ETU}}}{A_H} N_L^2$$

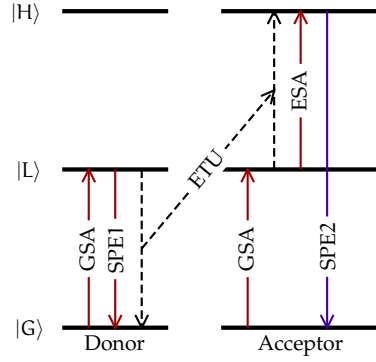


Figure 2.12: Schematic of simple upconversion process under consideration of a basic three-level system. After GSA provides the initial population in $|L\rangle$, spontaneous emission (SPE) via $|L\rangle \rightarrow |G\rangle$ can commence with a power dependence $N_L \propto P$, or ETU via $2 \cdot |L\rangle \rightarrow |0\rangle + |H\rangle$ with $N_H \propto N_L^2$ and $N_L \propto P^{1/2}$, or ESA via $|H\rangle \leftarrow |L\rangle$ with $N_H \propto PN_L$ and $N_L \propto P$. Adapted from Ref. [58].

and therefore

$$N_H \propto N_L^2 \propto \rho_{GSA}^2 \propto P^2, \quad (2.4.7)$$

whenever $w_{ETU}N_L$ is small compared to A_L and hence the linear decay associated to A_L is the dominant decay channel for level N_L [58]. Plotting such relation on a doubly logarithmic scale like

$$\log N_H \propto \log \rho_{GSA}^2 \propto \log P^2 = 2 \log P$$

gives the order of the process as the slope, which is two in this case. On a doubly logarithmic scale, the power-dependence of the directly pumped intermediate level N_L is directly proportional to the pump rate,

$$N_L \propto \rho_{GSA} \propto P, \quad (2.4.8)$$

and therefore has order 1.

For ESA, the situation is similar [58].

$$\begin{cases} \partial_t N_L = \rho_{GSA} N_G - \rho_{ESA} N_L - A_L N_L \\ \partial_t N_H = \rho_{ESA} N_L - A_H N_H \end{cases} \quad (2.4.9)$$

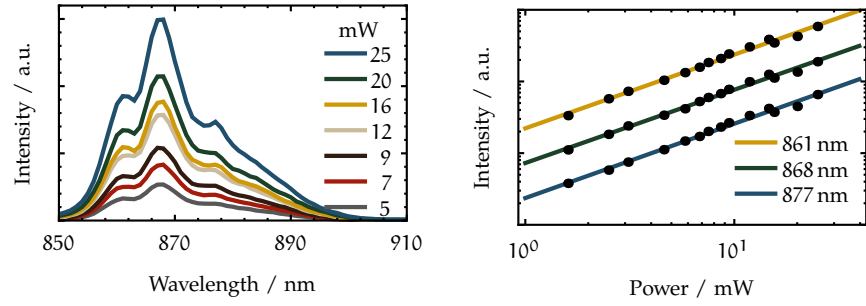
Just like the GSA rate, the ESA rate is proportional to the incident pump power, $\rho_{ESA} \propto P$. From Eq. (2.4.9) it follows under steady-state conditions

$$N_H \propto \rho_{ESA} N_L.$$

Again, for linear decay being the dominant relaxation channel of the intermediate level,

$$N_L \propto \rho_{GSA} \Rightarrow N_H \propto \rho_{ESA} N_L \propto \rho_{GSA} \rho_{ESA} N_G \propto P^2.$$

Beyond this, the situation extends for multi-order steps accordingly, where in general, an n -step process is of order n in the simplest possible model. Possible problems with the above-made assumption will be discussed later in section 2.5.3.



(a) Power dependent emission spectra of $|4\rangle \rightarrow |0\rangle$ band in FCZ1-c. The pump in resonance to $|5\rangle \leftarrow |0\rangle$ involves a phonon emission step before emission commences from $|4\rangle$. (b) Power dependence of $|4\rangle \rightarrow |0\rangle$ emission in FCZ1-c at three different wavelengths that all show the same power dependence with slope 1.0. The curves are vertically displaced.

Figure 2.13: Power dependence of $|4\rangle \leftarrow |0\rangle$ emission upon pulsed excitation at 800 nm. A slope of 1.0 indicates a linear, Stokes-type population mechanism.

Fig. 2.13a shows the power-dependent ground-state transition from $|4\rangle$ at 870 nm. The power-dependence has been recorded on three different positions related to individual Stark levels of $|4\rangle$. All three peaks show the exact same power-dependence with a slope of 1.0.

The same experiments have been carried out for multiple emission lines of Stokes-type photoluminescence at 515 nm excitation in pulsed regime and of Anti-Stokes-type upconversion luminescence pumped at 800 nm continuously, the results of all of which are summarized in Table 2.4. Note that under femtosecond irradiation at 800 nm the intentional low peak power and low repetition rate – employed to circumvent nonlinear optical effects – result in really low average power in comparison to the cw case and hence only comparably weak upconversion. Therefore, only the emissions from the metastable subsystem were measured with satisfactory accuracy and several emissions could either hardly be measured or not measured at all. Nonetheless, they are included in the table for a basic comparison, although the fluctuations in these data will not be further elaborated on in the discussion. The power-dependence of the upconverted spectra are shown in Fig. 2.14 along with the slope determination of the 530 nm emission.

The orders of the respective excitation mechanism from the slope determinations in Table 2.4 show slopes of around 1.0 in all cases where the pumping was of Stokes-type, i. e. at a pumping wavelength shorter than the emission wavelength (see upper part of the table with $\lambda_{\text{ex}} = 515 \text{ nm}$). While most emissions in the visible spectral range from FCZ1 are very weak in the pulsed pumping scheme, the other samples give better emissions and allowed slope determination from several significant peaks. Under pulsed excitation at 800 nm the situation is similar while here only the other two peaks from the thermally coupled level system, namely $|4\rangle$ and $|6\rangle$ at emission wavelengths of 870 nm and 750 nm, could be measured at satisfactory accuracy. This is due to the intentionally low average power under pulsed femtosecond irradiation at low repetition rates, both setup to avoid nonlinear optical effects that are determined by the pulse peak power. Nonetheless, both named peaks show mostly the one-order mechanism slopes with the

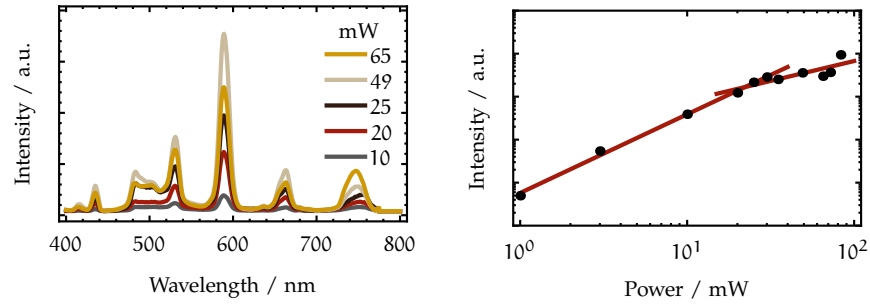
Table 2.4: Slopes of power-dependencies of emission peaks. Note that in the case of numbers marked with an asterisk (*) the slope could only be determined from the high-intensity values while the low-power data points were too noisy. Values marked with a cross-sign (†) mark slopes that change above a certain, higher power. Finally, values in brackets were derived from very noisy data and are probably less accurate.

$\lambda_{\text{em}}/\text{nm}$	FCZ1	FCZ1-c	FCZ5	FCZ5-c
	pulsed excitation at 515 nm			
545	–	0.9	1.0	1.0
575	–	1.0	1.1	1.0
590	1.0	1.0	1.0	1.0
645	1.0	1.0	1.0	1.0
660	–	1.0	1.0	1.0
750	1.0	0.9	0.9	1.0
800	1.1	1.0	1.1	1.1
870	1.0	1.0	1.2	1.1
pulsed excitation at 800 nm				
435	(1.6)	(2.4)	–	2.3
490	(2.8)	(1.4)	–	2.2
500	–	–	–	–
530	–	(2.2)	1.5	2.1
590	–	1.8	1.9	2.3
660	–	(1.6)	(2.9)	2.0
750	–	1.1	0.9	1.9*
870	1.0	1.0	1.0	1.1–1.6†
continuous excitation at 800 nm				
435	–	2.0*	2.0*	1.7
490	2.0	1.0	2.0*	1.7
500	2.1	1.0	1.9*	1.7
530	2.1	1.3	1.4	1.8–0.9†
590	1.7	1.6	1.5	1.7
660	1.5	1.4	1.8	1.6
750	1.0	1.0	1.2	1.2
870	1.0	1.0	1.1	1.0–1.4†

exception of FCZ5-c, where the slope is almost 2 at 750 nm and between 1 and 2 at 870 nm. The short-wavelength emissions are probably accompanied with larger inaccuracies, but are in general compatible to the findings in the continuous excitation scheme.

The emissions under cw excitation at 800 nm (see lower part of the table) mostly show a different behavior. All emissions to higher lying levels with emission wavelengths shorter than 700 nm exhibit power-dependencies with slopes of exactly 2 or between 1 and 2. One exception is the emission around 500 nm from FCZ1-c, where there is a slope of 1. The emission at 750 nm and 870 nm again shows a slope of around 1 as expected for an emission from the thermally coupled metastable subsystem, with the 750 nm emission being slightly nonlinear. The emission at 530 nm is 2 for FCZ1, between 1 and 2 for FCZ1-c and FCZ5 changes from nearly 2 to 1 in the FCZ5-c sample. The latter case of changing slopes is shown separately in Fig. 2.14b.

Generally, besides the mentioned exceptions the emissions at wavelengths shorter than or equal to 500 nm tend to be more clearly of slope 2 than emissions at lower wavelengths are. In contrast, most emissions from FCZ5-c tend to have less distinct, more mixed slopes between 1 and 2.



(a) Power dependent emission spectra of (b) Power dependence of upconverted upconverted emissions. 530 nm emission. The slope changes from 1.8 to around 0.9.

Figure 2.14: Power-dependence of upconverted emissions from FCZ5-c upon cw excitation at 800 nm.

2.4.3 Spectral characterization of broadened lines

Line broadening of RE has several different origins. The homogeneous contribution to the linewidth is caused by lifetime broadening. The individual transition probabilities $1/\tau_i$ between Stark levels of a J multiplet are governed by the intermultiplet phonon transition probabilities. These are statistical events distributed around an average lifetime $\bar{\tau}$. As each level is rapidly changing over time, a quantum mechanical uncertainty $\Delta E \approx \hbar/\tau$ is conveyed over to its energy E, leading to a spectral distribution.

Inhomogeneous line broadening on the other hand, is due to site to site variations of the crystal field in glasses or due to inhomogeneous stress or strain in crystals. Such line broadening can be large whenever charge compensation is required [95]. In glasses, inhomogeneous line broadening is the dominant mechanism at room temperature [49, 96]. It might be large enough to mask the electric field splitting of individual Stark levels or even render them invisible [49, 97, 98]. The shape of the lines is then Gaussian or a combination of Gaussian and Lorentzian (Voigt profile), in contrast to perfect crystals, where sharp lines split into clearly separate Stark levels of ideal Lorentzian shape [99].

The energy separation ΔE of the electronic levels is a crucial parameter and having a reliable measure of it is most important for modelling correctly the radiative transitions with the Judd-Ofelt and McCumber theories, described later in section 3.1 and section 3.3.3. In the Judd-Ofelt theory it enters not only via the wavelengths of transitions (a minor error source), but it also is a potential source of larger errors in the Boltzmann-weighted grouping of individual levels to level groups with common radiative decay rates. In the McCumber theory, a similar thermodynamic factor is governed by small energy separations where errors usually have a significant impact. Finally the phonon contribution to electronic decays is dominated by the energy

gap via the energy gap law (see section 4.1.2) and has therefore a crucial influence on almost any transition modelled in the rate equation model.

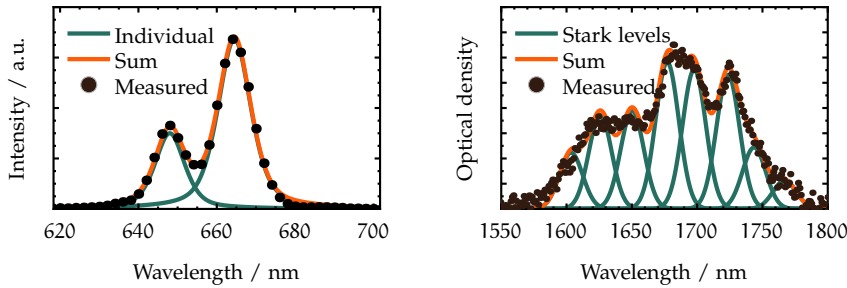
ENERGY POSITION OF BROADENED LINES Taking the peak energy position to characterize the energy level positions and determine the energy gaps between levels is often a useful approximation. In the material subject to this work however, inhomogeneous line broadening and electric field splitting make it sometimes necessary to consider that this would largely overestimate certain energy gaps. Also, in the case of very asymmetric peaks, the energy positions were not reflected correctly. In cases where this is problematic – for example the assumption of mono-exponential energy gap laws would easily fail due to this – it can help to use the energy positions determined as barycentric (centre of mass) energy positions [90, 99], like

$$\lambda_{\text{cm}} = \frac{\int \lambda \sigma(\lambda) d\lambda}{\int \sigma(\lambda) d\lambda}. \quad (2.4.10)$$

ESTIMATION OF LINE WIDTHS As not all peaks have high signal to noise ratio, approximation functions with Gaussian profiles

$$V_G(k) = \exp\left(-\ln 2 \left(\frac{k - k_0}{w}\right)^2\right),$$

were fitted to particular lines to enable for realistic determination of the line widths. In the formula, $2w$ is the full-width at half-maximum of the profiles. Quite similar, overlapping peak groups were assembled from linear combinations of these line-shape functions. The working principle becomes obvious from Fig. 2.15a.



(a) Example for decomposition of overlapping emission line profiles by linear combination of Pseudo-Voigt functions. The emissions are from FCZ1-c under pulsed excitation at 515 nm. (b) Example for Stark level decomposition for the case of the absorption line $|3\rangle \leftarrow |0\rangle$ (${}^4I_{15/2}$) in FCZ5-c. The figure shows the line approximation by $J + 1/2 = 8$ individual Stark levels.

Figure 2.15: Decomposition of overlapping emission lines or of overlapping Stark level absorptions in glass ceramics.

The line widths are summarized in Table 2.5. There is a general correlation between the line width and the number of Stark levels, $J + 1/2$. However, this is not strictly true. There are two main reasons. Firstly, a common J for level groups is not well-defined and it depends on the most intense level to dominate the Stark split. Secondly, several lines are very weak anyway and the experimental errors are then considerably larger than for an intense, single- J level. From the last column in Table 2.5 it can be seen that most

Table 2.5: Linewidths (FWHM) for FCZ and FCZ-c as determined from absorption spectroscopy. The third column gives the relative change of the line width of FCZ-c with respect to FCZ in %.

$ N\rangle \leftarrow 0\rangle$	$\Delta k/\text{cm}^{-1}$		$\Delta_{\text{rel}}/\%$
	FCZ	FCZ-c	
$ 1\rangle \leftarrow 0\rangle$	–	–	–
$ 2\rangle \leftarrow 0\rangle$	430	460	7
$ 3\rangle \leftarrow 0\rangle$	313	326	4
$ 4\rangle \leftarrow 0\rangle$	219	138	–37
$ 5\rangle \leftarrow 0\rangle$	251	277	10
$ 6\rangle \leftarrow 0\rangle$	208	245	18
$ 7\rangle \leftarrow 0\rangle$	189	274	45
$ 8\rangle \leftarrow 0\rangle$	266	299	12
$ 9\rangle \leftarrow 0\rangle$	325	456	40
$ 10\rangle \leftarrow 0\rangle$	206	347	69
$ 11\rangle \leftarrow 0\rangle$	342	314	–8
$ 12\rangle \leftarrow 0\rangle$	265	307	16
$ 13\rangle \leftarrow 0\rangle$	328	352	7
$ 14\rangle \leftarrow 0\rangle$	228	288	26
$ 15\rangle \leftarrow 0\rangle$	187	182	–3

levels undergo a considerable broadening upon the nanocrystal growth. For other cases, like the SLJ manifold $|4\rangle$ or $|11\rangle$, a decrease of the line width was observed. The uncertainty of the line width analysis is probably not much better than 10%, especially in the case of weak levels. Therefore, relative deviations of less than 10% are presumably meaningless.

2.5 DISCUSSION

2.5.1 Origin of emission increase

The observations from the previous paragraph can be summarized in the following way: Nearly all emissions see a huge increase in intensity upon nanocrystal growth. The notable exceptions are the levels $|4\rangle$ to $|6\rangle$. $|4\rangle$ (and hence the two levels thermally coupled to it, cf. section 4.2.1) is metastable due to its exceptionally large energy gap to level $|3\rangle$, which can be seen clearly in the near-infrared part of the absorption spectrum in Fig. 2.5. This leads to the conclusion that the nanocrystals change the phonon spectrum of (a part of) the neodymium such that much smaller multi-phonon relaxation rates W_{PE} are generated. From the symbolic relation that describes the lifetime time of any level as a sum of the contributions of the individual decay channels,

$$\tau^{-1} = A_{\text{SPE}} + W_{\text{PE}} + \dots, \quad (2.5.1)$$

it hence follows that the decay becomes more beneficial for radiative decay (SPE) and with shrinking W_{PE} the lifetimes τ increase. As a consequence, the intensity of an emission increases with

$$I_{\text{PL}} \propto \int_0^{\infty} I_{\text{decay}}(t) dt = \int_0^{\infty} I_0 \exp(-t/\tau) dt = I_0 \tau. \quad (2.5.2)$$

This is the working principle of emission increase upon nanocrystal growth. It also makes it understandable that there should be only a very small effect if any, when the W_{PE} are already quite low, for example in the case of the emissions of $|4\rangle$. The large energy gap there implicates negligible W_{PE} due to the energy gap law (cf. section 4.1.2 for details)

$$W_{PE} \propto \exp(-c\Delta E), \quad c = \text{const.}$$

and consequently, the lifetime becomes $\tau^{-1} \approx A_{SPE}$. The non-existent nanocrystal effect on the levels in the vicinity of $|4\rangle$ is obvious since whenever there is no dependency on phonons, there is also no phonon-dependent change to be expected.

2.5.2 Spectral identification of transitions

With the information from the absorption spectra in Fig. 2.5 and the energy positions of the SLJ manifolds (summarized in Table 2.2), it becomes possible to identify the main contributions to the Stokes emission lines from the weakly doped samples in Fig. 2.9a. As the excitation is at 515 nm, in resonance to $|11\rangle$, the double peak around 530 nm must be caused by emission from $|10\rangle \rightarrow |0\rangle$. The emission groups around 575/590 nm and 650/660 nm are both mainly $|10\rangle \rightarrow |1\rangle$, $|9\rangle \rightarrow |0\rangle$ and $|10\rangle \rightarrow |2\rangle$, $|9\rangle \rightarrow |1\rangle$, respectively. Light at 800 nm and 870 nm stems from groundstate decays of levels $|5\rangle$ and $|4\rangle$, respectively. Nearly the same emissions are generated in the highly doped samples as shown in Fig. 2.10a while some emissions are more easily identified. In any case, there are potentially also minor contributions from weaker levels. Their contributions will be discussed later after the rate equation model has been introduced in chapter 4, which allows selective investigation of any spectral contributions. The main contributions however, which are relevant to the emission spectra, are schematically shown in Fig. 2.16.

The near-infrared emissions from the weakly doped samples in Fig. 2.9b are well resolved and come from the metastable level $|4\rangle$, decaying to either $|1\rangle$ with 1050 nm or $|2\rangle$ with 1330 nm. The decay $|4\rangle \rightarrow |1\rangle$ is the famous neodymium laser transition that is exploited in almost all neodymium based solid-state lasers. From the figure it is again obvious that the transitions starting from $|4\rangle$ do not undergo an intensity change upon nanocrystal growth.

The upconversion spectra in Fig. 2.10b again show similar transitions. The 380 nm light comes from $|16\rangle$ which is populated by excited-state absorption and phonon absorption from $|15\rangle$. Note that this is a continuously pumped system and it can be expected to be different from the spectra obtained upon pulsed excitation.

2.5.3 Order of Anti-Stokes population mechanisms

MAIN FINDINGS Apart from some notable exceptions the general observations from the power-dependency analysis in section 2.4.2 are the following: Stokes-type excitation at wavelengths shorter than the emission wavelengths usually leads to slopes of around 1, and are therefore of order 1 according to Eq. (2.4.8). Moreover, emissions from higher lying levels and at wavelengths

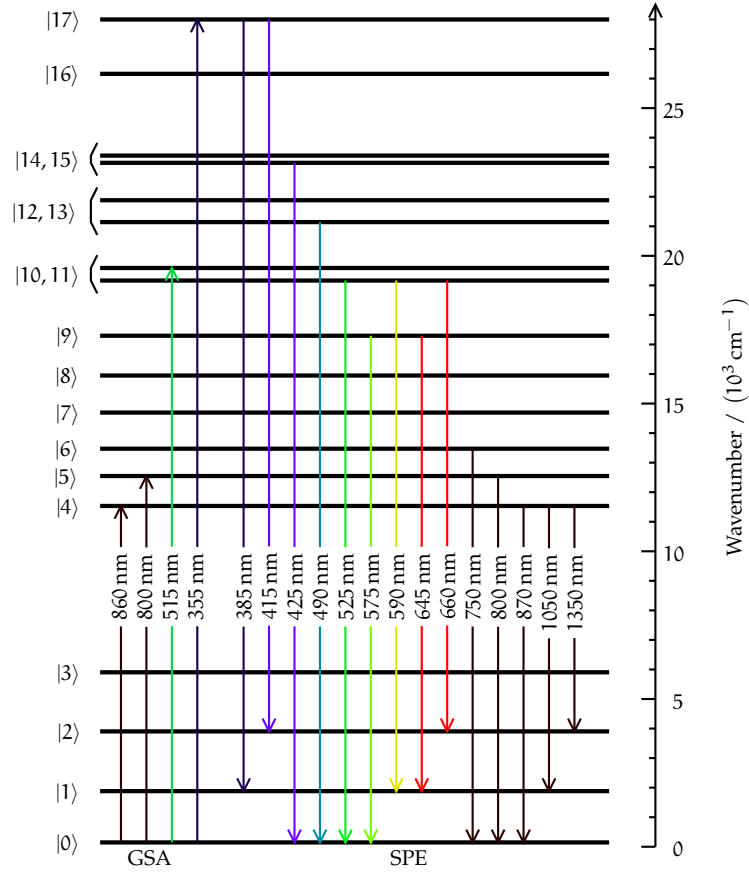


Figure 2.16: Neodymium energy level scheme with relevant electronic transitions of the Stokes-type. See Table 2.2 for level assignments.

shorter than the excitation wavelength, are upconverted emissions, and usually show a slope of 2. If ETU is the dominating upconversion mechanism, this implies a two-step energy-transfer. The same holds for slopes in between 1 and 2, and there are reasons why the slope might not be exactly 2 in these cases, which are briefly discussed in the following.

If the assumption of $w_{\text{ETU}}N_L < A_L$ does not hold for Eq. (2.4.7), as it had been implicated in section 2.4.2, and the ETU is dominating the depletion of the level N_L , the relation between the upconverted emission intensity and the pump light intensity is not a potential law anymore [58]. Then, with neglecting $A_L N_L$ in the steady-state solution of Eq. (2.4.6), it follows that

$$N_L^2 \propto \rho_{\text{GSA}}$$

which finally implicates

$$N_H \propto \rho_{\text{GSA}} \propto P, \quad (2.5.3)$$

corresponding to a slope of 1 on a doubly logarithmic scale. Note that this also implicates

$$N_L \propto \sqrt{P} \quad (2.5.4)$$

for the intermediate level's power-dependence (slope smaller than 1).

The same is established for ESA when it dominates the linear decay channel of the intermediate level in Eq. (2.4.9) and $\rho_{\text{ESA}} > A_L$ leading to

$$N_L \neq N_L(P) \Rightarrow N_H \propto P. \quad (2.5.5)$$

From this it follows that at intermediate excitation rates, where neither linear decay nor ETU/ESA can be neglected, the two compete and the slopes determined from power-dependencies in such situation would be somewhere in between 2 and 1 or even less than 1 for ETU and ESA, respectively. It is evident from this simple analysis that whenever ETU and ESA are non-negligible at the same time, the situation is even more complex.

For the present case of neodymium, the simple energy level scheme in Fig. 2.12 is already sufficient to discuss the order of occurring processes. The intermediate level is neodymium's metastable level $|4\rangle$ (thermally coupled levels $|5\rangle$ and $|6\rangle$ included) whereas the upconverted emissions originate from levels $|7\rangle$ upwards. It will later be shown in section 5.1.1 that there is one non-vanishing overlap for ESA at the pumping wavelength of 800 nm, a resonant pump for the metastable subsystem ($|4\rangle$ to $|6\rangle$). This overlap is for the ESA transition $|4\rangle \rightarrow |15\rangle$. However, this overlap is still very small and hence is the ESA cross section. This is also confirmed from power-dependent transmission measurements, where a constant slope was found, which, according to

$$T(P) = I_0 e^{-(\sigma_{\text{GSA}} N_0 + \sigma_{\text{ESA}} N_4) l_0},$$

indicates small ESA with respect to GSA because $T(P)$ should drop at sufficiently large pump powers via $N_4 \propto P$. This is not the case (see Fig. 5.10b for the measurement).

Judging from the data in Table 2.4 and the analytic relationships just established, it can be concluded for the present system that (i) ETU appears to be the dominant upconversion mechanism due to the small spectral overlap for ESA at the pump wavelength; (ii) ETU is mainly of second-order, as all power-dependency slopes are either 2 or between 1 and 2.

SECONDARY FINDINGS A secondary observation is a slope of 2 for the 750 nm emission and of about 1.5 for the 870 nm emission, both at higher powers, and both from the FCZ5-c sample under pulsed excitation at 800 nm, where a slope of 1 would be expected for a presumably Stokes process and is also actually achieved with the other samples. From this slope it follows that the 750 nm emission is not solely from $|6\rangle \rightarrow |0\rangle$, but must originate from an upconverted transition, for example $|9\rangle \rightarrow |2\rangle$ which appears at nearly the exact same wavelength. The same is true for 870 nm where $|9\rangle \rightarrow |3\rangle$ is a possible upconverted transition near this frequency. Whenever the upconversion is strong enough such that the intensity from the transition from the higher level becomes comparable to that from the linear decay from the thermally coupled subsystem of levels $|4\rangle$ to $|6\rangle$, the slope changes to 2. However this situation is only set when (a) neodymium is under nanocrystal influence as the glasses do not emit efficiently in the visible spectral range and (b) the neodymium concentration is large enough for significant ETU which is both the case for the FCZ5-c sample and hence only fulfilled there. Note that there is a certain amount of ETU also in the FCZ1 samples but it is very weak and thus measurements of it are strongly affected by experimental uncertainties. Note also that the FCZ5 (-c) samples show a certain

contribution of higher levels to the 750 nm emission even under continuous excitation (slope of 1.2).

In Ref. [58], a case similar to the upconverted 530 nm emission upon cw excitation shown in Fig. 2.14b, is discussed. The main argument for the observed decrease in the power dependence slopes is that all neodymium ions participate in the ETU processes, in contrast to the case of partially isolated neodymium ions due to ion clustering at other sites. If this were the case, the assumption of homogeneously distributed neodymium ions throughout the glass and glass ceramic samples would be falsified. Therefore, the power dependence of the ground-state emission of the intermediate level would have to drop starting from 1 and reapproach 1 after a certain power threshold. At the same time the upconverted emission would have to show the above mentioned decrease. However, the former is neither observed in Ref. [58] for neodymium in LiYF_4 nor is it in the data in Table 2.4. Accordingly it can be concluded that all neodymium participates in ETU and that there is no significant clustering leading to partial isolation of any remaining, non-clustered ions.

One further peculiarity observed in Table 2.4 is the slope of 1 for the emissions near 500 nm upon 800 nm cw illumination of FCZ1-c. According to Eq. (2.5.3) and Eq. (2.5.4) this would have to be accompanied by a slope of less than 1 for the Stokes emission under this pump scenario, if ETU were dominant here. This is not found. However, a slope of 1 would also be found when the dominant upconversion mechanism were a strong ESA process that was governing the depletion of the intermediate state (see Eq. (2.5.5)). This seems plausible here due to the low neodymium concentration in FCZ1-c and at the same time high excitation powers. Another reason may be the smaller ESA overlap in FCZ1 compared to FCZ1-c (shown in detail later in section 5.1.1). It can even be speculated that there may be an efficient ESA process, such as $|11\rangle \rightarrow |19\rangle$ or similar, depleting $|11\rangle$. The fact that the remaining upconverted emissions have a slope of 2 at high powers shows that ETU is dominant there.

Finally note that the power-dependent upconversion spectra analysed in section 2.4.2 and discussed in this section, will later serve as the basis for the experimental verification of the steady-state rate equation system in section 5.3.2. They will therefore be further integrated over five whole wavelength regions to come by the experimental uncertainties with a larger integration interval while maintaining a certain spectral resolution. Any spectral overlaps of ground-state emissions with non-ground-state emissions from higher lying levels will also be considered in the comparison there and taken into account in the rate equation simulation.

2.5.4 Linewidths and spectral overlaps

As a general result, the line widths of neodymium in the glassy host are rather large. In the glass ceramics a mixture of glassy and crystal-field split, crystalline bands is found. The FWHM line widths have a mean value of 270 cm^{-1} in FCZ and 300 cm^{-1} in FCZ-c. For comparison, line widths of neodymium in the crystals LaCl_2 and YAG are typically 10 cm^{-1} and 4 cm^{-1} , respectively. [95, 100]. The line widths found here for glasses are of the order of values for fluorozirconate glasses elsewhere [84]. The differences between crystalline and glassy line widths are due to the amorphous

character of the latter. Although short-range interactions of RE ions are similar in both hosts, the glasses lack a long-range order [101] with the result that the local environment of any ion is different at different positions within the glass matrix. These site-to-site variations cause the line-broadening and also lead to deviations from mono-exponential decay and other variations in radiative parameters due to their distribution around a mean value.

The broad line widths have several consequences for the later analysis in this work: The situation of an already considerable number of overlapping transitions in free-ion neodymium gets tightened even more as even slightly off-resonant transitions have a significant spectral overlap in this host. This means that not only spectral overlap integrals that enter the formulae for ESA cross sections or ETU/CR coefficients increase, but also that nonvanishing overlap is generated for processes that were not resonant at all in crystals (cf. to section 5.1.1 and section 5.1.2 for details concerning the overlap study of upconversion processes). Related to this overlap increase is also the increase of possible transitions per wavelength interval for a steady-state neodymium ion with all-occupied levels. Contrary to a perfect crystal with clearly separate transitions in frequency-space, the distribution of transitions per wavelength interval is almost continuous and larger than one for most wavelengths (see Fig. 6.3 in chapter 6). As a result, a broadband excitation of such a pre-occupied, steady-state neodymium ions will result in a broadband absorption leading to broadband upconversion of the light which will be modelled and analysed in chapter 6.

Nonetheless, the broad line widths also cause problems for the spectral analysis. For example, in a strongly overlapping level scheme, a selective excitation can be hard to achieve. The magnitudes of absorption cross sections and line-shapes have to be inspected to achieve still this, but care has to be taken in interpreting the results of all excitation schemes. This emphasizes the experimental imperative of low-intensity excitation even further. Also, the distribution of states over a broad range soften the precise definition of energy gaps. Up to a certain degree, the approximation of energy gaps by the difference between the peak positions of broadened lines remains valid enough not to falsify energy gap laws. As these are exponentially depending on the energy separations however, wider line broadening might cause more significant deviation from a mono-exponential energy gap law.

2.6 SUMMARY

Spectral upconversion was introduced as an avenue to potentially increase the efficiency of Silicon solar cells with the help of an upconverting bottom-layer. For good conversion efficiency, losses to nonradiative processes – mainly phonons of the host – need to be minimized. This also forms one major technological approach towards efficiency optimization, namely the careful choice of the host. The canonical materials have either good relaxation properties but are hard to handle (such as crystals) or are less well performing while equipped with appreciable mechanical and optical properties at the same time. An approach of combining optimum phonon spectra of BaCl_2 crystals with an intermediately performing photonic glass (ZBLAN) leads to the FCZ glass-ceramics with BaCl_2 nanocrystals. This material benefits from both.

The choice of the dopant naturally leads to erbium, which from a first glance has upconversion transitions at wavelengths well suited to the photovoltaic application and also good cross sections for the necessary processes. However, erbium does not enter the nanocrystals. Neodymium does enter and can thus profit from the beneficial relaxation properties conveyed by BaCl_2 . While neodymium initially does appear inferior to erbium with regard to the spectral suitability of the elementary upconversion step for photovoltaic application (800 nm as compared to $1.54 \mu\text{m}$ for erbium), this assessment might prove premature because of the huge differences between monochromatic, laser-induced upconversion and broadband, solar-excited upconversion.

In the preceding chapter, the preparation of the glass-ceramics was briefly summarized. The growth of the nanocrystals was verified from two independent approaches, namely X-ray diffraction and Rayleigh-scattering. Both methods were also used complementary to gather information on the size of the nanocrystals in two totally different experimental ways. Furthermore, an effective refractive index description was established for the composite glass ceramic where the nanocrystals are treated as inclusions into an homogeneous host on the basis of a Garnett-model. Based on this prearrangement, absorption cross sections were measured for later use in the rate equation model. Emission spectroscopy under a variety of different excitation regimes was used to compile evidence for the drastic photoluminescence and upconversion enhancement spawned by the nanocrystals. Besides the identification of the emissions and the spectral characterization of the line shapes, the power-dependencies of upconversion emissions were used to establish the principal upconversion population routes. This forms the basis for the development of the upconversion rate equation model later in chapter 4.

3

EINSTEIN COEFFICIENTS FOR SPONTANEOUS EMISSION

The radiative decay, described by the Einstein coefficients for spontaneous emission (SPE), is an important part of the electronic relaxation dynamics. The complete corresponding time evolution will be discussed as part of a rate equation system in chapter 4. As the coefficient matrix of this model depends strongly on the Einstein coefficients, they need to be known with sufficient precision. In section 3.3.2 and section 3.3.3 it is described, how decay constants were determined experimentally. However, the experimental decay rates are often not equal to the radiative rates due to the presence of strong nonradiative loss mechanisms. As they are thus not experimentally accessible, another, semi-theoretical approach was employed, the so-called Judd–Ofelt (JO) theory.

This theory processes spectroscopic data under linear excitation conditions and defines a set of numbers that contain the host dependent part of the rare-earth properties. In addition, they give qualitative information on the inclusion of neodymium into the BaCl_2 nanocrystals. Moreover, together with the host-independent part of the rare earth description, which is tabulated in the literature, the theory enables for the calculation of the Einstein coefficients of SPE.

3.1 JUDD–OFELT THEORY FOR EFFECTIVE REFRACTIVE INDEX MEDIUM

3.1.1 Overview of Judd–Ofelt theory in glass and glass ceramics

A schematic overview of the analysis algorithm is given in Fig. 3.1. Starting with linear spectroscopic data from the samples at the top, namely transmittance spectra $T(\nu)$, the absorption cross section spectra are calculated using the dopant concentration N_0 . This was already explained in section 2.4.1. Spectral integrals of the cross section spectra of SLJ absorption bands enter the so-called measured oscillator strengths, f_{meas} .

Independently, the theoretical oscillator strengths of the neodymium transitions are calculated. These discriminate between contributions of electric and magnetic dipoles, f_{ed} and f_{md} . There are also contributions from electric quadrupoles, but they are very small [102]. The two dipole contributions are calculated from reduced matrix elements, which are tabulated in the literature [85, 103–105]. Special care has to be taken with regard to the refractive indices which enter the evaluation of the actual local field within the neodymium host. For the glass the ZBLAN index has been used (see Eq. (2.4.1)). For the glass ceramic however, refractive index fluctuations exist in the composite material of glass matrix and BaCl_2 nanocrystals. The

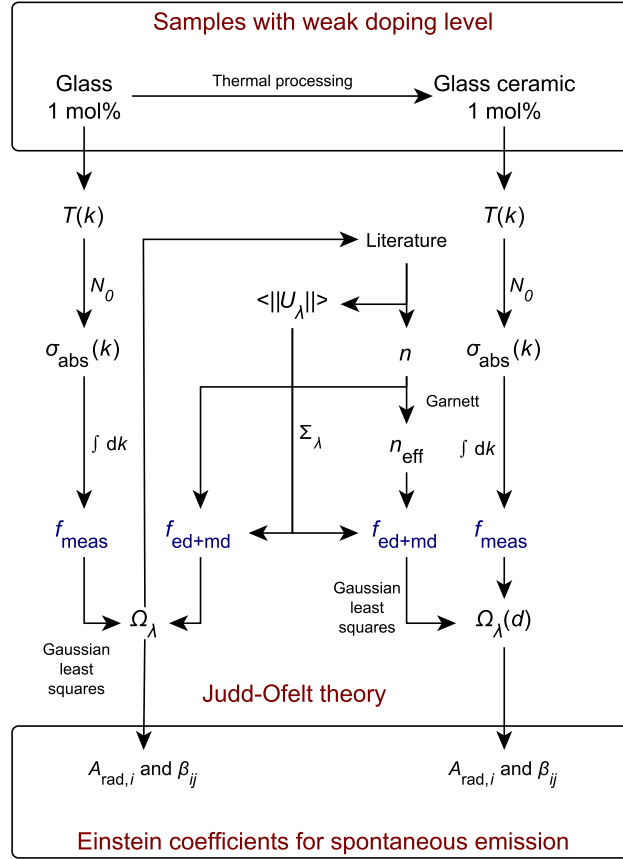


Figure 3.1: Schematic of Judd-Ofelt analysis

Garnett-based effective refractive index was employed in these cases (see Eq. (2.4.2)).

Given the experimental and theoretical oscillator strengths, the JO intensity parameters Ω_λ ($\lambda = 2, 4, 6$) are calculated with a matrix approach (Gaussian least-squares method). They are derived in separately for the glass and the glass ceramic. From these, the radiative properties, namely the Einstein coefficients and branching ratios of all neodymium transitions are calculated.

3.1.2 Determination of intensity parameters

The JO theory [102, 106, 107] allows for the calculation of electronic transition probabilities within the rare earth's 4f orbitals. The canonical determination of the so-called intensity parameters, Ω_λ , is carried out with a least-squares fit of the experimental to theoretically calculated oscillator strengths. These Ω_λ parameters are correlated to structural properties of the matrix and the local environment surrounding the rare earth ion. They can be used to calculate radiative decay rates of any given level as well as the respective branching ratios.

Starting from the absorption cross section spectra as determined in section 2.4.1, the experimental oscillator strengths, f_{meas} for each absorption

process from the ground state to any excited state within the energy range (k_1, k_2) is determined according to

$$f_{\text{meas}} = \frac{4\pi\epsilon_0}{e^2} \frac{m_e c_0^2}{\pi} \int_{k_1}^{k_2} \sigma(k) dk, \quad (3.1.1)$$

where m_e is the mass of the electron, c_0 the speed of light and $\sigma(k)$ the absorption cross section from Eq. (2.4.4). However, as the individual levels listed in Table 2.2 are overlapping in more than a few cases, only the sums of those oscillator strengths were derived. This is reflected in the summary of measured oscillator strengths in Table 3.2.

The theoretical oscillator strengths comprise contributions from electric, f_{ed} , and magnetic dipole transitions, f_{md} , which are of the form

$$f_{\text{ed}} = \frac{4\pi\epsilon_0}{e^2} \frac{8\pi^2 m_e \nu}{3h(2J+1)} \chi_{\text{ed}} S_{\text{ed}}$$

and

$$f_{\text{md}} = \frac{4\pi\epsilon_0}{e^2} \frac{8\pi^2 m_e \nu}{3h(2J+1)} \chi_{\text{md}} S_{\text{md}}$$

with ν the mean frequency of the respective transition and J the corresponding total angular momentum quantum number. The quantities

$$S_{\text{ed}} = \sum_{\lambda} \Omega_{\lambda} |\langle i || U_{\lambda} || j \rangle|^2 \quad (3.1.2)$$

and

$$S_{\text{md}} = \left(\frac{eh}{4\pi m_e c} \right)^2 |\langle i || L + 2S || j \rangle|^2$$

are the electric and magnetic dipole line strengths, respectively, in which $\langle i || U_{\lambda} || j \rangle$ are the doubly reduced matrix elements of the electric dipole tensor operator and $\langle i || L + 2S || j \rangle$ the matrix elements of the magnetic dipole operator for the transitions between the 4f states i and j . These are in general independent of the host matrix and are given in the literature for neodymium [85, 103–105] and other RE ions [90, 102]. The factors

$$\chi_{\text{ed}} = (n^2 + 2)^2 \quad \text{and} \quad \chi_{\text{md}} = n \quad (3.1.3)$$

further denote the local field correction factors under the tight binding model [108].

With the oscillator strengths established, the Gaussian least-squares method is used to minimize

$$f_{\text{meas}} - f_{\text{md}} = f_{\text{ed}}^{(\lambda)} \Omega_{\lambda}$$

in order to evaluate the intensity parameters Ω_{λ} (with $\lambda = 2, 4, 6$). Minimizing $f_{\text{meas}} - f_{\text{md}}$ is equivalent to solving $\mathfrak{F} \Omega = f_{\text{meas}} - f_{\text{md}}$ for the vector Ω [90]. There, \mathfrak{F} is a $(j \times \lambda)$ -matrix containing the calculated oscillator strengths $f_j^{(\lambda)}$ as

$$\mathfrak{F} = \begin{pmatrix} f_{\text{calc},1}^{(2)} & f_{\text{calc},1}^{(4)} & f_{\text{calc},1}^{(6)} \\ f_{\text{calc},2}^{(2)} & f_{\text{calc},2}^{(4)} & f_{\text{calc},2}^{(6)} \\ \vdots & \vdots & \vdots \end{pmatrix}$$

and

$$f_{\text{meas}} - f_{\text{md}} = \begin{pmatrix} f_{\text{meas},1} \\ f_{\text{meas},2} \\ \vdots \end{pmatrix},$$

the vector of the oscillator strengths, this is achieved by calculating

$$\Omega = \left(\mathfrak{F}^T \mathfrak{F} \right)^{-1} \mathfrak{F}^T (f_{\text{meas}} - f_{\text{md}}).$$

The effective refractive index n of the FCZ-c glass ceramics were calculated with Eq. (2.4.2), as discussed earlier in section 2.4.1.

3.1.3 Calculation of radiative properties

Given the JO intensity parameters Ω_λ , the radiative transition probabilities between the states $|j\rangle$ and $|i\rangle$ can be calculated [90]

$$A_{ji} = \frac{64\pi^4\nu^3}{3hc^3(2J_j + 1)} (\chi_{\text{ed}}S_{\text{ed}} + \chi_{\text{md}}S_{\text{md}}). \quad (3.1.4)$$

As $|i\rangle$ is not necessarily the ground state ($i = 0$), the branching ratios

$$\beta_{ji} = \tau_j A_{ji} \quad (3.1.5)$$

are an important quantity to describe the dynamics as they define the rate share for each possible radiative relaxation channel.

Groups of at least partially overlapping levels are thermally coupled when their energy difference is of the order of $k_B T$. Several of such groups are present here due to the significant line broadening in the glasses and glass ceramics. Their total radiative lifetime is not simply $\tau = 1/\sum_j A_j$. As the levels are thermally coupled, a thermal equilibrium will arise within picoseconds or less. Subsequently, the relative occupation numbers n_j are Boltzmann-distributed and can hence be calculated with

$$\tau = \frac{1}{\sum_j n_j A_j}, \quad (3.1.6)$$

where

$$n_j = \frac{(2J_j + 1)e^{-E_j}}{\sum_i (2J_i + 1)e^{-E_i}}. \quad (3.1.7)$$

In Eq. (3.1.7) the E_i are the energy positions of the sublevels i in units of $k_B T$. The index i iterates over all sublevels including j [90].

It is noteworthy here that this weighting procedure induces a temperature dependence on the radiative emission probabilities for the level groups. While the JO parameters Ω_λ also show a temperature dependence, the Einstein coefficients of individual isolated levels do not [109].

3.2 RESULTS

3.2.1 Oscillator strengths

The measured oscillator strengths were determined with Eq. (3.1.1) from absorption cross section spectra for each of the weakly doped samples, both glasses and glass ceramics. Strongly overlapping levels or level groups were concatenated in this step. From these experimentally derived oscillator strengths, the theoretically expected contribution from magnetic dipole interactions given in Table 3.1 [104] are subtracted to gain the experimental oscillator strengths

$$f_{\text{meas}} - f_{\text{md}} =: f_{\text{meas,ed}}$$

due to electric dipole interaction [110]. Higher-order electric or magnetic contributions are even smaller than the magnetic dipole values and hence negligible. This quantity will later be used to determine the JO intensity

Table 3.1: Magnetic dipole oscillator strengths considered. From Ref. [104].

SLJ manifold	$ N\rangle$	$f_{\text{md}}/10^{-6}$
${}^2\text{H}_{9/2}$	$ 5\rangle$	0.0112
${}^4\text{F}_{9/2}$	$ 7\rangle$	0.0020
${}^2\text{G}_{7/2}$	$ 9\rangle$	0.0002

parameters as a measure for the influence of the host on the free-ion RE. The measured oscillator strengths are presented in Table 3.2 and their behavior over the sample types encompassing the influence of nanocrystal growth is shown graphically in Fig. 3.2.

Table 3.2: Measured oscillator strengths $f_{\text{meas}} - f_{\text{md}}$ for the glasses (FZ1 and FCZ1) and glass ceramics samples (FCZ1-c, denoted by their thermal treatment temperatures) with different nanocrystal sizes in comparison.

SLJ manifold	$(f_{\text{meas}} - f_{\text{md}})/10^{-6}$					
	FZ	FCZ	240 °C	250 °C	260 °C	270 °C
$ 15 + 14\rangle$	0.29	0.35	0.32	0.30	0.31	0.38
$ 13 + 12\rangle$	1.38	1.55	1.67	1.45	1.61	1.06
$ 11 + 10\rangle$	4.96	5.85	6.52	5.94	6.27	6.23
$ 9\rangle$	11.74	13.41	13.55	12.03	12.54	11.20
$ 8\rangle$	0.11	0.29	0.36	0.22	0.23	0.29
$ 7\rangle$	0.58	0.51	0.56	0.48	0.58	0.64
$ 6\rangle$	6.26	6.03	6.64	5.92	6.32	6.06
$ 5\rangle$	5.61	6.19	6.87	6.10	6.67	6.21
$ 4\rangle$	1.48	1.74	2.16	1.97	3.17	3.51

The oscillator strengths shown in Table 3.2 are of the order of 10^{-7} to 10^{-5} . A selection of values from relevant levels is graphically shown in Fig. 3.2. Particularly low oscillator strengths are found for the bands $|14 + 15\rangle$, $|8\rangle$, and also $|7\rangle$. Their experimental uncertainty is larger, but they have only minor influence on the intensity parameter determination [104]. The latter is governed by the levels with both high oscillator strengths and large reduced

matrix elements [85], most notably $|9\rangle$. A comparison of the FZ and the mean FCZ values to different host materials from the literature is given in Table 3.3. The measured values are in satisfactory consistency with the general trend observed from the other sources. The calculated oscillator strengths determined with Eq. (3.1.2) are tabulated in Table 3.4 for reference. They show a similar behavior as the measured values. From the relationship between the two, the JO parameters are calculated in section 3.2.2.

Table 3.3: Measured oscillator strengths of FZ glass and the mean of the FCZ samples in comparison to values derived in the literature for neodymium in different host [104].

SLJ manifold	$(f_{\text{meas}} - f_{\text{md}})/10^{-6}$		
	$\langle \text{FCZ} \rangle$	HClO ₄ -DClO ₄	NdCl ₃
$ 14 + 15\rangle$	0.33	0.50	0.36
$ 13 + 12\rangle$	1.47	2.33	1.90
$ 11 + 10\rangle$	6.16	7.01	5.80
$ 9\rangle$	12.55	9.76	8.30
$ 8\rangle$	0.28	0.15	0.14
$ 7\rangle$	0.56	0.65	0.51
$ 6\rangle$	6.19	8.90	7.60
$ 5\rangle$	6.41	8.84	7.70
$ 4\rangle$	2.51	2.56	2.30

Table 3.4: Calculated oscillator strengths f_{ed} for the glass and glass ceramics samples with different nanocrystal sizes in comparison.

SLJ manifold	$f_{\text{ed}}/10^{-6}$					
	FZ	ini	240 °C	250 °C	260 °C	270 °C
$ 14 + 15\rangle$	0.52	0.69	0.81	0.74	0.87	0.93
$ 12 + 13\rangle$	1.06	1.22	1.39	1.25	1.39	1.43
$ 10 + 11\rangle$	4.39	5.15	5.74	5.17	5.67	5.80
$ 9\rangle$	11.78	13.46	13.61	12.08	12.05	11.23
$ 8\rangle$	0.13	0.14	0.15	0.14	0.14	0.14
$ 7\rangle$	0.49	0.49	0.55	0.49	0.50	0.50
$ 6\rangle$	6.16	6.14	6.61	5.87	5.87	5.70
$ 5\rangle$	5.98	6.41	7.17	6.42	6.82	6.87
$ 4\rangle$	1.89	2.41	2.79	2.54	2.92	3.09

The measured oscillator strengths all increase by between 10 to 20% upon the composition change from the FZ to the FCZ glass. Exceptions are $|7\rangle$ and $|6\rangle$, which seem to stay constant over all samples within the experimental uncertainty of approximately 5%. For the former and also for $|8\rangle$, which increases by over 150%, the experimental uncertainty is really high due to their weak electric dipole interaction. As already mentioned this does not pose any further problems as their influence on the intensity parameters is also very weak.

Over the different glass ceramics, the measured oscillator strengths either stay approximately constant or decrease again towards higher nanocrystal sizes with the exception of $|4\rangle$, which almost doubles. Although $|7\rangle$ indeed increases, this is again within reasonable uncertainty.

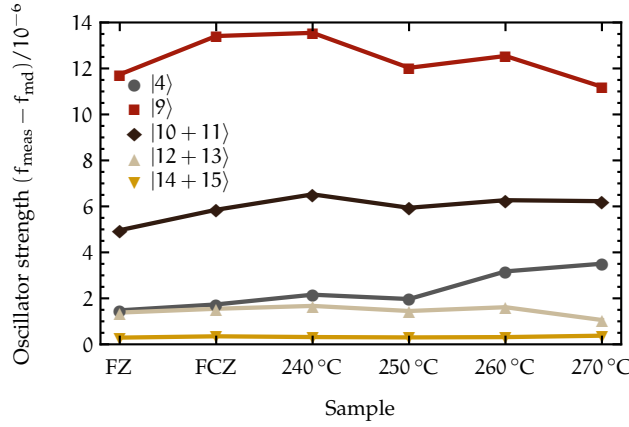


Figure 3.2: Selected measured oscillator strengths $f_{\text{meas}} - f_{\text{md}}$ for the FZ and FCZ glass and the different FCZ-c glass-ceramic samples with different nanocrystal sizes in comparison, denoted by their respective thermal treatment temperature. The values are given in units of 10^{-6} .

3.2.2 Intensity parameters

A JO analysis has been carried out [111, 112] on the basis of the oscillator strengths determined in the previous section. The phenomenological parameters Ω_λ deduced from these show small root mean square deviations and are therefore assumed sufficiently accurate [113]. The transitions involving the $|16\rangle$ to $|20\rangle$ are partly observable in Fig. 2.5 but were not included in the calculations as all of them are located above $25\,000\text{ cm}^{-1}$ and are hence superposed to the UV absorption edge of the matrix. The general peak assignment is given in Table 2.2 and is consistent with the usual classifications found in the literature [80–83].

Figure 3.3 and Table 3.5 show the phenomenological parameters Ω_λ as determined for the different nanocrystal sizes. Also included in the figure are the values for the FZ reference glass and for the untreated FCZ precursor glass. The table also encompasses values from the literature that were derived for very similar glasses and other crystalline or non-crystalline host materials for comparison.

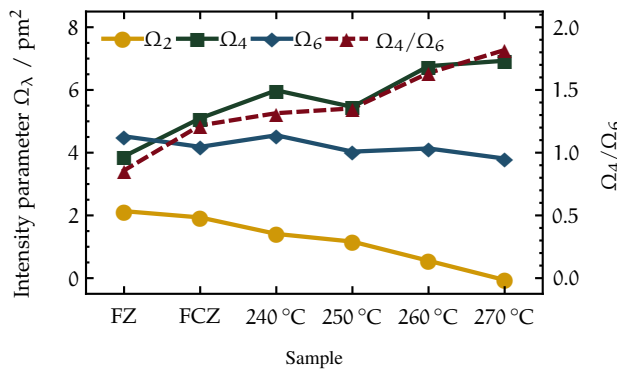


Figure 3.3: Change of Ω_λ with thermal treatment temperature and thus nanocrystal size. Also included is the so-called spectroscopic quality factor Ω_4/Ω_6 . The samples with no BaCl_2 or non-grown nanocrystals are also shown to emphasize the trends.

Table 3.5: Intensity parameters for neodymium in different hosts. Also included are the values obtained in this work for the FZ and FCZ glasses and the FCZ-c glass ceramics with differently sized nanocrystal.

Host	Ω_2/pm^2	Ω_4/pm^2	Ω_6/pm^2	source
CaF ₂	0.87	3.44	9.47	[114]
Lu ₃ Sc ₂ Ga ₃ O ₁₂	0.08	2.84	3.14	[105]
YAG	0.20	2.70	5.00	[115]
60 PbO–20Bi ₂ O ₃ –20Ga ₂ O ₃	2.37	3.77	4.86	[82]
ED2 glass	3.30	4.68	5.18	[116]
BiCl ₃ –KCl	5.70	6.60	4.40	[117]
ZnCl ₂ –KI	2.20	8.10	5.00	[117]
ZnCl ₂ –BaCl ₂ –KCl	4.97	7.39	5.12	[9]
diluted acid	1.20	6.44	10.20	[104]
ZBN	1.95	3.65	4.17	[84]
ZBL	1.93	3.80	4.35	[84]
ZBLA	1.10	3.80	5.53	[118]
ZBLAN	1.76	3.08	3.67	[119]
ZBLAN	2.66	3.05	4.08	[120]
ZBLAN	2.37	3.77	4.86	[82]
ZBLAN	2.10	3.71	4.62	[121]
FZ1	2.14	3.88	4.52	this work
FCZ1	1.93	5.10	4.19	this work
FCZ1-c, 240 °C	1.41	5.99	4.55	this work
FCZ1-c, 250 °C	1.16	5.46	4.03	this work
FCZ1-c, 260 °C	0.55	6.76	4.13	this work
FCZ1-c, 270 °C	–0.06	6.93	3.81	this work

The Ω_λ derived in this work for the FZ glass are generally close to the values from the literature for ZBLAN, but usually the chemical composition differs slightly. The untreated FCZ glass is also similar, but especially Ω_4 is larger. It compares well to the ZnCl₂-based glasses, for example [9, 117]. The Ω_2 of the FCZ-c samples with nanocrystals are more similar to the values from crystalline hosts, such as CaF₂, the gallium garnet Lu₃Sc₂Ga₃O₁₂ or the YAG laser host [105, 114, 115].

For ZBLAN, similar glasses and several crystals, the Ω_λ follow the rule $\Omega_6 > \Omega_4 > \Omega_2$ [114]. This condition was met for the FZ sample. With the chemical composition change from FZ to FCZ glass, the relation is different. With growing nanocrystals the deviation from the rule becomes even stronger and $\Omega_2 < \Omega_6 < \Omega_4$ sets. The spectroscopic quality factor Ω_4/Ω_6 correlated to the structural properties of the medium is an often-used measure for the evaluation of stimulated emission of a laser medium [114]. Here, it gradually increases from 0.9 to 1.0 in the glasses to about 1.5 in the glass ceramics.

3.2.3 Einstein coefficients

The radiative decay rates were calculated from the intensity parameters following Eq. (3.1.4) and Eq. (3.1.5) [111]. The total radiative decay rates are summed up in Table 3.6. These values mean the rate at which the total

Table 3.6: Calculated radiative decay rates A_{SPE} for different nanocrystal sizes. In the case of level groups, the common radiative decay rate was calculated from Boltzmann statistics. The results for the FZ glass and the FCZ glass without nanocrystals (ini) are included for comparison. The glass ceramics were abbreviated with their treatment temperatures.

j⟩	Radiative decay rate $A_{\text{SPE}}/\text{s}^{-1}$							$\sigma_{\text{rel}}/\%$
	FZ	ini	240 °C	250 °C	260 °C	270 °C	mean	
1⟩	6	6	7	6	7	6	6	9
2⟩	25	27	28	25	27	21	26	10
3⟩	31	33	36	32	33	27	32	9
4⟩	2166	2588	2916	2656	2969	2915	2702	11
5⟩	1651	1912	2152	1932	2168	2107	1987	10
6⟩	3011	3289	3658	3265	3540	3362	3354	7
7⟩	2105	2244	2486	2232	2381	2270	2286	6
8⟩	213	255	275	241	261	242	248	9
9⟩	7186	8687	9011	8032	8528	7784	8205	8
10⟩	1713	1985	2065	1844	1942	1802	1892	7
11⟩	6940	8476	8878	7954	8624	8118	8165	8
12⟩	1129	1264	1349	1234	1317	1241	1256	6
13⟩	26 121	31 477	32 660	29 639	31 773	29 506	30 196	8
14⟩	3703	4777	5488	4983	5879	5873	5117	16
15⟩	1259	1539	1760	1595	1842	1819	1636	14

population of the excited state level decays through any of the potential radiative decay channels. What part of the population is transported to the ground state or any particular other lower lying level is not determined by the branching ratios and not shown in this table. A selection of particularly interesting branching ratios is given in appendix A.3.1, but the whole details were published separately [112].

In the case of level groups – in contrast to isolated levels such as |4⟩ – the total decay rate was determined from a Boltzmann weighting with Eq. (3.1.6) and Eq. (3.1.7). Particularly important rates from Table 3.6 are plotted in Fig. 3.4.

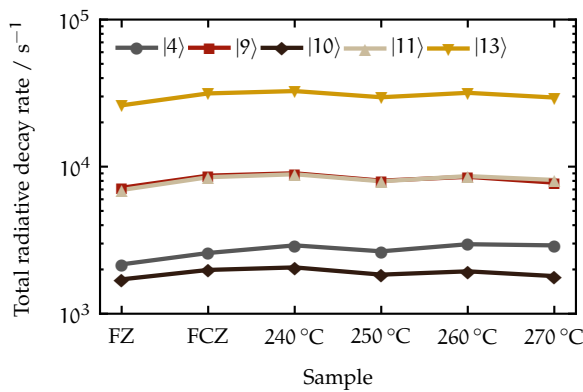


Figure 3.4: Selection of total radiative decay rates over the sample type. The rates stay approximately constant for all samples.

From the figure and table, it can be seen that the transitions of the low lying levels (|1⟩ to |3⟩) are very improbable with rates below 100 s^{-1} . Also,

$|8\rangle$ has a comparably weak radiative decay probability. While most of the remaining levels decay on the time scale of hundreds of μs (corresponding to rates of some 1000 s^{-1}), the rate of level $|13\rangle$ is the largest and level $|13\rangle$ one order of magnitude more probable to decay radiatively within a fixed period of time than most of the other levels.

Disregarding the levels below the metastable level for now, the second observation from the figures is that all rates grow around 5 to 30% upon the composition change from FZ to the FCZ glass matrix. Over the thermal treatment towards glass ceramics, most of the rates remain approximately constant within the conservative JO margin of error of 10%. There are however some exceptions, most notably $|4\rangle$ increasing by almost 15%, as well as $|14\rangle$ and $|15\rangle$, who both increase by approximately 20% with the increasing nanocrystal size [75, 111]. In addition, it is worthy to note that next to $|4\rangle$, the level $|5\rangle$ also increases and while $|6\rangle$ and $|7\rangle$ remain equal, the rates of levels $|8\rangle$ to $|13\rangle$ all decrease over the annealing temperature.

Another exception is the single hypersensitive ($\Delta J \leq 2$, $\Delta L \leq 2$, and $\Delta S = 0$) neodymium transition, namely $|9\rangle \rightarrow |0\rangle$. Its decay rate does a large jump of around 20% along the composition change from FZ to FCZ. This trend is also followed by the JO parameter Ω_2 (see Fig. 3.3 and Table 3.5), in agreement to observations [122] claiming that it reflects the peculiar sensitivity of the hypersensitive transitions to the local RE environment. The mathematical correlation is also obvious from the exceptionally large reduced matrix element $|\langle i || U_2 || j \rangle|^2$ for $|9\rangle$ [85]. Thermal treatment has only a weak effect though, and the rates stay of the order of magnitude already published for a different host material [123].

The already mentioned monotonic decrease of Ω_2 for growing nanocrystal sites implicates both high ionicity and relatively high symmetry in the local RE environment. This gives rise to the expectation that at least parts of neodymium are located near nanocrystal interfaces or have even been included into them. In contrast to this, there are hints in the literature [8, 17] that erbium does not enter BaCl_2 nanocrystals, although this has been shown for BaF_2 nanocrystals inside an oxyfluoride glass matrix [63]. An inclusion of neodymium into this material was also shown [62].

3.3 EXPERIMENTAL VERIFICATION OF JUDD-OFELT RESULTS

3.3.1 Overview

As there is no prior knowledge for the validity of the JO results apart from fair root mean square deviations of the order of values from similar analysis in the literature, several independent approaches have been chosen to gather evidence for the the JO intensity parameters, Ω_λ , and also the Einstein coefficients for SPE A_{SPE} that were derived from them.

First of all the general working mechanism of the procedure was tested by carrying out a JO analysis on the plain ZBLAN base glass (FZ). The intensity parameters as shown in Table 3.5 are in good agreement to results of the same or a similar system in the literature. Having established the

correct method with the reference sample, the situation was extended to the untreated precursor glass for the glass ceramics (FCZ). The results compare to the literature quite similarly.

Parts of the analysis results for the glass ceramics were then checked against two independent experiment-based approaches. On of those, the McCumber theory, links emission cross sections to Einstein coefficients with the Füchtbauer-Ladenburg equation and gave a direct comparison of a subset of the coefficients with a good agreement to the JO results. Furthermore, time-resolved spectroscopy of photoluminescence decays were employed as another approach. This was possible whenever the decay constant is directly related to the Einstein coefficient without affection by other processes, as is the case for the decay of the metastable state.

The results from any of the mentioned complementary approaches gave a convincing agreement to the JO results as elaborated in more detail in the following.

3.3.2 Photoluminescence lifetime measurements

As discussed previously, the discussed levels generally favor nonradiative decay by the emission of several phonons over radiative decay, given the comparably large MPR rates for energy gaps of several hundred cm^{-1} . It is clear that the level $|4\rangle$ with its remarkably large energy gap makes up for the one notable exception [124], which enables for a direct comparison of the JO-derived decay rate to experimental photoluminescence lifetime data. This becomes possible as for energy gaps of about 5400 cm^{-1} phonon emission is improbable and hence the radiative quantum efficiency amounts to unity. While there is in fact a non-negligible probability for phonon absorption, the inverse process to MPR, which will be discussed in more detail later in section 4.1.2, the radiative decay rate is expected to be approximately equal to the measured photoluminescence decay rate in this peculiar case.

Table 3.6 showed FCZ(-c) $|4\rangle \rightarrow |0\rangle$ decay rates between 2600 s^{-1} and 3000 s^{-1} . These are comparable to, but smaller than those in the FZ glass at about 2200 s^{-1} . Although almost all values in Table 3.6 vary slightly with growing nanocrystals, they still stay almost constant within the accuracy range expected from the JO theory.

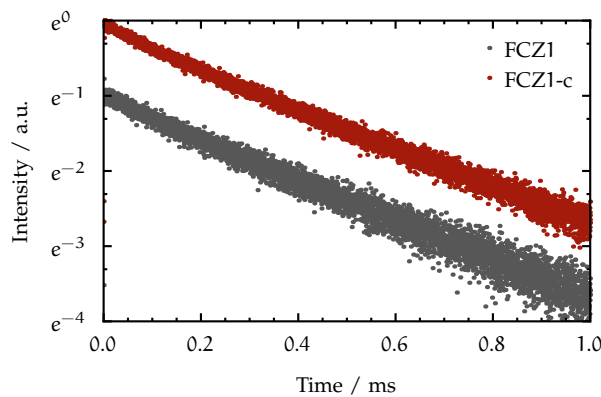


Figure 3.5: Spontaneous decay at 870 nm upon indirect excitation via $|5\rangle \leftarrow |0\rangle$ at 800 nm with 10 mW.

Due to the insignificance of phonon emission from $|4\rangle$, huge changes of the experimental lifetimes with the nanocrystal size are not anticipated. In fact, lifetime measurements yield decay rates between 2400 s^{-1} and 2700 s^{-1} for the different FCZ(-c) samples. In Fig. 3.5, two decays at about $375 \mu\text{s}$ and $395 \mu\text{s}$ for the precursor (FCZ) and the glass ceramic (FCZ-c) are shown, respectively. For the FZ glass, a lifetime of approximately $450 \mu\text{s}$ is found.

The decay rates obtained from JO results for all samples differ from those measured by less than 10%, and are therefore directly verified by the lifetime measurements. Still, a small and actually positive deviation can be observed, which is however not related to the Einstein coefficients. A similar observation was found by other authors [121] earlier. Considering

$$\tau^{-1} = \underbrace{W_{\text{PE}}}_{\approx 0} + A_{\text{SPE}} \approx A_{\text{SPE}}$$

and the observation $\tau^{-1} < A_{\text{SPE}}$ leads to the conclusion that another contribution is involved, but with opposite sign. For $|4\rangle$ this is clearly a phonon absorption to $|5\rangle$,

$$\tau^{-1} = A_{\text{SPE}} - W_{\text{PA}},$$

giving rise to a thermal coupling of the two levels. This effect is usually insignificant, especially for all the other, shorter living levels. In the case of the metastable level however, it may not be neglected. Absorption of phonons will therefore be considered in the rate equation model setup later, together with a general discussion of the thermal coupling effect, in section 4.1.2.

In general, the Einstein coefficients for spontaneous emission from the JO theory are verified quite well by the lifetime measurements. However, this was only possible for the levels comprised by the thermal coupling in the vicinity of $|4\rangle$. Unfortunately, all other decays are strictly dominated by phonon emission and thus, lifetime measurements cannot confirm the JO rates in these cases. As another complementary venue to this problem, an approach involving the McCumber theory will be chosen in the following to gather further evidence for the correctness of the JO rates.

3.3.3 McCumber theory and Füchtbauer-Ladenburg-Equation

The McCumber theory [125, 126] delivers a relation between absorption and emission cross section spectra,

$$\sigma_{ji}(\nu) = \sigma_{ij}(\nu) \exp\left(-\frac{h\nu - \mu}{k_{\text{B}}T}\right), \quad (3.3.1)$$

which is to be evaluated for room temperature measurements. As a generalization of the Einstein coefficient approach the validity of Eq. (3.3.1) holds under the assumption of a quick set-in of a Boltzmann-distribution of the electronic population [127]. This requirement is met whenever the energy spacing between the Stark components of a multiplet are small and non-radiative processes occur of the order of nanoseconds or faster.

With Eq. (3.3.1), the emission cross section σ_{ji} for the transition from an excited level j to a lower level i , especially to the ground state ($i = 0$), can be calculated from the corresponding absorption cross section σ_{ij} . The

chemical potential μ equals the free net energy for an excitation from a Stark component in i to one in j at constant temperature [125].

The equilibrium population densities N_i and N_j of the two involved levels are Boltzmann distributed,

$$\frac{N_j}{N_i} = \exp\left(\frac{-\mu}{k_B T}\right).$$

An estimation of μ assuming equidistant Stark levels proceeds with

$$\frac{N_i}{N_j} = \frac{\sum_{m=0}^{\nu_S-1} \exp\left(-\frac{m}{\nu_S-1} \Delta E_i\right)}{\exp(-E_0) \sum_{m=0}^{\nu_S-1} \exp\left(-\frac{m}{\nu_S-1} \Delta E_j\right)}.$$

The population densities N are integrated over all Stark levels m within each of the multiplets i and j [125, 126]. Therefore, $\frac{1}{\nu_S-1} \Delta E_k$, with ΔE_k the total energy separation ($k = i, j$), is the individual component spacing. The inter-multiplet separation between the lowest components of i and j is denoted E_0 . The number of Stark levels ν_S per multiplet is related to the number of f -electrons of the ion:

$$\nu_S = \begin{cases} 2J + 1 & \text{even} \\ J + \frac{1}{2} & \text{odd} \end{cases}.$$

For trivalent neodymium (Nd^{3+}) the electronic configuration is $[\text{Xe}]4f^3$ and hence, $\nu_S = J + 1/2$. Singly ionized ($[\text{Xe}]4f^4 6s$) and neutral ($[\text{Xe}]4f^4 6s^2$) neodymium however, have an even number of Stark levels and $\nu_S = 2J + 1$. The intra-multiplet spacing ΔE_k was estimated according to Ref. [126]. Here, the distance E_0 is approximated with the mean value of the centre of mass emission and absorption positions.

With this information and the above-made simplifications, Eq. (3.3.1) allows the immediate calculation of the shape of emission cross sections from the available absorption cross section spectra. With these, a direct comparison to experimentally derived emission spectra is possible as a check for the validity of the model established so far. Moreover, a rescaling of the spectra involving the Fuchtbauer-Ladenburg equation [116],

$$A_{\text{SPE}} = \frac{8\pi n^2}{c^2} \int_{\nu_1}^{\nu_2} \nu^2 \sigma_{ji}(\nu) d\nu, \quad (3.3.2)$$

yields absolute cross sections from the naturally relative experimental emission spectra [128]. If the radiative decay rate A_{SPE} is unknown, but both absorption and emission spectra are at hand, it is possible to calculate A_{SPE} from the ratio of the two. Note that radiation trapping [129] might be responsible for a few percent error in the decay rates [116] in some cases, depending on the thickness of the samples. It was neglected here, as only thin samples ≤ 1 mm were used.

Several emission cross section spectra were calculated with Eq. (3.3.1). Experimental emission cross section were rescaled to the calculated spectra with Eq. (3.3.2) to determine A_{SPE} . Fig. 3.6 shows the $|5\rangle \rightarrow |0\rangle$ cross sections for FCZ1 and FCZ1-c. For these a decay rate of 1928 s^{-1} and 2030 s^{-1} were determined, respectively, which is in fairly good agreement to the results from the JO theory, namely 1930 s^{-1} and 2168 s^{-1} . Note also that both the

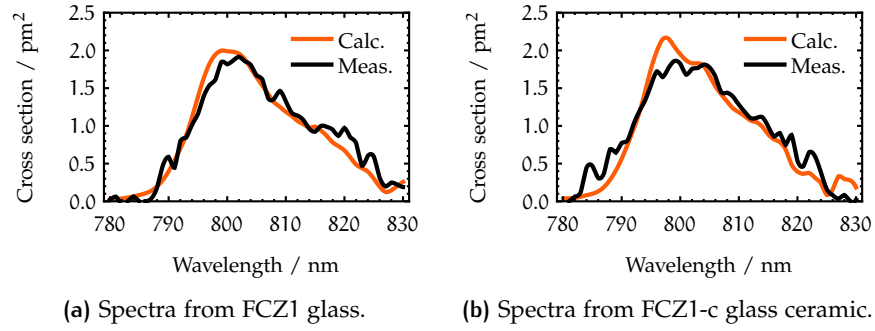


Figure 3.6: Comparison of calculated emission cross section spectra of the $|5\rangle \rightarrow |0\rangle$ transition at 800 nm in FCZ1 and FCZ1-c to measured spectra that were rescaled to absolute units with Eq. (3.3.2).

theoretical and the experimental spectra of the FCZ-c samples (see Fig. 3.6b) feature a Stark splitting.

$|4\rangle$ could not be calculated to a satisfactory quality. A similar case was explained elsewhere [130] with the high bandwidth of this level (strong inhomogeneous broadening in this amorphous host) causing the McCumber theory to fail. Also the calculations for the level groups such as $|9\rangle$ and $|10\rangle$ were not possible, although better prediction accuracy is expected from McCumber theory for the shorter wavelengths since errors in the baseline fitting are not amplified as much by Eq. (3.3.1) as for the shorter wavelengths [127]. The reason for this are the numerous overlap options present in the level scheme. For example, the emissions from $|9\rangle \rightarrow |0\rangle$ very well overlaps $|10\rangle \rightarrow |1\rangle$. And due to the almost equal spacing between the individual J-levels of 4I_J ($J = 9/2, 11/2, 13/2, 15/2$), several of such overlaps between non-ground-state transitions and the ground-state transition are found. McCumber calculation was also not possible for the remaining, weak emission bands, where the measured spectra had vanishing or had a bad signal to noise ratio. Nevertheless, the alternative approach of using the McCumber theory together with Eq. (3.3.2) confirmed a complementary part of the JO results for the radiative decay rates.

3.4 DISCUSSION

3.4.1 Nanocrystal growth and inclusion of neodymium

NANOCRYSTAL GROWTH It is unquestioned that growing nanocrystals off from the established matrix of a stable glass has several consequences for the glass itself. These material transformations can be separated into visible effects on the RE ion embedded into the matrix, and into effects visible from the glass matrix. In either way neodymium ions aid as a sensor to the material transformation as they are affected by the surroundings in a comparably weak but meaningful way. Therefore, neodymium and RE ions in general serve as a probe for material transformation. The major arguments compiled here are grouped schematically in Fig. 3.7 for a quick overview.

One particularly visible effect of nanocrystal growth affecting the glass matrix is the drastic change of the spectral transmittance of the samples from

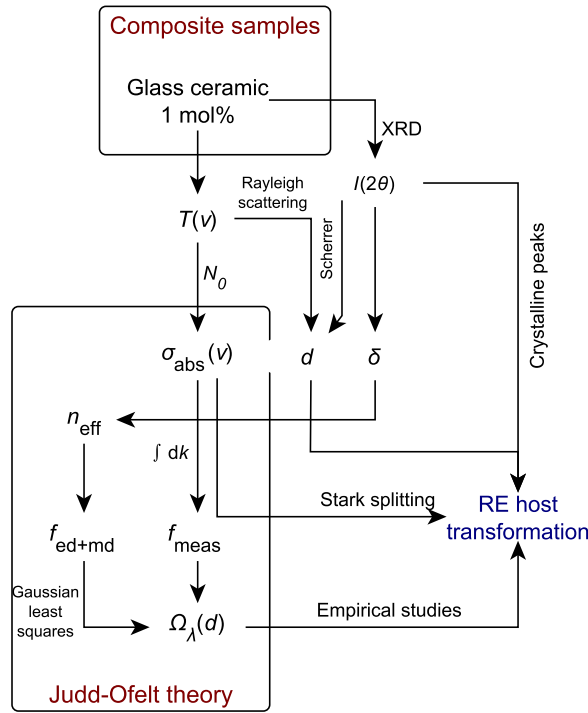


Figure 3.7: Schematic of the relations between the experimental arguments that hint at the inclusion of neodymium into the BaCl_2 nanocrystals.

transparent to milky-white. If neodymium did not serve as a nucleating agent for the nanocrystals, the suspected case in another glass ceramic [62], this effect would be independent of any dopants in the matrix. Fig. 2.7 shows how the net transmittance is reduced upon nanocrystal growth following the Rayleigh-scattering law according to

$$T = \frac{I}{I_0} \propto \lambda^{-4}.$$

In section 2.4.1 this fact has been exploited to determine the nanocrystal size from a Rayleigh-scattering based model independent of the usual Scherrer formalism. The result drawn there is that higher annealing temperature steps that lead to larger nanocrystals generate a certain nanocrystal size dependence obvious from the Rayleigh-scattering.

Furthermore, the evaluation of X-ray diffraction patterns of the different samples in section 2.3.2 gives direct evidence for the growth of hexagonal nanocrystals. It also directly verifies the sizes derived from Rayleigh-scattered transmittance data. Crystalline peaks superpose the amorphous glass background after thermal treatment, as clearly seen in Fig. 2.3. The volume fraction δ determined from the peak integrals in comparison to the total integral are in consistence to the actual chemical composition of the precursor glass (see also section 2.4.1) and make it obvious that the whole BaCl_2 from the glass melt is gathered for the growth of hexagonal crystals within the glass. These volume fractions are of the order of 20%. Apparently a significant fraction of neodymium ions that are assumed to be in homogeneous distribution over the glass bulk will be located in the vicinity of, at the interface to, or built into a nanocrystal.

NEODYMIUM NANOCRYSTAL INCLUSION RE inclusion into the FCZ-c glass ceramics was already shown for europium [52, 53] and hints at a nanocrystal inclusion of neodymium within these matrices were also found [10, 11]. Several observations from the preceding sections foster this assumption and are gathered in the following.

The effect of a nanometric crystal with quite polar constituents, like chlorine with a strong electronegativity, is expected to exhibit a considerable static electric field (crystal field) as an ordered ionic structure. Connected to this is the splitting of the degenerated SLJ manifolds into their Stark-levels. Fig. 3.8 shows the comparison of emission spectra between the FCZ and FCZ-c samples. The slight broadening by the weak crystal field in the glass is much more emphasized in the glass ceramic and also shoulders from the individual Stark components appear. The same can be seen from the absorption cross section spectra in Fig. 3.6 and was also found in the literature [10, 11]. Note however that in the glass ceramic, contributions to the spectra arise from both neodymium within the glassy part of the matrix and from the nanocrystals which weakens the visible effect to a certain amount as the majority of neodymium in the glass ceramics is distributed among the glassy part of the matrix.

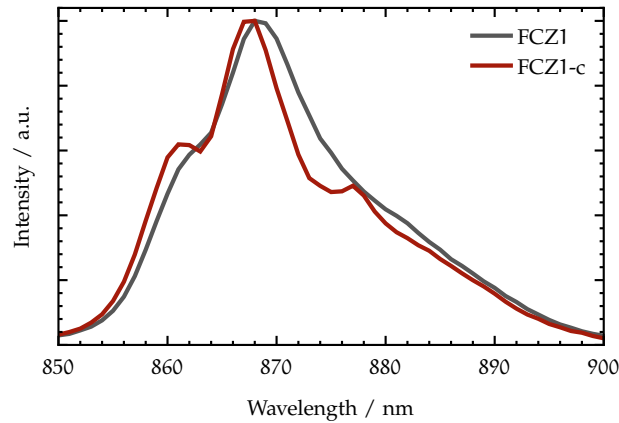


Figure 3.8: Stark effect in glass ceramics from $|4\rangle \rightarrow |0\rangle$ emission in the weakly doped precursor glass and glass ceramic. The spectra are measured upon 800 nm pulsed excitation at an average of 25 mW with 500 Hz. The sample with nanocrystals shows a much more pronounced Stark effect than the precursor glass.

The Ω_λ and calculated A_{SPE} from the FZ reference sample are in very good agreement to values from similar materials in the literature [82, 84, 118–121]. The FCZ precursor glass behaves similarly, although it has a slightly different chemical composition. A comparison of the FZ and FCZ intensity parameters shows that the addition of BaCl_2 changes the RE environment significantly. Ω_2 and Ω_4 are most affected by this. Proceeding with thermal treatment (see first FCZ-c sample, treated at 240 °C) then leads to only a slight change. This is expected as the nanoparticles are known to grow slowly at the treatment temperatures below 260 °C and change more significantly from there. As Ω_2 decreases, Ω_4 increases. At the same time Ω_6 decreases only slightly and stays roughly constant.

The Ω_λ can also be related to structural properties of the RE host environment and there are several empirical studies in the literature where the effects of host composition and choice are related to the individual intensity

parameters [83, 131–135]. In particular, Ω_4 and Ω_6 are connected to the rigidity of the host matrix and also the distortion of the RE crystal field. On the other hand, Ω_2 is interpreted as a measure for the covalency (or ionicity) of RE-halogenide bonds. Moreover, the ionicities of RE bonds are defined by the polarizabilities of the halogenide bonding partners [131]. In turn, these are determined by their electron donating capabilities and therefore connected to Ω_2 [131, 136].

Applied to the present case of neodymium in the glass ceramics, the effect of thermal treatment on the magnitudes of Ω_λ implies that the growing nanocrystals are responsible for both an increase of ionicity (low covalency) [137] and for a rising degree of symmetry in the local environment of neodymium. Furthermore, the rigidity of the host matrix increases. This is also expected given its transformation into a partially crystalline host, which is usually accompanied by low Ω_2 values (cf. the distinctively small Ω_2 for several crystalline hosts in Table 3.5).

Neodymium's hypersensitive transition ($\Delta J \leq 2$, $\Delta L \leq 2$, and $\Delta S = 0$) is $|9\rangle \rightarrow |0\rangle$. As it is mainly determined by the short-range crystal field, it is most sensitive to alterations of the local environment. Similar to observations for neodymium in an oxyfluoride glass ceramic [62], the dependence of the oscillator strengths from this transition on the thermal treatment temperature is slightly more monotonic than that of the others. Fig. 3.9 emphasizes the connection between Ω_2 and the oscillator strengths of the hypersensitive transition. Their close correlation is another hint at the inclusion of neodymium into the nanocrystals [62].

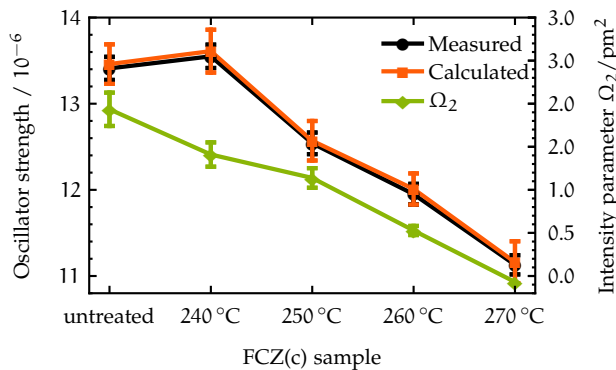


Figure 3.9: Correlation between oscillator strengths of the hypersensitive transition and the intensity parameter Ω_2 with increasing nanoparticle size.

The variation of the spectroscopic quality factor Ω_4/Ω_6 from 0.9 to 1.0 in the glasses to about 1.5 in the glass ceramics (see Fig. 3.3) endorses this conclusion even further as the same values were found in Refs. [9, 117]: 0.6 to 0.9 for fluoride glasses and about 1.5 for chloride hosts. It was also known that an increasing Ω_4/Ω_6 is accompanied by a change of the branching ratios of the metastable level's emissions in a way favouring $\beta_{4,0}$ over $\beta_{4,1}$ [117]. As Eq. (3.1.2) implicates, it determines these branching ratios as they have a vanishing reduced matrix element of second order, $\langle i||U_2||j\rangle$ [85]. This is also found in the present case, where $\beta_{4,0}$ increases from 47 to 53 % and $\beta_{4,1}$ decreases from 44 to 40 % along the thermal treatment temperature, respectively (see appendix A.3.1).

A final argument for the nanocrystal inclusion is shown by the blue shift of the neodymium photoluminescence, e. g. of up to 5 nm for the bright $|4\rangle \rightarrow |1\rangle$ transition. As again deduced from empirical studies [83, 135, 138, 139], this confirms the increase of the ionicity between neodymium and its halogenide bonding partner. The same observation is also endorsed by the weak dependence of Ω_6 on the ionicity as reported analogously in Ref. [131]. Furthermore, in a comparison between neodymium line positions in bulk BaCl_2 and in FCZ-c glass ceramics, a significant blueshift was also found [11]. There, a selective excitation in resonance to both resulting peaks even allowed for a switching of the Stark splitting in the FCZ-c by the choice of the respective excitation wavelength. This was thus treated as a direct evidence for the nanocrystal inclusion of neodymium in the glass ceramics.

3.4.2 On Judd-Ofelt accuracy and error margins

The accuracy of JO results is generally of the order of 10 to 25 % [99, 140, 141]. Ref. [122] discusses the influence of the main simplifications made in the derivation of the JO theory on this error. No specific problems are expected for the present system. Contributions to the JO error that arise from experimental insufficiencies related to the experimental data are summarized in the following.

An often-cited JO obstacle is associated with the choice of the minimization quantity for determining the Ω_λ parameters [90, 142, 143]. A different choice of this quantity implies a different calculation method, which is finally detrimental to reliably comparing Ω_λ parameters from different sources. What method is the most sensible was discussed elsewhere [90, 142, 143]. In this work the matrix method of Ω_λ -determination has been employed.

Considering the mathematical avenue to the Ω_λ determination, the actual number of levels included into the analysis also affects the intensity parameter calculation [90, 99]. The accuracy would generally benefit when the analysis comprises as many individual absorption bands as possible. However, due to experimental reasons, it is not always possible to include bands from the whole optical spectrum of a given RE ion. In this work, the absorption bands in the UV could not be included as they are strongly superposed to the host matrix absorption edge. To test for the stability of the Ω_λ solutions found here, it was iteratively tested whether the omission of any band(s) leads to dramatically different results. From this it was found that the set of bands included here, as found also in the literature [144], was quite stable. From this stability test it also turned out that indeed the strong lines dominate the intensity-parameter determination. This also implicates that a good description of the major bands usually assures a sufficiently well-determined set of intensity parameters [99]. Based on the results found here, this condition is definitely met in the present work. Note that a *weak* band on the other hand may be associated either to a small measured oscillator strength or small reduced matrix elements.

While mostly the root mean square error is determined as a measure for the JO error, it still gives no convincing argument for the reliability of the JO description of the system. According to several works in the literature [99, 145], only a contrasting juxtaposition of simulated to measured GSA

cross sections is a reliable measure for the quality of JO calculations. This procedure is shown for the FZ1 sample in Fig. 3.10.

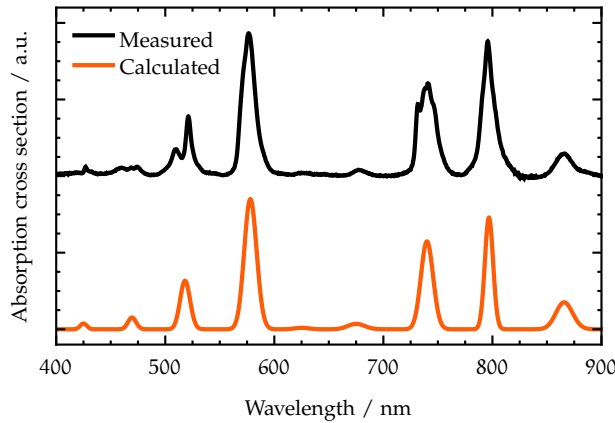


Figure 3.10: JO-simulated and measured GSA cross section spectra of FZ1.

From the figure it becomes obvious how the experimental data were mapped to get a simplified model containing the vital information. Especially the level grouping can be seen where the oscillator strengths of individual nearby absorption lines was mapped to single common oscillator strengths. Note that the integrals in the picture do not need to be equal.

Further, particularly problematic for the JO accuracy are the strongly inhomogeneously broadened lines. In these amorphous hosts, only one global dipole strength can be determined for each absorption band. Individual Stark components of SLJ manifolds usually cannot be independently considered [99]. Moreover, in some cases even whole SLJ manifolds are not individually resolved from nearby levels.

There are also error sources directly associated to the experiments: The baseline determination necessary for the calculation of the oscillator strengths from absorption spectra can pose obvious errors in particular in the case of the weak levels. Moreover, due to the strong line broadening and partially overlapping tails of approximately Gaussian absorption bands, even the choice of the integration intervals (cf. Fig. 3.10, experimental curve), over which the spectra are integrated is an error source. The calculation of absorption cross sections takes the number density of neodymium N_0 in the samples as an input parameter. Its value was estimated for each sample from its composition and assumed to be homogeneous throughout the host matrix. Therefore it is immediately attached to all errors in the composition, such as the weighing or stoichiometric composition.

An important error source is hidden in the local-field correction factors χ_{ed} and χ_{md} (Eq. (3.1.3)). The refractive index n enters here significantly, especially for χ_{ed} . Varying n could therefore lead to notably different A_{SPE} , even for identical Ω_λ . In this work, the refractive index of the FZ and the FCZ precursor glasses were estimated by literature values for ZBLAN. For smaller compositional changes throughout the family of FZ glasses including ZBLAN this is unproblematic. Upon the transition to FCZ glass, 10% of the fluorine are replaced by chlorine. It may be subject to a more detailed discussion whether this is actually a small compositional change. Moreover, in the case of FCZ1, and even worse in FCZ5, the neodymium content itself

might also affect the accuracy of the refractive index of the glasses. For moderate doping levels however, only little influence of neodymium content on the refractive index is found, and the maximal induced error is within the already known JO margin of error. In the case of the glass ceramics, a refractive index based on the Garnett model was used. The prerequisite of small volume fractions ($\delta_i \ll 1$) was fulfilled. Also, there are also no indications that the nanocrystal shape deviate significantly from a spherical shape – the second requirement of the Garnett model.

Errors related to the application of the McCumber theory are basically the same as the experimental errors from the JO analysis: baseline uncertainties, reabsorption of fluorescence, too low signal-to-noise ratio. The latter is however partly remedied with the McCumber theory, since in the analysis scheme employed here, the absorption cross section was calculated from the emission cross sections which is usually equipped with much better signal strengths.

Summing up, there are several possible error sources that make up for a total JO uncertainty of around 10 to 25 % [140, 141] when evaluated pessimistically. This error comprises the Ω_λ parameters and extends as far as to the JO-derived Einstein coefficients for SPE (A_{SPE}). However, judging from the fact that the major decay mechanism is generally the emission of phonons with rates orders of magnitude larger than most of the radiative rates, such errors in the JO-derived quantities lose their relative significance. Nonetheless, in order to verify the correctness of the overall method setup in this work, the analysis intentionally included an FZ reference sample. This reference test showed an excellent agreement to several works in the literature.

3.5 SUMMARY

OSCILLATOR STRENGTHS The theoretical oscillator strengths for electric dipole and magnetic dipole interactions were calculated for optical transitions in trivalent neodymium. While electric dipole oscillator strengths are of the order of 10^{-7} to 10^{-5} , the magnetic-dipole values range between 10^{-10} to 10^{-8} for only a few SLJ manifolds and are zero for the remainder. From absorption spectroscopy, the experimental oscillator strengths comprising both the electric and magnetic dipole contributions, were determined. In both cases, theoretical and experimental, the largest values were found for |9). Further important levels are |11 + 10), |6), |5), |4), and |13 + 12) with medium scale values. The remaining were insignificant at last considering the different sources of error. The list of possible errors encompasses most importantly errors related to the baseline determination or the huge inhomogeneous line broadening and is responsible for a general uncertainty of the order of 10^{-7} for the measured oscillator strengths. While this might be significant for the smaller oscillator strengths, it still has no large influence on the further JO procedure, which is dominated by the strong lines that are not prone to this type of uncertainty.

JUDD-OFELT PARAMETERS Based on the oscillator strengths, the JO intensity parameters were calculated with a matrix method for the glass-ceramic

samples with differently sized nanocrystals and the precursor glass without any nanocrystals. In the case of the glass ceramics, an effective-refractive-index model was used enabling the JO analysis of a composite material. The procedure gave very good agreement with literature values for a reference sample. The dependence of the JO parameters on the annealing temperature of the glass-ceramic samples gave, based on empirical studies, detailed insight in the alteration of the matrix surrounding parts of the neodymium dopant ions and also evidence for their inclusion into the nanocrystals: From the change of the Ω_4 and Ω_6 parameters, which are dominated by long-range interactions, changes of the bulk properties were concluded such as an increase of the rigidity of the host matrix increases. Ω_2 , which is connected to short-range effects, decreased over the annealing temperature, which means an increase of the ionicity of the neodymium bonds in place and also a local symmetry increase [62]. All these structural property changes serve as direct evidence for the nanocrystal inclusion of at least part of the neodymium ions.

EINSTEIN COEFFICIENTS With the Ω_λ parameters known, Einstein coefficients for spontaneous emission were calculated. They are of the order of 10^3 to 10^4 s^{-1} with few smaller and larger exceptions. In particular, $|13\rangle$ shows the distinctively largest value of around $3 \cdot 10^4 \text{ s}^{-1}$. Other notable values are found for $|11\rangle$ and $|9\rangle$ with around $7 \cdot 10^3 \text{ s}^{-1}$. Several experimental approaches were sought to gather proofs for the calculated Einstein coefficients, including the McCumber theory and the Füchtbauer-Ladenburg equation but also direct photoluminescence lifetime measurements. With these complementary methods, different subsets of the Einstein coefficients were independently determined and directly verified the JO results. The Einstein coefficients do not change much with the annealing temperature. While a huge effect is actually not expected due to the nature of the rare-earth's orbitals, an overall increase of the rates with annealing temperature might be related to an advancing inclusion into the growing nanocrystals. Another possibility would be the growing influence of the nanocrystal volume with respect to its surface.

4

RATE EQUATION MODEL - STOKES PROCESSES

The rate equation model established here is a non-stationary, ordinary differential equation system. The coefficients owe to SPE or phonon processes and hence describe the regular Stokes-type emissions. Their determination from experiments and theory is presented in the following [146, 147].

4.1 MODELLING STOKES PROCESSES WITH RATE EQUATIONS

The process of the analysis of the Stokes processes with the rate equation system is shown schematically in Fig. 4.1. From samples at weak doping level, the Einstein coefficients for SPE could be derived with the Judd-Ofelt (JO) theory. Absorption spectroscopy yielded the base data for the calculation of radiative decay rates and branching ratios. From these, the coefficient matrices that describe SPE are constructed. The second major part of the coefficient matrices for the Stokes processes comes from those decays where phonons are involved. The phonon coefficients are all related to a model which connects the energy gaps to phonon transition rates, the so-called energy gap law (EGL). For the glass matrix this is known from the literature [148–151].

For the glass ceramics however, an effective medium model is proposed, in which contributions to the measured decay are mixed by weighted amounts of decays from neodymium residing in the glass matrix or at the nanocrystal sites. For the nanocrystal sites, an EGL is proposed in another work [6, 152] on the basis of experimental methods shown below. Using this and the glass-ceramic Einstein coefficients from the JO theory, the effective-medium glass ceramic situation is modelled.

The validity of the respective coefficient sets is ensured by comparing the rate equation solutions to selectively pumped decay measurements. Here, the situation is modelled as follows. A femtosecond excitation pulse leads to ground state absorption of the pump radiation. From the pump level, the excitation energy is lost mainly due to multiphonon-relaxation to the next lower level, but also radiative emission to each lower-lying level. The inverse process to phonon emission is responsible for a thermal occupation mechanism of higher lying levels, but in most cases the attached probabilities are very low.

One notable exception is the metastable level, from which phonon absorption produces weak Anti-Stokes emission from the next higher lying levels generating an extended population reservoir. The experimental situation of femtosecond pulses at low repetition rates allow to exclude any excited-state absorption from the model picture as all population is relaxed to the ground state prior to each next excitation pulse. Also, the weak doping level ensures

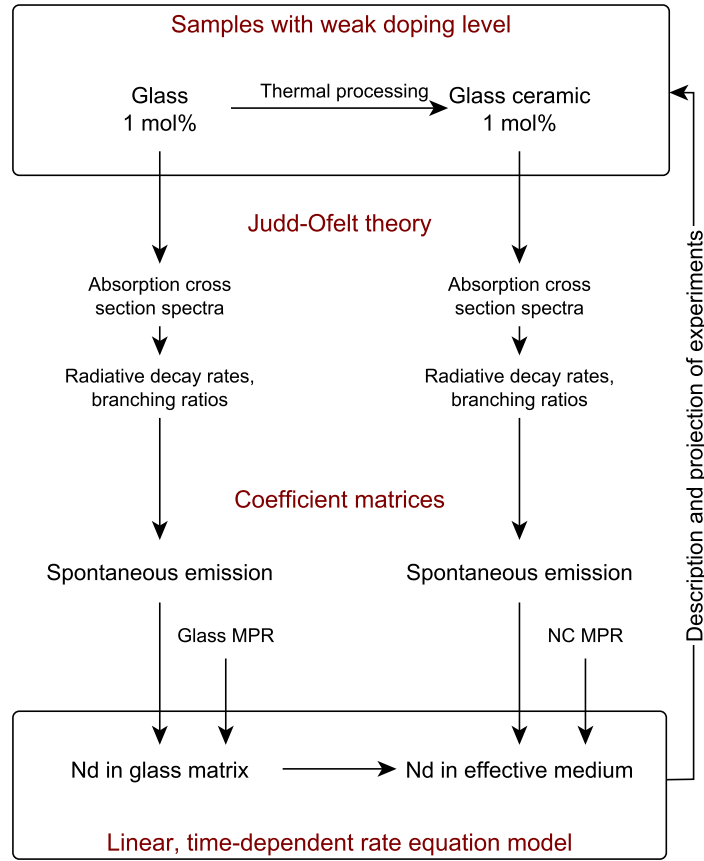


Figure 4.1: Schematic of time-dependent rate equation analysis for description of Stokes processes.

negligible energy-transfer probabilities. A good similarity of simulated and measured decay curves is found for different pumping scenarios, evidence for well-established coefficients and a correct model picture for the Stokes processes.

4.1.1 Spontaneous emission

The probability of photoluminescence is determined by the Einstein coefficients for SPE, A_{SPE} . They give the probability for an excited ion to decay radiatively by the emission of photons. The probability for a specific transition at a particular frequency, i. e., for a transition from an initial level to a particular final level is given by the branching ratios β . Both coefficients used in this work are based on the JO theory, described earlier in chapter 3. In general, the SPE contributes to the population of level $|j\rangle$ as a loss to levels $|k\rangle$ with $k < j$ and as a gain from any levels $|i\rangle$ with $i > j$ in the form

$$\left. \partial_t N_j(t) \right|_{\text{SPE}} = -A_{\text{SPE},j} N_j(t) + A_{\text{SPE},i} \beta_{ij} N_i(t),$$

where A_{SPE} is the total radiative emission rate of $|j\rangle$ and the product $A_{\text{SPE},i} \beta_{ij}$ the rate of radiative transitions $|i\rangle \rightarrow |j\rangle$ with $i > j$.

4.1.2 Processes involving phonons

OVERVIEW Non-radiative relaxations involving phonons are the dominating mechanism on the neodymium decay dynamics. Simultaneous emission of one or more phonons (PE), often denoted multiphonon relaxation (MPR) in the latter case, typically has rates between 10^4 and 10^9 s^{-1} , depending on the energy gap of the dopant and the phonon spectrum and coupling of its host matrix. The inverse process, phonon absorption (PA) must also be considered in some cases and its rates are typically two to three orders of magnitude smaller. On the other hand, radiative decay rates are of the order of 10^3 s^{-1} as discussed in chapter 3. Between near-by lying states with energy gaps of the order of or below $k_B T$, population is distributed very quickly to finally reach a Boltzmann population distribution. This is the case between Stark levels of one SLJ manifold, but also for very close SLJ manifolds, and finally is the reason for the level grouping in Table 2.2. Such level groups are treated as one level with a common oscillator strength and a combined decay rate (see section 3.1.3).

The theory of multiphonon processes has been established in the 1970s [153–156]. A successful [124, 155] phenomenological treatment was developed by Riseberg and Moos [100, 141].

ENERGY-GAP LAW In general, the probability for phonon processes depends mostly on the energy gap and further detailed properties of the individual phonon modes and electronic states are usually not significant [124]. The actual relationship between PE rate W_{PE} and energy gap ΔE is expressed in a so-called energy-gap law (EGL), which can be written as [154, 155]

$$W_{PE} = C \cdot \exp(-\alpha \Delta E). \quad (4.1.1)$$

While C is the zero-gap extrapolated PE rate, α is related to the strength of the electron-phonon coupling via [155, 156]

$$\alpha = \frac{1}{\hbar\omega} \left(\ln \frac{p}{g(\bar{n} + 1)} - 1 \right).$$

Here, $p = \Delta E / \hbar\omega$ is the (average) number of $\hbar\omega$ -phonons emitted, which defines the order of the process. Moreover,

$$\bar{n} = \frac{1}{\exp \frac{\hbar\omega}{k_B T} - 1} \quad (4.1.2)$$

is the Bose-Einstein distribution. The chemical potential in the Bose-Einstein-distribution is zero since there is no particle conservation. It was assumed in the deduction of these equations that the electron-phonon coupling constant g describes a weak coupling and that \bar{n} is not much greater than unity [153, 155]. With this phenomenological approach, an approximately¹ exponential relation between energy-gap and PE rate is found which is valid for almost all triply ionized RE ions. Note that Eq. (4.1.1) also implies that multiphonon processes will be i) of lowest possible order and will ii) involve the maximum energy phonons available from the phonon spectrum to still conserve energy during the transition [100, 155]. This was found to be the

¹ In detail, the constants α and C both also depend on ΔE [153].

case for triply ionized RE embedded into glasses [155]. Representing EGLs for some glassy materials including the ones subject to the present work are shown in Fig. 4.2.

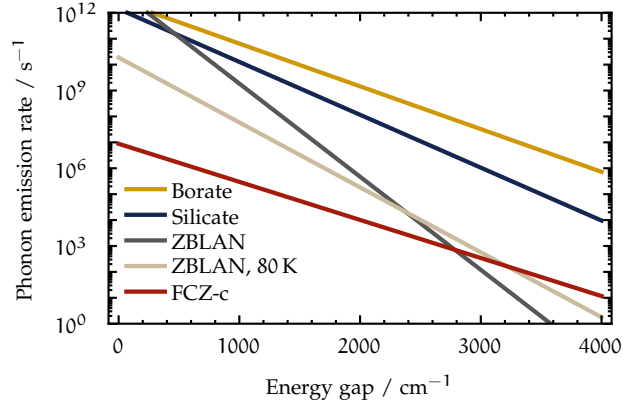


Figure 4.2: Comparison of energy-gap laws for different glassy matrices. References: ZBLAN [148, 149], ZBLA [151] at 80 K, FCZ-c (crystalline fraction) [152], borate [157], silicate [158].

Due to the large rates connected to it, PE will - with the few exceptions of metastable levels - be the dominating decay channel for excited states. This also constitutes the main technological avenue towards optimizing photoluminescence efficiencies, which is the choice of the host material where the maximum phonon frequency is one of the key parameters. For ZBLAN-based glasses it is $\hbar\omega_{\max} = 580 \text{ cm}^{-1}$ [51, 159] and for BaCl_2 , which constitutes the nanocrystals in the FCZ-c glass ceramics, it is $\hbar\omega_{\max} = 220 \text{ cm}^{-1}$ [12, 13].

The temperature-dependence of the PE probability has a general form

$$W_{\text{PE}}(T) = W_0(\bar{n} + 1)^p, \quad (4.1.3)$$

which results from the temperature dependence of the Bose-Einstein distribution. W_0 is the zero-temperature rate. Inserting Eq. (4.1.2) finally leads to

$$W_{\text{PE}}(T) = W_0 \left(\frac{\exp(\hbar\omega/k_B T)}{\exp(\hbar\omega/k_B T) - 1} \right)^p. \quad (4.1.4)$$

EXPERIMENTAL DETERMINATION OF PHONON EMISSION RATES Several complementary experimental methods exist to access PE rates over a specific energy gap. The three standard methods presented here all rely on photoluminescence. As this is not easy to measure in all cases, the preferred method depends on the particular transition involved.

The first method directly uses measured PL lifetimes and its relation to PE rates in Eq. (2.5.1): Via

$$W_{\text{PE}} = \tau^{-1} - A_{\text{SPE}}$$

the PE rate can be calculated from mono-exponential decays, whenever the Einstein coefficients for SPE are also known.

The second method is based on the build-up process of indirectly pumped PL signals [124]. The PE step between $|j\rangle$ and the adjacent $|j-1\rangle$ after a

pulsed excitation to $|j\rangle$ limits the time used for the build-up process of $|j-1\rangle$ population. The equations describing such a system are

$$\begin{aligned}\partial_t N_j(t) &= -W_{PE} N_j(t) \\ \partial_t N_{j-1}(t) &= -A_{j-1} N_{j-1}(t) + W_{PE} N_j(t),\end{aligned}$$

where the radiative decay rate $A_j \ll W_{PE}$ of the level $|j\rangle$ was neglected.² The point t_{\max} where the solution $N_{j-1}(t)$ becomes maximal is then found as

$$t_{\max} = \frac{\ln \frac{W_{PE}}{A_{j-1}}}{W_{PE} - A_{j-1}}.$$

It describes the time needed by the decay mechanism to overcome the build-up process and it can be easily determined from a measured decay whenever the build-up process is experimentally resolved.

The third method of PE rate determination is based on the temperature dependence of PE as expressed in Eq. (4.1.4). After recording the temperature-dependence of PL lifetimes τ from a particular transition, the resulting data is fitted with

$$\tau^{-1}(T) = W_{PE}(T) + A_{SPE},$$

similar to the first method.

The three methods were used complementary to construct effective EGL for the FCZ-c glass ceramics [6, 152]. There, the host-specific coefficients were determined to be $C = 1.4 \cdot 10^7 \text{ s}^{-1}$ and $\alpha = 3.8 \cdot 10^{-3} \text{ cm}$. For the untreated FCZ samples used here that include no nanocrystals, the FZ EGL from the literature [148–151] were in good agreement with the experimental decays compiled in this work. The EGL from Refs. [148, 149] with $C = 7.28 \cdot 10^{12} \text{ s}^{-1}$ and $\alpha = 8.28 \cdot 10^{-3} \text{ cm}$ was finally used³ as the simulations compared slightly better to the data than the other two.

RATE COEFFICIENTS With the transition probabilities for phonon emission $W_{PE,j} = W_{PE}(\Delta E_j)$ known from the EGL, the change of the population of level $|j\rangle$ by the gain through phonons from level $|j+1\rangle$ and losses through phonons to level $|j-1\rangle$, is accounted for with

$$\left. \partial_t N_j(t) \right|_{PE} = -W_{PE,j} N_j(t) + W_{PE,j+1} N_{j+1}(t)$$

in all rate equations ($j \geq 0$).

PHONON ABSORPTION The probability for the absorption of phonons (PA) can be calculated again from thermodynamic principles from the respective PE probability. The rates for phonon absorption W_{PA} and emission W_{PE} are related to the Bose-Einstein distribution in Eq. (4.1.2) with the equations (see Eq. (4.1.3))

$$W_{PA} = W_0 \bar{n}^P(T) \quad \text{and} \quad W_{PE} = W_0 (\bar{n}(T) + 1)^P,$$

² The initial conditions $N_{j-1}(0) = 0$ and $N_j(0) = P$ with P the pump rate were also omitted for brevity.

³ The value of α was converted with $\hbar \omega_{\max} = 580 \text{ cm}^{-1}$.

where W_0 is the so-called zero-temperature phonon rate [160]. Eliminating W_0 gives the relation

$$W_{PA} = e^{-\frac{\hbar\omega}{k_B T}} W_{PE} , \quad (4.1.5)$$

with the help of which the PA rates can be calculated from the PE rates that are known from the EGL. For $T \rightarrow 0$ the n approaches zero and hence $W_{PE} \rightarrow W_0$ and $W_{PA} \rightarrow 0$. For typical energy gaps $\Delta E = \hbar\omega$ of $\approx 1000 \text{ cm}^{-1}$, the absorption rate is about $\exp(-5) = 0.7\%$. From this it becomes clear that normally this effect is negligible. However, in the case of the metastable level for example, the population becomes large enough, and is stored long enough, so that phonon absorption to the levels $|5\rangle$, $|6\rangle$, and even $|7\rangle$ becomes significant, leading to Anti-Stokes emission from them. This emission would usually not exist as the non-radiative rates for such comparably small energy gaps are rather large compared to the radiative rates. See Fig. 4.9 for an example of such emission spectrum. This effect is also mentioned in Ref. [127] where these levels are found to be acting as a single multiplet comprised of rather widely spaced individual components.

In the rate equations, phonon absorption is henceforth accounted for via

$$\left. \partial_t N_j(t) \right|_{PA} = +W_{PA,j} N_{j-1}(t) - W_{PA,j+1} N_j(t)$$

for a level $|j\rangle$ with losses to the next higher level $|j+1\rangle$ and gains from the next lower level $|j-1\rangle$.

4.1.3 Ground state absorption

Ground state absorption in the case of pulsed excitation is considered as a population gain of the respective pump level N_{GSA} in the form

$$\left. \partial_t N_{GSA}(t) \right|_{GSA} = \rho_0 \sigma_{GSA} e^{-(t/\tau_0)^2} N_0(t) . \quad (4.1.6)$$

This means that a photon flux of $\rho_0 = I/(h\nu)$, where I is the optical intensity, excites with a probability equal to the absorption cross section σ_{GSA} of the respective pump level, ions from the ground state reservoir N_0 to the pump level population N_{GSA} . The time dependence of the pump pulse of duration τ_0 enters Eq. (4.1.6) via the exponential term. The optical intensity profile is treated as a Gaussian beam in simplified cylindrical coordinates,

$$I(r, z) = I_0 \exp\left(-\frac{2r^2}{w_0^2} - \alpha_0 z\right) . \quad (4.1.7)$$

r is the radial distance from the optical axis at the beam center along the propagation direction z . Fig. 4.3 shows the intensity profiles of the laser and the resulting emissions with representing parameters over the sample dimensions assuming the named symmetry.

The optical intensity is related to experimental parameters such as the laser power P and the Gaussian beam waist w_0 via

$$I_0 = \frac{2P}{\pi w_0^2} .$$

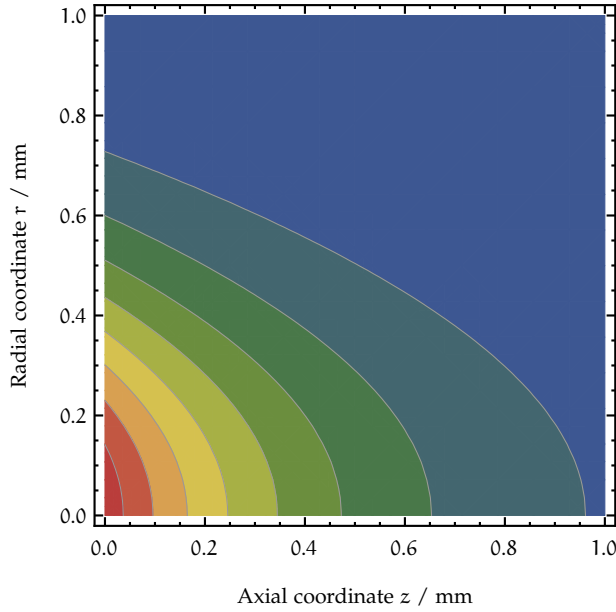


Figure 4.3: Contourplot of spatial pump rate profile from the excitation laser in cylindrical coordinates (r, z) . The profile has a radially Gaussian shape (along r -axis) and decreases along the axial (z -) direction according to the Lambert-Beer-Law (see Eq. (4.1.7)).

The Gaussian beam waist, denoted w_0 , is determined from beam profiles as shown in detail in appendix A.2.1. The average power is measured with a powermeter.⁴ For pulsed excitation the peak power P_0 is related to the directly measurable average power P_m with $P_0 = P_m / (f_{RR}\tau_0)$ involving the repetition rate f_{RR} and the pulse duration τ_0 . The pulse duration was measured with an SHG-based frequency-resolved optical gating (SHG-FROG), described in appendix A.2.2.

Note that in the following, the r - z -discretization of each of the population densities $N_j(r, z, t)$ resulting from Eq. (4.1.6) is implicitly presumed. Also it must be stressed here that the absorption coefficient α_0 is equal to $\sigma_{GSA}N_0(t=0)$ (cf. Eq. (2.4.4)) only in the pulsed pumping scenario. In the continuous pumping regime described later, excited state absorption adds to the ground state absorption to give an effective absorption coefficient that also depends on the pump power.

4.2 COMPARISON WITH EXPERIMENTAL PHOTOLUMINESCENCE DECAYS

The rate equation model described in the previous sections allows description of the Stokes part of the emission, that is, processes involving SPE and phonons. Strictly speaking there is also the possibility of Anti-Stokes emission with the help of phonons, described in detail in section 4.2.1.

In the following section, the solutions of the model will be compared to experimental decay measurements to test the correctness of the model para-

⁴ Thorlabs *PM100D* console with detector *S302C*

eters and the validity of the model picture. As spectroscopic decay measurements cannot discriminate between photons from different transitions at or near the same wavelength, it is necessary to adapt the simulation results to this situation. This problem is visualized in Fig. 4.4. There, the number of overlapping emissions per 5 nm interval around wavelength λ are counted. The number of overlaps over the whole λ range is between 0 and 6. Although not all contributions to an emission at k are equally strong, there is often significant perturbation of the primary emission. A good example are the overlapping emissions from the transitions $|10\rangle \rightarrow |1\rangle$ and $|9\rangle \rightarrow |0\rangle$ which are hardly resolved spectrally due to amorphous line broadening. Therefore, overlaps may not be disregarded when comparing to experimental decays.

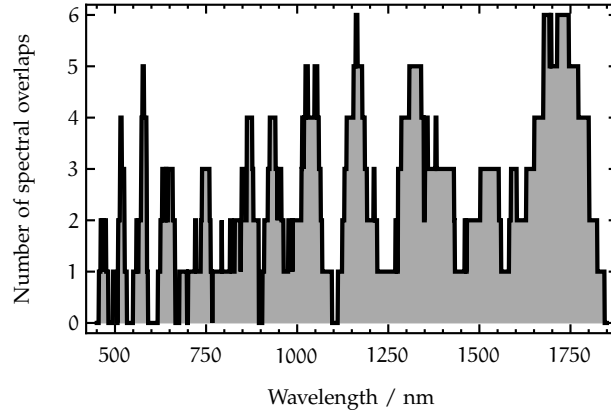


Figure 4.4: Number of spectral emission overlaps within the wavelength interval $|\lambda \pm 5 \text{ nm}|$.

The overlaps are considered by summing up the intensities per wavelength interval (i. e. $E_j - E_i \approx hc_0/\lambda$) after integrating over the sample dimensions to capture photons from each r - z -coordinate as it is the case with a light-collecting device such as a curved mirror in the experiment. The integration is carried out with

$$I_\lambda(t) = \sum_j \sum_{i < j} A_{\text{SPE},j} \beta_{ji} \iint N_j(r, z, t) 2\pi r dr dz, \quad (4.2.1)$$

where the sum compiles the terms

$$\forall i, j : |E_j - E_i| \approx \frac{hc_0}{\lambda}.$$

Here, $I_\lambda(t)$ is the decay function of light near wavelength λ . The sums collect light emitted near λ , defined by the branching ratios β_{ji} for all transitions from any levels $|j\rangle$ to lower lying levels $|i\rangle$. Since two transitions are overlapping whenever their *wavelengths* cannot be discriminated by the spectral monochromator, the threshold in the simulation is chosen in the *wavelength* space as opposed to the photon energy space.⁵

The experimental decays shown in the following were all recorded under experimental conditions excluding any unwanted effects not considered in the model. The intensity was kept very low (less than 10 mW average power).

⁵ The exact value is more or less determined by the slit width chosen during the experiments. Usually, $\Delta\lambda$ was 5 nm.

This helped to exclude effects related to the femtosecond pulses such as the simultaneous absorption of two photons (two-photon absorption, TPA) for which a nonzero overlap integral exists for several of the used excitation wavelengths. ESA at the pumping wavelength was precluded with the choice of the excitation wavelengths. Exclusion of a cumulative ESA with consecutive pulses entering an already pre-excited sample was achieved by lowering the repetition rate of the laser system. Frequencies of 100 Hz or less ensured that all neodymium ions are in the thermal steady-state prior to the occurrence of the next excitation pulse. Also, the decay measurements for the test of the Stokes processes were exclusively carried out with weakly doped samples so that no concentration quenching effects could affect the otherwise linear decays. In general, this means

$$\tau^{-1} = A_{\text{SPE}} + W_{\text{PE}} - W_{\text{PA}}$$

for the lifetime τ of every measured level.

4.2.1 Stokes emissions under the influence of glass phonons

Although featuring an already comparably low maximum phonon frequency of 580 cm^{-1} , glass decays are still subject to very strong multiphonon relaxation processes. These are able to very efficiently deplete any excitation brought to higher levels. Hence, most of the decays from higher lying emission lines in the visible spectral region had very low signal-to-noise ratios. Those could not be measured under the linear optical, pulsed pumping conditions chosen in this work to circumvent problems with nonlinear optical effects.

However, in the neodymium energy level scheme, the metastable level $|4\rangle$ features a strikingly large energy gap. Bridging this gap of around 5000 cm^{-1} by phonon emission requires almost 9 highest energy phonons of the glass matrix or more than 20 from the BaCl_2 nanocrystal. Therefore, this process is highly improbable and shows negligible rates of $<1 \text{ s}^{-1}$ in all samples. In the weakly doped samples this leads to very good emission intensities from there. Additionally, there is the unique possibility of being able to directly test the validity of the radiative decay rate. SPE is the only significant relaxation channel for population in the metastable level. As the rate for phonon absorption is non-zero but small compared to the radiative rate, this means

$$\tau^{-1} = A_{\text{SPE}} + W_{\text{PE}} - W_{\text{PA}} \approx A_{\text{SPE}}$$

for the lifetime. As the Einstein coefficients for SPE are of the order of 2000 s^{-1} , the decay is also very slow entailing the metastable status of that level.

In Fig. 4.5, this experimental situation is shown together with the result of the simulation. As shown in the small schematic on the right, the metastable level is resonantly pumped and its decay recorded over a long time scale. The decay is generally well approximated by the calculation.

An experimental case introducing processes involving phonons is shown in Fig. 4.6. There, the metastable level is non-resonantly pumped via $|5\rangle$ demanding a quick population of $|4\rangle$ by phonon emission. The energy gap between the levels $|4\rangle$ and $|5\rangle$ is comparably small being of the order of

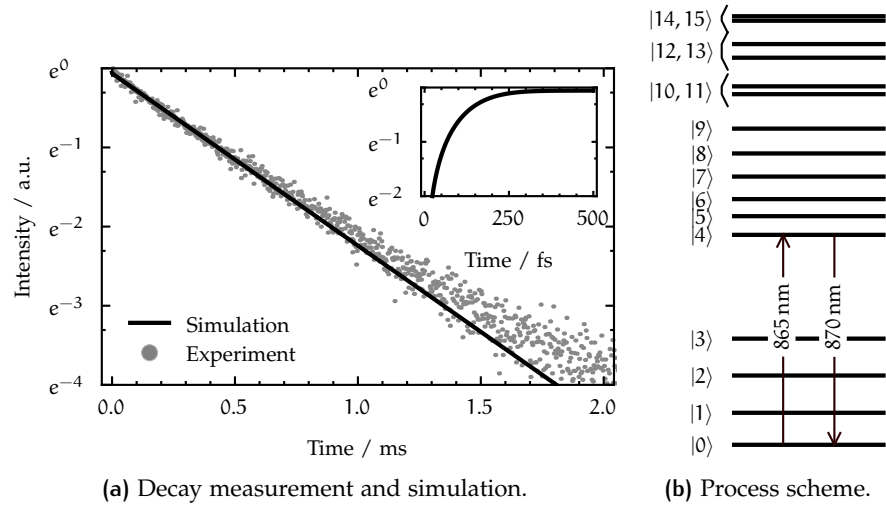


Figure 4.5: Emission from weakly doped FCZ1 glass sample recorded at 870 nm upon resonant pulsed excitation of $|4\rangle$. The solid line is the result of the simulation.

1000 cm^{-1} . After the quick phonon emission not resolved in the timescale of the figure, the decay of the metastable level is similar to the resonant pumping case. Since the phonon emission rate is also several orders of magnitude larger than the rate for spontaneous emission of $|4\rangle$, it also decays with the same total time constant.

A decay scheme including a cascade of multi-phonon emissions is shown in Fig. 4.7, where the neodymium is excited to a higher lying level but a low lying relaxation channel is observed. The efficiency of this radiative process is quite low in the glasses and therefore the signal-to-noise ratio is disadvantageous.

The small but measurable rate of phonon absorption is responsible for another interesting pumping scheme. Fig. 4.8 shows the situation where emission from level $|6\rangle$ at 750 nm is recorded under non-resonant pulsed excitation at 800 nm (in resonance to $|5\rangle \leftarrow |0\rangle$). Although unrelated to ETU or ESA, this process is also of the Anti-Stokes type. However, it stems from only power-independent coefficients as opposed to the major upconversion processes. From the emission spectrum in Fig. 4.9 it becomes clear that phonon absorption is the population mechanism as no higher frequency emission is there. The intensity ratios are also compatible to Eq. (4.1.5).

Taking level $|6\rangle$ independently gives a radiative decay rate of the order of 3000 s^{-1} from the JO theory. However, given the energy gap of around 900 cm^{-1} , the major decay mechanism would be phonon emission. However, from the decay measurement, a decay constant of 2200 s^{-1} can be determined, which is again the decay constant of the metastable level. In fact, population from the pumping level $|5\rangle$ reaches the emitting level $|6\rangle$ via phonon absorption until a quasi-stationary state is reached between the levels $|4\rangle$ to $|6\rangle$. Due to comparably quick population transfer in between them, their decay is solely limited due to the radiative decay of the metastable level as population stored there immediately comes to the other two. The three levels are thermally coupled making them the population reservoir from which further processes originate. The former was also observed

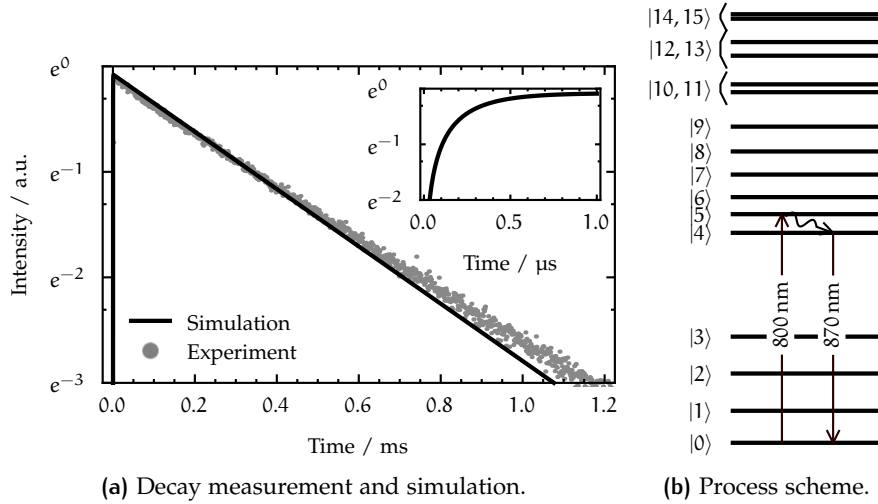


Figure 4.6: Emission from weakly doped FCZ1 glass sample recorded at 870 nm upon non-resonant pulsed excitation via $|5\rangle$. The solid line is the result of the simulation.

in the literature [127]. It is also the reason the decay constant of $|4\rangle$ is conveyed over to all of them.

4.2.2 Stokes emissions in the glass ceramics

Extending the model situation to the glass ceramics involves the transition from the glassy phonon rates to the ones in the effective medium. Also, the coefficients for SPE need to be replaced.

Fig. 4.10 shows a simulation of a decay that involves a pump step to a level, around 8000 cm^{-1} higher than the previously shown decays, which is followed by a multi-level phonon emission cascade to finally populate the emission level. This example is chosen to stress the EGL for the glass ceramic. At the beginning there is a short peak near $t = 0$. The remainder of the decay is the same as can be measured in the case of the glass. As the decay of the intermediate levels is dominated by phonon emission too, most of the overall decay is governed solely by the slow population drain in the metastable reservoir by the limited radiative emission from there.

As already mentioned and further elaborated in section 4.3, the glass samples do not efficiently emit radiation from higher lying levels rendering transitions that are in the visible spectral range inaccessible to time-resolved decay measurements. In the glass ceramic however, the radiative emission probabilities get drastically increased by the change of the phonon spectrum. Fig. 4.11 shows an emission stemming from a decay of a high lying level. Contributions to the total intensity at the recording wavelength $\lambda = 650\text{ nm}$ come not only from the resonantly pumped $|11\rangle$, but also from the next two, $|10\rangle$ and $|9\rangle$ that get populated by phonon emission from $|11\rangle$. The major intensity originates from the transitions $|10\rangle \rightarrow |2\rangle$, $|11\rangle \rightarrow |2\rangle$, and $|9\rangle \rightarrow |1\rangle$. The transitions from $|8\rangle$ to the ground state and $|12 + 13\rangle \rightarrow |3\rangle$ are also in this same spectral region but contribute only little. Level $|8\rangle$ is quickly depleted by MPR and at the same time has only a small Einstein coefficient.

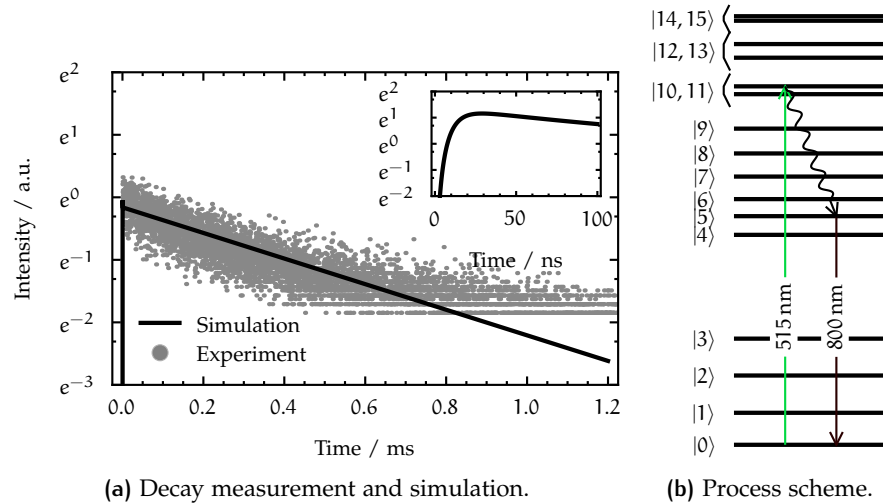


Figure 4.7: Emission from weakly doped FCZ1 glass sample recorded at 800 nm upon non-resonant pulsed excitation via $|11\rangle$. The solid line is the result of the simulation.

The levels $|12\rangle$ and $|13\rangle$ become not efficiently populated by phonon absorption from $|11\rangle$ although they would have had larger SPE-coefficients. In the figure there is a quicker decaying part that belongs to neodymium distributed over the glass matrix without nanocrystal influence. This intensity part has only little contribution to the total intensity integral that remains governed by the fraction of neodymium residing at the nanocrystal sites with their favorable phonon spectrum. The ultrafast resonant pumping is also conceivable from the spike near $t = 0$.

4.3 DISCUSSION

4.3.1 Influence of Einstein coefficients

The lifetimes of all but the metastable level are dominated by rapid (multi-)phonon emission. Whenever this is the case, the radiative decay channels described by the Einstein coefficients for spontaneous emission play only a minor role and so do inaccuracies in their coefficients earlier derived from JO theory. Hence, decay measurements of several transitions are mainly affected by the validity of the model parameters describing phonon emission, represented by the EGLs.

Nonetheless, in the case of the decays involving the metastable level and also the levels thermally coupled to it, radiative decay is the major state depletion mechanism. In experimental decay measurements of transitions directly involving these levels or in measurements, where emissions from these levels are overlapping the main decay process, inaccuracies in the Einstein coefficients directly affect the quality of the rate equation simulations. Such deviations are visible from the figures 4.5 to 4.8. There, the overall decay behavior is well-described, but differences in the late decay are obvious.

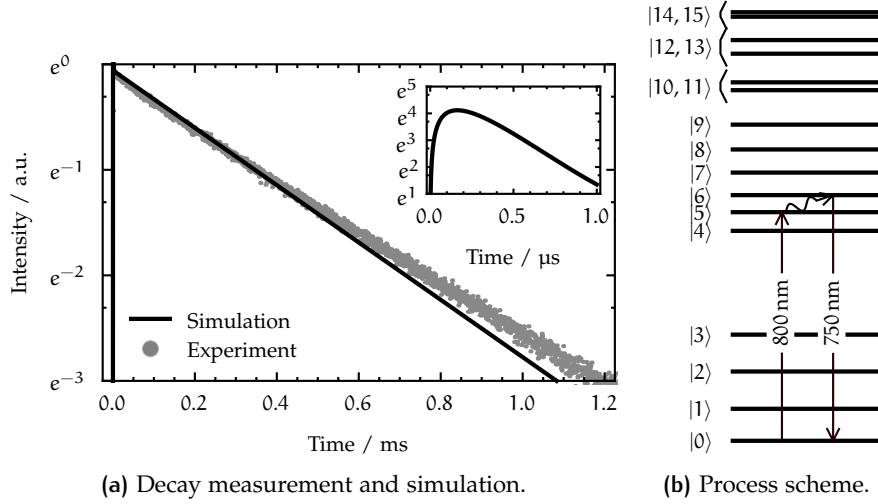


Figure 4.8: Emission from weakly doped FCZ1 glass sample recorded at 750 nm upon non-resonant pulsed excitation via $|5\rangle$. The solid line is the result of the simulation.

However, even though these slight deviations of the order of less than 10% do exist, their influence on the remaining part of the rate equation description is not dramatic. Recalling the main goal of this work to be a description of the upconversion emission under continuous broadband excitation, it becomes obvious why the JO-inherited accuracy level of 10% in the radiative decay rates will pose no major problem. From Eq. (2.5.2) the relation $I_{\text{PL}} \propto \tau$ is known, which shows that errors in the lifetime linearly affect the cw simulation results. The pump-rate (besides thermal population) determines the order of the level populations. Solving Eq. (4.1.6) independent from its coupling to the other level's populations, gives an estimate of the order of magnitude of the population numbers and hence, emission intensity, because of

$$I_{\text{PL}} \propto A_{\text{SPE}} N_{\text{PL}}.$$

Exploiting $\lim_{t \rightarrow \infty} \text{erf } t/\tau_0 = 1$ in the solution

$$N_{\text{GSA}}(t) = \frac{\sqrt{\pi}}{2} N_0 \tau_0 \rho_0 \sigma_{\text{GSA}} \text{erf } \frac{t}{\tau_0},$$

and inserting typical values such as $\tau_0 = 100$ fs, $\sigma_{\text{GSA}} = 1$ pm², $\nu = 500$ THz, $P = 10$ mW, $f_{\text{RR}} = 1$ kHz, $w_0 = 100$ μm, and rounding Planck's constant h to 10^{-33} J s, yields an approximate value of $N_0/1000$ for a typical population number density. N_0 is of the order of 10^{21} cm⁻³. From this simple estimation, it is clear that the numbers simulated with the rate equation model are rather large and deviations of the order of several percent are probably irrelevant as soon as the order of magnitude is matched.

Note that the simulation of the decays shown in the previous section did not involve any fitting procedure of any kind and no free parameters. It would therefore be a legitimate venue for further steps of the rate equation analysis to adjust the parameters in the same stepwise, cross-checking-experiments fashion, as traversed with the model development. However, free parameters or parameter adjustment was avoided in this work for the present since

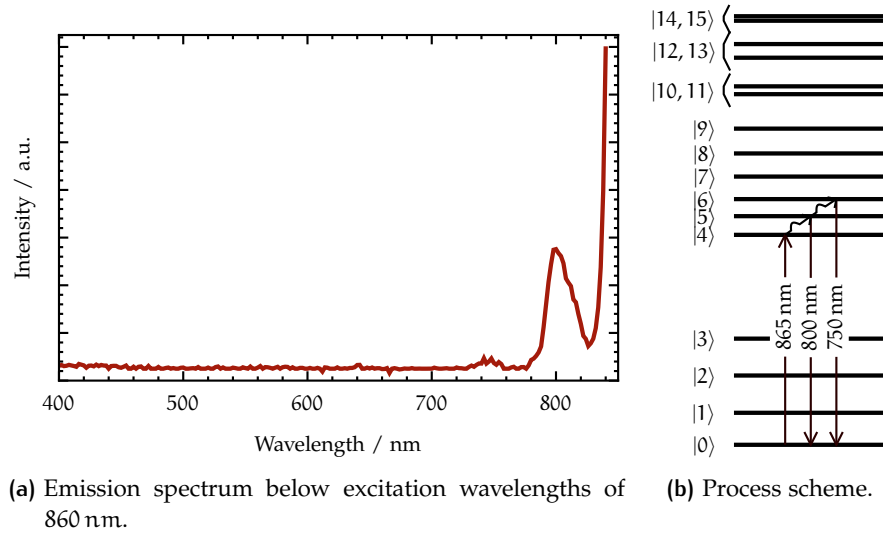


Figure 4.9: Anti-Stokes emission spectrum from weakly doped FCZ1-c glass ceramic sample upon pulsed excitation in resonance to $|4\rangle \leftarrow |0\rangle$ with 10 mW. Thermal occupation of $|5\rangle$ to $|6\rangle$ generated by phonon absorption from $|4\rangle$ leads to emission at wavelengths shorter than the pump wavelength of 865 nm. Note that this is not an upconversion process in the sense of the discussion in chapter 5.

as few instabilities as possible should be introduced to the numerical solver procedure.

Summing up, the radiative decay coefficients derived from JO theory and verified by further complementary approaches shown in chapter 3 are sufficiently well-determined for the purpose of this model. Although larger inaccuracies are not present, they do not affect the emission intensity and have thus no significant impact on the following analysis.

4.3.2 Nanocrystal influence on Stokes emissions

In section 2.4.2 it was found that growing nanocrystals within the FCZ glass matrix lead to emphasized emissions, enables emission of quenched levels at all, and increases lifetimes of emitting levels. With the rate equation model established to successfully describe regular, Stokes-type photoluminescence, it is now possible to quantitatively evaluate the influence of the nanocrystal growth on the neodymium emission characteristics. A suitable magnitude for this is the radiative quantum efficiency, defined as

$$\eta = \frac{A_{\text{SPE}}}{A_{\text{SPE}} + W_{\text{PE}}} . \quad (4.3.1)$$

Considering the weight of the radiative decay channel with respect to the remaining decay channels – governed by phonon emission for low neodymium concentrations –, the quantum efficiency η gives the number of emitted photons per excited ion [140].

The radiative quantum efficiencies of neodymium levels in FCZ and FCZ-c are given in Table 4.1. Considerable emission can be presumed whenever the radiative decay rates are no less than about two orders of magnitude

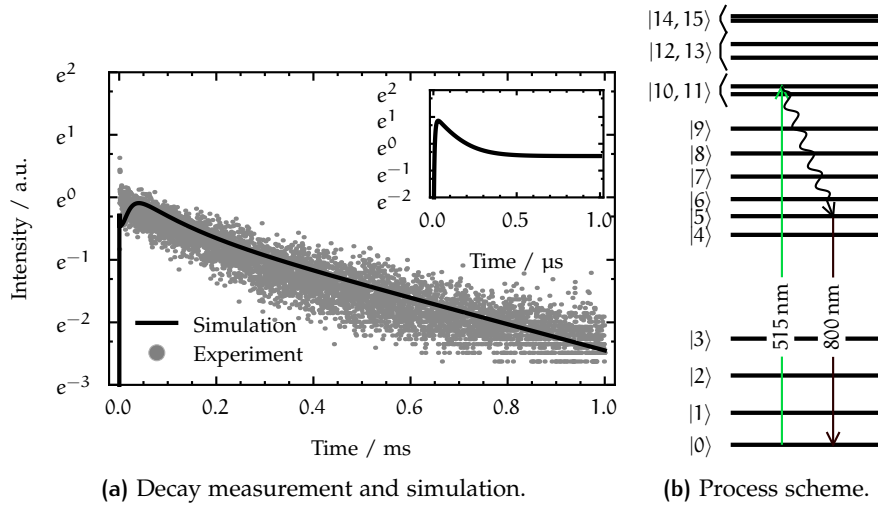


Figure 4.10: 800 nm emission from weakly doped FCZ1-c glass ceramic sample upon pulsed excitation at 515 nm in resonance to $|11\rangle \leftarrow |0\rangle$ and subsequent multi-level phonon emission cascade responsible for the population of the emission level. The solid line is the result of the simulation.

smaller than the phonon emission losses [9], corresponding to $\eta \geq 1\%$. In the case of the glass samples, this strict criterion assigns significance only to the emission from the metastable level in consistence to the experimental findings in section 2.4.2. In fact, the levels thermally coupled to it (namely |5) and |6)) also receive considerable population and emit at least measurable amounts of light. This thermal coupling is however not considered in the simple form of the definition of η in Eq. (4.3.1) and will hence be disregarded here.

In the case of the glass ceramic, the situation changes significantly. Upon nanocrystal growth, the probabilities for losses to phonon emission get decreased enough to allow for significant emission even from otherwise quenched levels. The most obvious changes are seen with the levels |14), |10), and |9), in fair agreement to Fig. 2.9a, where a drastic improvement of their emissions at 535, 575, 590, 650 and 665 nm is found.

The two properties common to these levels that are responsible for the emission increase are

- (a) radiative transition rates (see Table 3.6) of more than 10^3 s^{-1} and
- (b) energy gaps large enough to require more than 5 maximum energy phonons for an energy-conserving multi-phonon transition ($p \geq 5$).

In addition to the levels mentioned above, these criteria are also met for the metastable level |4), but also for |7), |12), and |13). Emission from the latter three are weaker than and also overlapping the emissions at the above named wavelengths and are usually not individually resolved in neither the glasses nor the glass ceramics.

The case of the metastable level |4) with a radiative quantum efficiency equalling unity regardless of the host material is special, as its energy gap equals either 9 or more than 20 maximum-energy phonons. This fosters the arguments used in section 2.5.1 to assign the emission increase mechanism solely to the change of the phonon spectra in the host upon the transition

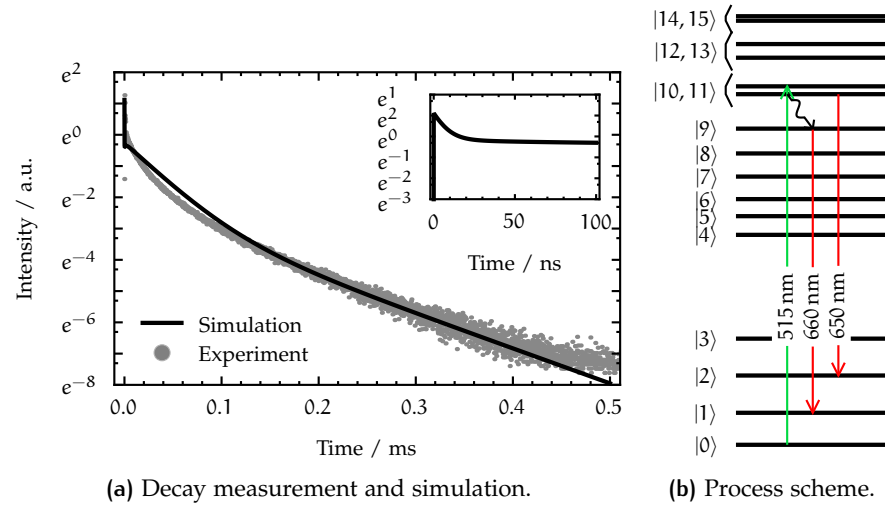


Figure 4.11: 650 nm emission from weakly doped FCZ1-c glass ceramic sample upon resonant pulsed excitation at 515 nm to level $|11\rangle$. The main contributions to the decay at that wavelength come from the transitions starting at $|11\rangle$ and $|10\rangle$ ending in $|2\rangle$ and the transition from $|9\rangle$ to $|1\rangle$. The solid line is the result of the simulation.

from glass to glass ceramic. For the levels named above with energy gaps and radiative rates set just so as to be sensitive to the host change, the emission differs drastically. For the metastable level and the levels coupled to it, phonon emission is no decay channel at all even in the glass. Starting from there, the further decrease of phonon emission probability does not change the situation any further and the emissions stay approximately constant over the annealing steps responsible for the nanocrystal growth. This also means that the photoluminescence lifetimes do not depend on the experimental temperature.

The levels $|1\rangle$ to $|3\rangle$ and $|7\rangle$, for example, do not show large quantum efficiencies despite their energy gaps correspond to at least five phonons (criterion (b) met), since the radiative decay rates are too low (criterion (a) not met). Therefore, no emission from them is seen in the experimental spectra.

In essence, a significant influence of the nanocrystals on the emission during the transition from glass to glass ceramic are expected, whenever the radiative decay rates are already considerable (criterion (a)) and the number of maximum-energy phonons needed simultaneously for a multi-phonon emission, changes from less to more than five with the transition.

4.3.3 Evaluation of effective-medium model

The rate-equation model developed in this work to describe neodymium dynamics in glass ceramics is based on an effective-medium combination of fractions of neodymium in glass and in the nanocrystalline part. No special interaction mechanisms are considered between neodymium in either submatrix other than the ion-ion interactions introduced later in chapter 5. However, even there, no discrimination between the two with respect to energy exchange is made.

Table 4.1: Radiative quantum efficiency η in FCZ and FCZ-c. $p = \Delta E/(\hbar\omega_{\max})$ gives the approximate number of maximum-energy phonons that need to be emitted simultaneously for an MPR transition of the respective level. The last column indicates whether significant emission of the particular level can be presumed. In the case of FCZ, only the metastable level shows significant emission.

$ i\rangle$	$\eta_{\text{FCZ}}/\%$	p_{FCZ}	$\eta_{\text{FCZ-c}}/\%$	$p_{\text{FCZ-c}}$	$\eta_{\text{FCZ-c}} \geq 1\%$
$ 1\rangle$	0.0	3	0.0	9	
$ 2\rangle$	0.0	3	0.3	9	
$ 3\rangle$	0.0	3	0.3	9	
$ 4\rangle$	100.0	9	100.0	25	yes
$ 5\rangle$	0.0	2	0.7	5	
$ 6\rangle$	0.0	2	0.8	4	
$ 7\rangle$	0.0	2	1.5	5	yes
$ 8\rangle$	0.0	2	0.1	5	
$ 9\rangle$	0.0	2	10.5	6	yes
$ 10\rangle$	0.0	3	5.9	8	yes
$ 11\rangle$	0.0	1	0.3	2	
$ 12\rangle$	0.0	2	1.9	7	yes
$ 13\rangle$	0.0	1	1.1	2	yes
$ 14\rangle$	0.0	3	12.6	7	yes
$ 15\rangle$	0.0	1	0.2	3	

The two neodymium fractions were combined by a weighted summation involving a constant weighting parameter δ . For the glass ceramics, two rate equation systems are solved and the intensities $I_{\text{PL}} \propto A_{\lambda} N_j$ are linearly combined with the parameter δ to give the total decay contributions by neodymium from both fractions. Although δ appears to be a free parameter, certain limits are imposed to it. First, as is evident from the experimental results, δ must be larger than zero, otherwise no nanocrystal influence could be observed. Secondly, the amount of neodymium in the nanocrystals should be limited by the volume fraction of the nanocrystals, if the neodymium remains homogeneously distributed. The latter constitutes merely an assumption, since growing nanocrystals could lead to clustering of neodymium ions. However, such clustering – equivalent to a local concentration increase – would lead to increased probabilities for ion-ion interactions. Although this is covered in detail in chapter 5, it can already be foreclosed here that no systematic increase of ion-ion interaction rates, exceeding the rates expected for homogeneously distributed neodymium, are found. It might of course still be the case for a small fraction of neodymium, but it appears from the power-dependent decay measurements that the concentration-quenched neodymium decays obey the regular decay laws found for homogeneously distributed neodymium and that there is no indication of strong clustering. The choice of the parameter δ was found to be optimal right in the middle of the aforementioned $0 < \delta < 20\%$ interval with $\delta = 10\%$. Deviations here also have no huge impact on the intensity simulations as the nanocrystal neodymium contributions associated to δ are usually much larger than the $(1 - \delta)$ contributions from the glassy neodymium. They contribute to for example the quick part in the PL buildups.

The radiative and phonon-related parameters of the glass model stem from the JO analysis and the literature EGL. In the case of the glass ceramic,

own JO parameters and radiative rates were deduced for the whole matrix. Regarding the phonon rates, two parameter sets are involved. The neodymium fraction in the glassy part of the glass ceramic obeys the glass EGL, while the nanocrystal-included neodymium fraction is subject to another EGL ascribed to these nanocrystals. While the situation is instructive for the glass samples, where glass-parameters can be directly used, in the case of the glass ceramics, it is more complex. It would appear that with the FCZ-c EGL from Ref. [152], an EGL deduced from the whole glass ceramic is applied to the part of neodymium constrained to the nanocrystals. However, it is in fact the case that the measurements leading to the FCZ-c EGL are based on only the very late decays or slow buildups of neodymium levels which are also subject to a change regarding their lifetimes upon nanocrystal growth. As the nanocrystals lead to prolonged lifetimes, they also dominate all late decays and slow buildups whenever there is actually a nanocrystal effect. This means that the EGL deduced in this way are really only based on decays of neodymium in the nanocrystal influence. Therefore, the parameter combination of whole-sample JO rates with mixed EGLs is actually perfectly valid to describe the glass ceramics.

The combination of glass and nanocrystal neodymium decays ensures also that the early parts of a decay simulation where quick buildup processes from glassy neodymium might precede the slower, finally dominating buildup process of nanocrystal neodymium, are correctly described. Of course, an exact simulation of such decays with such a simple model is not expected. However, the aim of describing the major *intensity* contributions is fulfilled decently. Quick buildup processes are not only imperfectly simulated due to model simplifications, but also due to the (partly intentional) experimental insufficiencies. Low excitation powers and loose focusing ensured the absence of nonlinear effects, such as saturation, multi-photon excitation, higher-harmonics generation and the like. The low signal-to-noise ratios accompanied by weak excitation in connection with limited recording time of photoluminescence decays lead to lower experimental resolution in the intensity direction (ordinate) than in the time direction (abscissa).

4.3.4 Coefficients for phonon emission and absorption

EGL SIMPLIFICATIONS Generally, PE probability coefficients from the EGL are not expected to have very high accuracies due to the strictness of the mono-exponential EGL model. For example, not only the highest-energy phonons might be participating in a transition [124], for example when the energy gaps not exactly match an integral number of phonons. This might also be true when phonons of less than maximal energy are more strongly coupled to the electrons of the RE ion. Impurities, ion clustering and further imperfections in the model system lead to competing, quick population drains that apparently contradict to the expectations from the EGL. In these cases, the EGL provide an insufficient description of the situation and only an approximation of the decay rate can be calculated from them. Furthermore, the energy-gaps these coefficients are based on are not very precisely defined, especially in glasses. Here, the strong inhomogeneous line broadening results in a distribution of energy gaps, well depending on the individual ion environment. In EGL, such distributions are disregarded and only their central moment is considered. Manual adjustment of the EGL

parameters C , α , or even the energy gaps ΔE_j ; theoretically enables for arbitrary decay simulations.

In this work, some of the decay measurements are not perfectly simulated, and in particular the quick part of buildup processes lacks in this respect, possibly due to the ultrashort pumping involved [161]. The importance was however attached to the fair description of general trends and the intensity-determining contributions. In order to be able to canonically describe the complex material system with as few free or adjustable parameters as possible, the strict assumptions of the EGL were maintained. In some cases, systematic deviations between model and measured decays could be found. The distributed character of the energy-gaps needed to be accounted for, whenever exceptional line broadening rendered the rigorous treatment with peak-to-peak-determined energy-gaps impossible. Slight corrections using the centre-of-mass peak positions instead, or consideration of levels as spectral intervals, lead to better results. In Refs. [149, 162, 163] the same was accomplished by adapting the EGL towards smaller energy gaps. In general however, the parameters were used as initially determined. In particular, no fitting of the model to the data was used to adjust parameters automatically in any way. The verification of the parameter set was instead achieved by the step-by-step establishment of the parameter set in a self-consistent fashion.

SELECTION RULES Further systematic deviations from perfect EGL is found whenever transitions are further restrained by selection rules. In neodymium, this is the case for the transitions $|17\rangle \rightarrow |16\rangle$, $|16\rangle \rightarrow |15\rangle$, and $|4\rangle \rightarrow |3\rangle$. The levels associated with the former two transitions are not included to the present work. The latter transition however, is part of the model description. The triangle-rule [155] holds,

$$|J - J'| \leq r \leq |J + J'| ,$$

with $r \leq 6$ for electronic operators of rank r in the case of lanthanides. Since there is no change in parity for intra-4f transitions, only even-order terms are present in the ion-lattice-interaction expansion. In the case of $|4\rangle \rightarrow |3\rangle$, there is $6 \leq r \leq 9$. In addition, $|\Delta J| \leq 2l$ holds, which, with $l = 3$ for RE ions, implies that $r = 8$ [155]. It is therefore defined only by an even-order term of the ion-lattice interaction for MPR. Unless the radiative rates are not exceptionally large, this selection-rules slows down phonon emission by a factor of two to three [124]. In real hosts, this selection rule is relaxed by J-mixing [164]. Moreover, as phonon emission is way less significant than radiative decay, such slow-down effect will probably go unnoticed.

4.4 SUMMARY

In summary, a rate equation model for the description of Stokes-type photoluminescence upon pulsed excitation is developed. Taking the radiative parameters from chapter 3 and EGLs from the literature, the (possibly spectrally overlapping) decays in glass were directly simulated and the related coefficients tested with decay measurements. For the decays measured with glass ceramics, an effective-medium rate equation model was employed based on a combination of glassy neodymium and neodymium

under nanocrystal influence. The combination successfully described several decay measurements verifying the used parameter sets in a step-by-step, self-consistent fashion, extending the system with another new process per step. Until here, more than 150 independent parameters⁶ are used for the glass description and roughly twice that for the glass ceramic.

The influence of the possible uncertainty of JO-derived radiative decay rates are found to be insignificant with respect to possible errors from the EGL. However, most decays were found to be simulated fairly well.

A criterion was established, which describes, whether a drastic lifetime increase is expected for a particular transition upon nanocrystal growth, i.e., upon transition from precursor glass to glass ceramic. The criterion essentially consists of the two requirements of (a) sufficiently large radiative decay rates with roughly $A_{\text{SPE}} > 10^3 \text{ s}^{-1}$ and (b) energy gaps equalling $p = \Delta E / (\hbar\omega_{\text{max}}) < 5$ maximum-energy phonons in the glass and $p \geq 5$ in the glass ceramic.

Several levels fulfill this criterion and the radiative quantum efficiencies η , defined as the number of photons emitted per excited ion, increase significantly from about zero in the glass to a few percent in the glass ceramic. This observation is in very good agreement to the observations made in the experimental photoluminescence spectra in Fig. 2.9a.

The rate equation tool so far describes Stokes-type photoluminescence decays of weakly doped neodymium in glasses and glass ceramics. Ion-ion interactions and power-dependent effects as responsible for upconversion will be included in the next chapter focusing on the Anti-Stokes processes. There, the time-dependence will be disregarded in favor of the simulation of upconversion photoluminescence spectra upon continuous, monochromatic excitation.

⁶ Most of them, $\binom{15+1}{2} = 120$, are for SPE, i.e. for transitions between 15 excited states and the ground state. PE and PA amount for $2(15) = 30$ transitions between these.

5

RATE EQUATION MODEL - ANTI-STOKES PROCESSES

In the previous chapter the rate equation model was set up to describe the basic pump and de-excitation mechanism responsible for Stokes-type photoluminescence (PL). All effects included into the model so far are linear in the excitation power and do not describe the optical upconversion of infrared pump light. In this chapter, further population mechanisms will be described that constitute the upconversion process. These are the absorption by excited states, the direct energy transfer between two ions, and cross relaxation, the primary quenching mechanism for neodymium [146, 147].

5.1 MODELLING ANTI-STOKES EMISSIONS

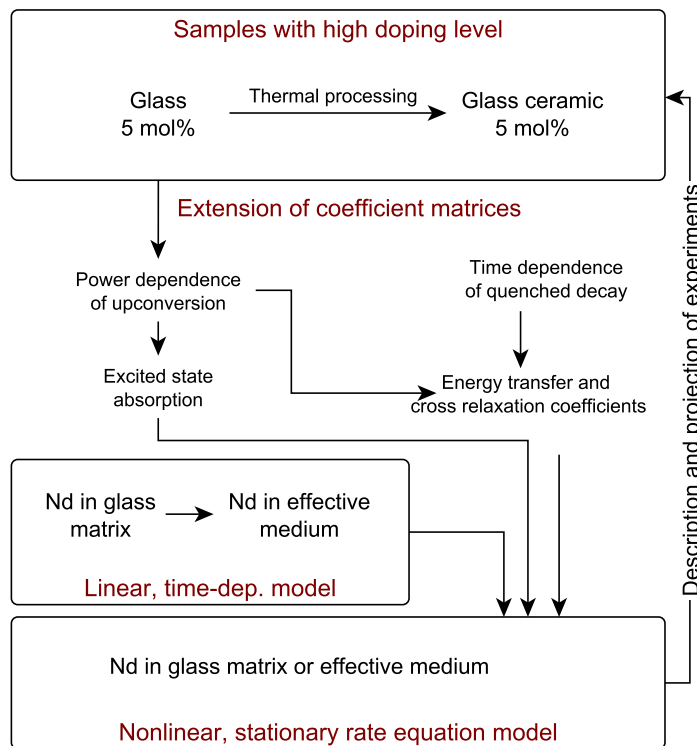


Figure 5.1: Schematic of stationary rate equation analysis, extension to Anti-Stokes effects.

As denoted in Fig. 5.1, the model parameters from the previous chapter are kept fixed during this extension. Again, the description for the glass and the glass ceramic are set up in parallel. Moreover, as weak doping levels do not lead to strong upconversion, the experiments are performed on the highly doped samples. The main test experiment series aiming at

the verification of the simulation results is the measurement of the power-dependence of upconversion emission. Since the experiments are therefore carried out under continuous laser irradiation, the simulation was adjusted to calculate the stationary solutions to the problem.

5.1.1 Excited-state absorption

Excited-state absorption (ESA) can be modeled in analogy to GSA, described earlier in section 4.1.3. A spectrally extended pump radiation can be resonant to more than one ESA transition. For the description of upconversion of continuous laser irradiation at 800 nm however, there was only a single non-zero overlap for the transition between level $|4\rangle$ and $|15\rangle$, which is shown in Fig. 5.2. There, the emission line shape of $|4\rangle$ (fawn) is convoluted with the line shape of the laser source (red). The result (brown) is plotted in addition to the nearby absorption, namely of level $|14 + 15\rangle$ (yellow).

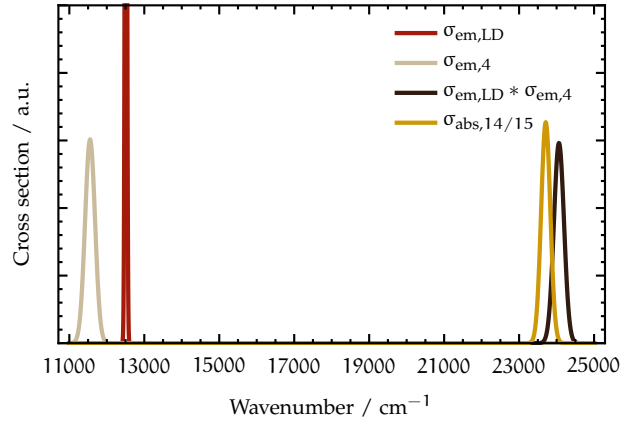


Figure 5.2: Overlap for ESA at pumping wavelength of 800 nm for FCZ-c. The laser diode $\sigma_{em,LD}$ (plot range clipped) is convoluted with $\sigma_{em,4}$. The overlap integral between the result and the $\sigma_{abs,14/15}$ absorption lines is calculated. Note that although the overlap for ESA is non-zero, it is still not in perfect resonance.

The corresponding contribution to the respective population densities is written similar to the GSA case as

$$\left. \partial_t N_{i/j}(t) \right|_{ESA} = \pm \rho_0 \xi \sigma_{ESA} N_4(t).$$

In addition to the otherwise identical GSA formulation from Eq. (4.1.6), the factor $\xi < 1$ specifies how well the pump is overlapping the ESA as compared to the GSA transition and is used as a weight to ensure energy conservation.

For the evaluation of overlap integrals between the excitation laser emission spectrum and an ESA transition, the two spectra have to be present. However, while the laser spectrum is readily measurable, the ESA spectrum is not, although there are numerous attempts involving experimental and semi-theoretical methods [161, 165–167]. Here, a simple method is used to estimate the overlap integrals. The regular GSA overlap integral between

the laser emission spectrum σ_{em} and the relevant part of the absorption spectrum, σ_{abs} , is calculated from [45]

$$\kappa_{\text{GSA}} = \int \sigma_{\text{em}}(E) \sigma_{\text{abs}}(E) dE, \quad (5.1.1)$$

where $E = \hbar\omega$. To determine the ESA overlap, the line shape of the excitation laser at energy E_1 is shifted to $E_3 = E_1 + E_2$ by the convolution with the emission spectrum of $|4\rangle$ centred at position E_2 , like

$$\kappa_{\text{ESA}} = \int \sigma_{\text{em}}(E) \sigma_{|15\rangle \leftarrow |4\rangle}(E) dE \approx \int \left(\sigma_{\text{em}}(E) * \sigma_{|4\rangle \rightarrow |0\rangle}(E) \right) \sigma_{|15\rangle \leftarrow |0\rangle} dE.$$

The relative fractions of GSA, $1 - \xi$, and ESA, ξ , were then found by calculating the ratio between κ_{GSA} or κ_{ESA} and $\kappa_{\text{GSA}} + \kappa_{\text{ESA}}$, respectively. This procedure yielded a ξ of 2% for the glass and 11% for the glass ceramic. Such higher value for the latter is indeed expected since the line shape changes towards broader widths due to the electric field split introduced by nanocrystal's static electric field. In addition, the peak position is also slightly shifted as denoted earlier in section 3.4.1.

As already mentioned, whenever ESA is considered, the GSA term in section 4.1.3 needs to be modified since the pump radiation is attenuated stronger in z -direction similar to the case of pure GSA and hence, α_0 increases by the above terms. The ESA cross section σ_{ESA} was estimated with

$$\sigma_{\text{ESA}} = A_{\text{SPE},j} \beta_{ji} \frac{\lambda^2}{8\pi n^2} g(\nu_0) \quad \forall i, j : |E_i - E_j| = hc/\lambda, \quad (5.1.2)$$

where $g(\nu_0)$ denotes the lineshape function at the pump frequency ν_0 and $j = 15$ and $i = 4$ are the participating levels. The refractive index n is the one for glass or the effective refractive index from the glass ceramic. The formula gives estimations for the ESA cross sections of 0.016 pm^2 and 0.018 pm^2 for the glass and the glass-ceramic samples, respectively. Both numbers are comparably low, which might be caused by the fact that $|4\rangle \rightarrow |15\rangle$ is spin-forbidden [168].¹

A comparison to literature data gives good agreements [167]. Generally it is reported that ESA at the resonant GSA wavelengths is rather weak and about 2 orders of magnitude less probable than GSA [49]. This observation, which is fostered by the values found here, is somehow surprising given the large number of nearby states in the neodymium level scheme [49]. Although other references give different ESA values [109, 168], these have in common that quite different host materials or very vague theoretical methods were taken as a basis. As the overlaps depend remarkably on the line widths that vary strongly in different hosts, they might differ by as much as 1 order of magnitude between crystals and glasses [98]. Moreover, different wavelengths were specified for the ESA cross sections. This is a special problem since $\sigma_{\text{ESA}}(\lambda)$ fluctuates notably in the range between 795 nm and 805 nm. Nonetheless, these problems were solved in this work with the above-mentioned overlap factor ξ .

¹ $|4\rangle \rightarrow |15\rangle$ denotes $|^4F_{3/2}\rangle \rightarrow |^2D_{5/2}\rangle$, where $\Delta S = |S - S'| = |3/2 - 1/2| = 1$ violates the selection rule $\Delta S = 0$, mentioned in section 2.1.

5.1.2 Ion-ion interactions

SPECTRAL OVERLAP Given sufficient adjacency between two neodymium ions, several ion-ion interactions are possible. Two main process classes are distinguished, namely energy transfer upconversion (ETU) and the down-converting cross-relaxation (CR). For them to be efficient, spectral overlap must be present for the de-excitation step in one of the ions and the spectrally corresponding excitation step in the other ion. Due to the function as population reservoir, all significant ion-ion interactions in neodymium originate from level $|4\rangle$. To find out which processes are in resonance at all and what their respective significance is, the overlap integrals from Eq. (5.1.1) between all transitions were calculated. $\sigma_{\text{em}}(k)$ and $\sigma_{\text{abs}}(k)$ in this case, are the emission and absorption cross sections of donor and acceptor of the excitation energy, respectively. The working principle is indicated in Fig. 5.3. Here, in contrast to the ESA-overlap integral, the convolution of the donor level emission and the lineshape of $|4\rangle$ is superimposed to the several absorption bands near their sum energy. Then the overlaps with each of those absorption bands are calculated. Whenever there is a non-vanishing overlap integral, this process is considered in the model.

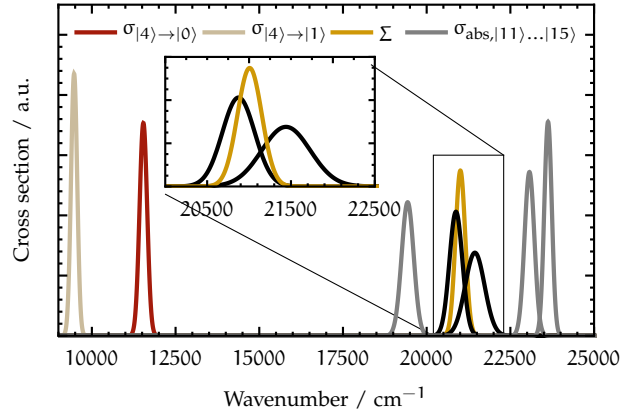


Figure 5.3: Overlap for ETU (ETU_3) in FCZ-c. The line shape of the transition $|4\rangle \rightarrow |1\rangle$ (fawn) is convoluted with the line shape of level $|4\rangle \leftarrow |0\rangle$ (red) and the result (yellow), abbreviated Σ , is shown together with absorption lines with either non-zero overlap (levels $|12\rangle$ and $|13\rangle$, black) or zero overlap (gray).

CONCENTRATION QUENCHING Fig. 5.4 shows a comparison between the decay corresponding to the well-known neodymium laser process in a weakly and a stronger doped sample (FCZ1 and FCZ5, respectively). Upon 800 nm pulsed excitation, the population leaves the state $|4\rangle$ in FCZ5 earlier as in an exclusively radiative decay $|4\rangle \rightarrow |1\rangle$ since ETU and CR also deplete the metastable state $|4\rangle$. For its lifetime it follows in a generalised form ($W_{\text{PE}} \approx 0$)

$$\tau_4^{-1} \sim A_{\text{SPE}} + w_{\text{CR}}N_0 + w_{\text{ETU}}N_4, \quad (5.1.3)$$

where the rate associated to $w_{\text{ETU}} = \sum_j w_{\text{ETU},j}$ involves the concentration N_4 of the excitation and therefore implicitly depends on the pump power. The concentration dependent lifetime shortening described with Eq. (5.1.3) is called concentration quenching, as the CR and ETU coefficients are de-

terminated by the distance between two RE ions and hence, on the RE concentration.

ENERGY TRANSFER In this work individual rate constants w_{ETU} and w_{CR} for neodymium in ZBLAN were used, which were derived from the literature [169]. There, relations for the concentration dependence of either are given. The data from Ref. [169] was linearly fit to give the concentration dependence of the net ETU parameter,

$$w_{\text{ETU}}(N_0) = -6.62 \cdot 10^{-24} \text{ m}^3 \text{ s}^{-1} + 2.70 \cdot 10^{-49} \text{ m}^6 \text{ s}^{-1} \times N_0 .$$

This net value equals the sum of all individual ETU rates originating from $|4\rangle$. It was distributed over the individual rates with quantitative weights determined from the normalized spectral overlap integrals as an estimation. The resulting individual ETU coefficients are listed in Table 5.1.

Table 5.1: ETU processes and corresponding rate constants.

Symbol	Process $2 \cdot 4\rangle \rightarrow$	k/cm^{-1}	$w_{\text{ETU}} / (10^{-24} \text{ m}^3 \text{ s}^{-1})$	
			FCZ5	FCZ5-c
ETU ₁	$ 3\rangle + 9\rangle$	5600	39.2	40.5
ETU _{2a}	$ 2\rangle + 10\rangle$	7500	53.2	48.5
ETU _{2b}	$ 2\rangle + 11\rangle$	7700	15.1	18.1
ETU _{3a}	$ 1\rangle + 12\rangle$	9900	46.1	44.4
ETU _{3b}	$ 1\rangle + 13\rangle$	10 300	16.3	22.1
ETU _{4a}	$ 0\rangle + 14\rangle$	12 100	59.8	55.7
ETU _{4b}	$ 0\rangle + 15\rangle$	12 300	1.3	1.6

Finally, ETU enters the rate equations for $|4\rangle$, from which each of the individual ETU processes originates, as a loss via

$$\partial_t N_4(t) \Big|_{\text{ETU}} = -2 \sum_j w_{\text{ETU},j} N_4^2$$

and add to each of the two receiving levels $|j\rangle$ as

$$\partial_t N_j(t) \Big|_{\text{ETU}} = +w_{\text{ETU},j} N_4^2 .$$

The respective receiving levels are shown in Table 5.1.

CROSS RELAXATION CR is the primary quenching mechanism in highly doped neodymium materials [49]. In the present systems, there is one single CR process with a non-vanishing overlap integral, namely $|4\rangle + |0\rangle \rightarrow 2 \cdot |3\rangle$. This can be described by the single coefficient w_{CR} , which has been calculated from another experimentally derived concentration dependence in Ref. [169],

$$w_{\text{CR}}(N_0) = 6.40 \cdot 10^{-51} \text{ m}^6 \text{ s}^{-1} \times N_0 .$$

For the FCZ5 sample the coefficient amounts to $5.62 \cdot 10^{-24} \text{ m}^3 \text{ s}^{-1}$. The value is about two orders of magnitude smaller than the corresponding ETU net rate, which appears to be common [169]. The result also compares quite

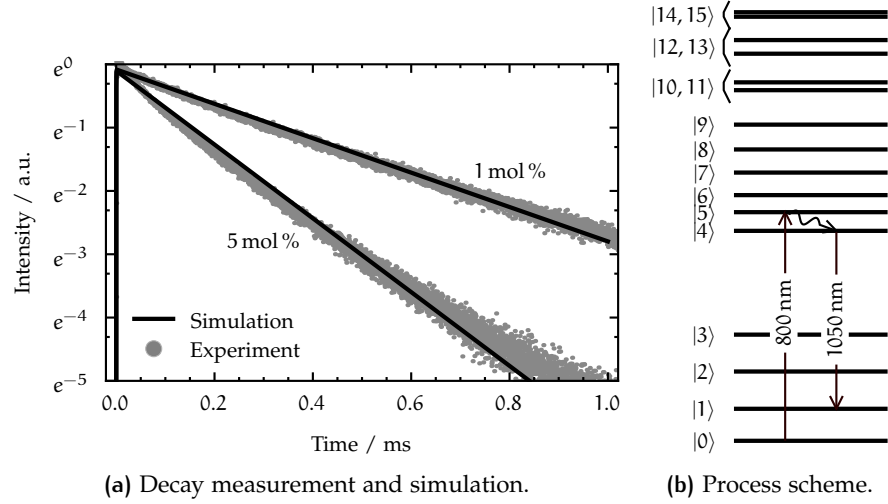


Figure 5.4: 1050 nm emission upon pulsed excitation at 800 nm at 10 mW average power. The decay is shown for the low and high dopant level from the samples FCZ1 and FCZ5. Concentration quenching decreases the lifetime in FCZ5. The solid lines are the results of the respective simulations.

well to a value of $3.4 \cdot 10^{-24} \text{ m}^3 \text{ s}^{-1}$ given in the literature for neodymium-doped ZBLANP glass [109].

With the w_{CR} coefficient known, CR is considered in the equation for $|4\rangle$ as a loss,

$$\left. \partial_t N_4(t) \right|_{\text{CR}} = -w_{\text{CR}} N_4 N_0 ,$$

and adds to the receiver $|3\rangle$ as a gain,

$$\left. \partial_t N_3(t) \right|_{\text{CR}} = +2w_{\text{CR}} N_4 N_0 .$$

CONCENTRATION QUENCHING OF PL With these processes integrated into the time-dependent model it becomes possible to simulate concentration-quenched decays to test the ETU and CR coefficients. Experimental decay traces obtained from samples with different doping levels are shown in Fig. 5.4. The experiment was carried out in pulsed regime at 800 nm. Consequently, ESA is not active here, since the $|4\rangle \rightarrow |15\rangle$ ESA step under 800 nm pumping involves the nonradiative transition $|5\rangle \rightarrow |4\rangle$ by the emission of phonons, which proceeds on time scales orders of magnitude slower than the femtosecond pump pulse. The solid lines in the figure show the simulation of the experiment at an average power of 10 mW. The concentration quenched decay is well-described, which verifies the involved coefficients.

5.2 SIMULATION OF CONTINUOUS-WAVE EXCITATION

NEW PROCESSES The rate equation model description of neodymium comprises of around 150 unique coefficients at this point and nearly twice that

considering the effective-medium model of the glass ceramic. From the overlap study, several new processes, namely one ESA, seven ETU, and one CR process were found with non-vanishing overlap. These will be considered in the model with the equations discussed in the previous section. The level scheme in Fig. 5.5 summarizes the stationary model for the case of continuous, pumping resonant to $|5\rangle \leftarrow |0\rangle$ (and the ESA transition $|4\rangle \rightarrow |15\rangle$). For brevity, the SPE, PE and PA processes have been omitted in the figure. This model now considers power-dependent Anti-Stokes processes and is thus not trivially solved anymore as there are now quadratic terms in the population number densities.

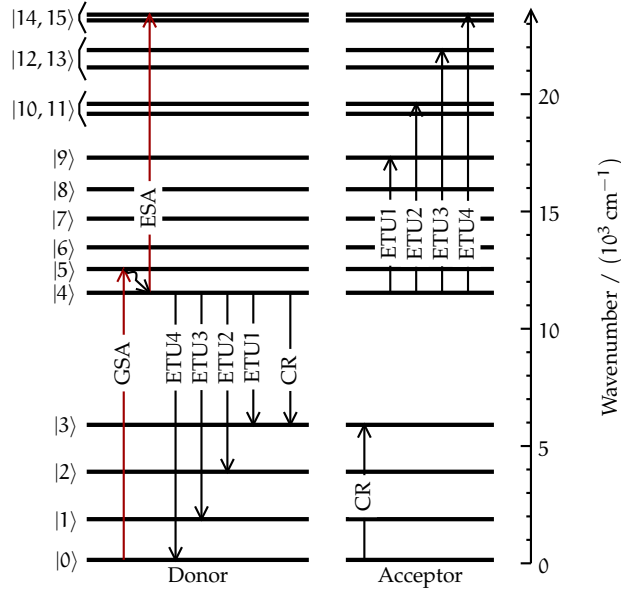


Figure 5.5: Level scheme of stationary rate equation analysis of monochromatic up-conversion. Significant processes considered in this cw pumping scheme include: GSA near 800 nm, ESA of the pump radiation, ETU, and CR. Not shown are processes involving phonons between any adjacent levels, as well as radiative decays from each level to any lower lying level. Also, stimulated emission (STE) was omitted here for brevity.

The positive, real solutions are used to describe cw-pumped upconversion emission spectra (introduced earlier in section 2.4.2). For comparison with cw-excited upconversion emission spectra, the steady-state solutions

$$I_{\lambda} = \int_0^{\infty} I'_{\lambda}(t) dt$$

were calculated from the result of Eq. (4.2.1). This integration step is equivalent to solving the rate equations with the time derivatives replaced by zero,

$$\partial_t N_j(t) \stackrel{!}{=} 0 \quad \Rightarrow \quad 0 = N_j(t) \sum_i A_{\text{decay},i}.$$

SPECTRAL RESOLUTION As the experimental spectra consist of multiple overlapping emissions again, and an individual decomposition of contributing lines would be inferred by larger errors, intensities were further summed up to cover any emission within predefined spectral ranges. Fig. 5.6 shows

a representing upconversion emission spectrum recorded upon monochromatic cw excitation at 800 nm. The spectrum is sectioned into five spectral regions. All emissive contributions within such emission interval are integrated over in both the simulations and the experimental data processing in order to be able to compare the two. This principle is denoted by the grey shading of the spectral range (III) in the figure.

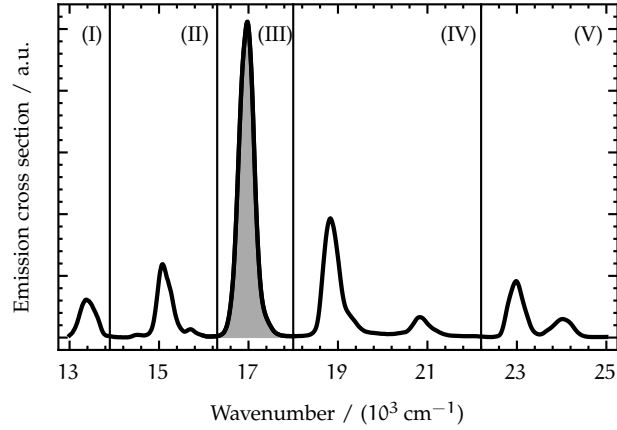


Figure 5.6: Upconversion emission cross section spectrum recorded from highly doped FCZ5-c glass ceramic upon continuous irradiation with 800 nm at 85 mW. The sketched spectral intervals (roman numerals) were used to integrate the intensity over for comparison with the simulation results in the stationary state. The integration procedure is shown for spectral range (III).

PHOTON FLUX To be able to compare the simulation results with experiments in the next section, an absolute measure must be found, which can be derived from both the simulation result and the experimental signal obtained from the measurement apparatus. A superposition of normalized data as with the Stokes-type processes in chapter 4 is not valid anymore, due to the nonlinearity in the power-dependence of the model now encompassing Anti-Stokes-type processes. The photon flux is the common measure readily available from the simulation results that can also be systematically estimated from the measurement data.

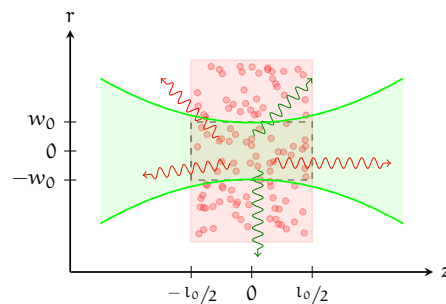


Figure 5.7: Schematic of Gaussian laser profile (light green) that leads to an excitation of neodymium ions (red) within the approximately cylindrical excitation volume (denoted by dashed lines). The PL photons generated within this volume flow out omnidirectionally through the cylinder surface (squiggled arrows).

Consider, as schematically shown in Fig. 5.7, a continuous laser beam entering the sample at $z = 0$ on the optical axis at $r = 0$, which has its focus set at approximately $z = 0$. Its Gaussian intensity profile $I(r, z)$ is located approximately between $r = \pm w_0/2$ and brings with it an excitation photon flux $I/(h\nu)$ through the entrance area πw_0^2 . Its electric field now excites neodymium ions located within the approximately cylindrical² excitation volume with a probability given by $\sigma_0 N_0$. The resultant excitation rate is described by $\partial_t N_{\text{GSA}} = I(r, z) \sigma_0 N_0 / (h\nu)$. Subsequently, the excited ions decay statistically, and with a probability given by the product of the Einstein coefficient and the emitting level's population density, photons of a certain energy are emitted, as in $\partial_t A_{\text{SPE}} N_{\text{SPE}}$. The wavelength corresponding to this photon energy is determined by the actual radiative transition $|i\rangle \rightarrow |j\rangle$ via $\lambda = hc / (E_i - E_j)$. Finally, the PL photons thus generated within the volume $V_{\text{cyl}} = \pi w_0^2 l_0$ is then leaving it as a photon flux

$$\Phi_{j \rightarrow i} = \sum_{j \rightarrow i} \frac{1}{A_{\text{cyl}}} \int_{\text{cyl}} A_j \beta_{j \rightarrow i} N_j dV_{\text{cyl}}$$

through its surface $A_{\text{cyl}} = 2\pi w_0(w_0 + l_0)$.

5.3 COMPARISON TO EXPERIMENTAL UPCONVERSION SPECTRA

Testing the coefficients for ion-ion processes while keeping the established coefficient sets fixed, is carried out with power-dependent measurements of upconversion spectra, as the population density enters the equations with quadratic terms and is hence depending nonlinearly on the pump power.

5.3.1 Estimation of experimental photon flux

As described in the previous section, the comparison between the two is only meaningful if both are brought to the same units. While the simulation results were already converted to a photon flux for each of the spectral intervals given in Fig. 5.6 in order to maintain spectral resolution, the experimental data is not converted as easily and the photon flux can only be estimated. Experimental spectra are obtained from a setup such as shown in Fig. 2.8 and a conversion is required from the detector (PMT) signal usually given in raw counts to the corresponding photon flux out of the excitation volume in the sample. The detailed calculation of this is shown in appendix A.3.2.

Note however that no step involves any empirical correction or discrimination between light from glass or glass-ceramic samples. The treatment of the individual spectral ranges is also the same in each case so that a direct comparison of the absolute values becomes possible.

² Given loose enough focusing and samples thin enough to fulfill $z_R \sim l_0$, with z_R the Rayleigh length of the beam, the beam waist $w(z)$ does not change much ($w(z) \leq \sqrt{2}w_0 \quad \forall z \leq z_R$) along the sample thickness.

5.3.2 Continuous infrared laser excitation

From the four spectral ranges shown in Fig. 5.6, the integrated emission intensities were determined experimentally over one order of magnitude of cw pump power. The comparison between the simulation and the experimental data is shown for each spectral range on doubly logarithmic scale in Fig. 5.8.

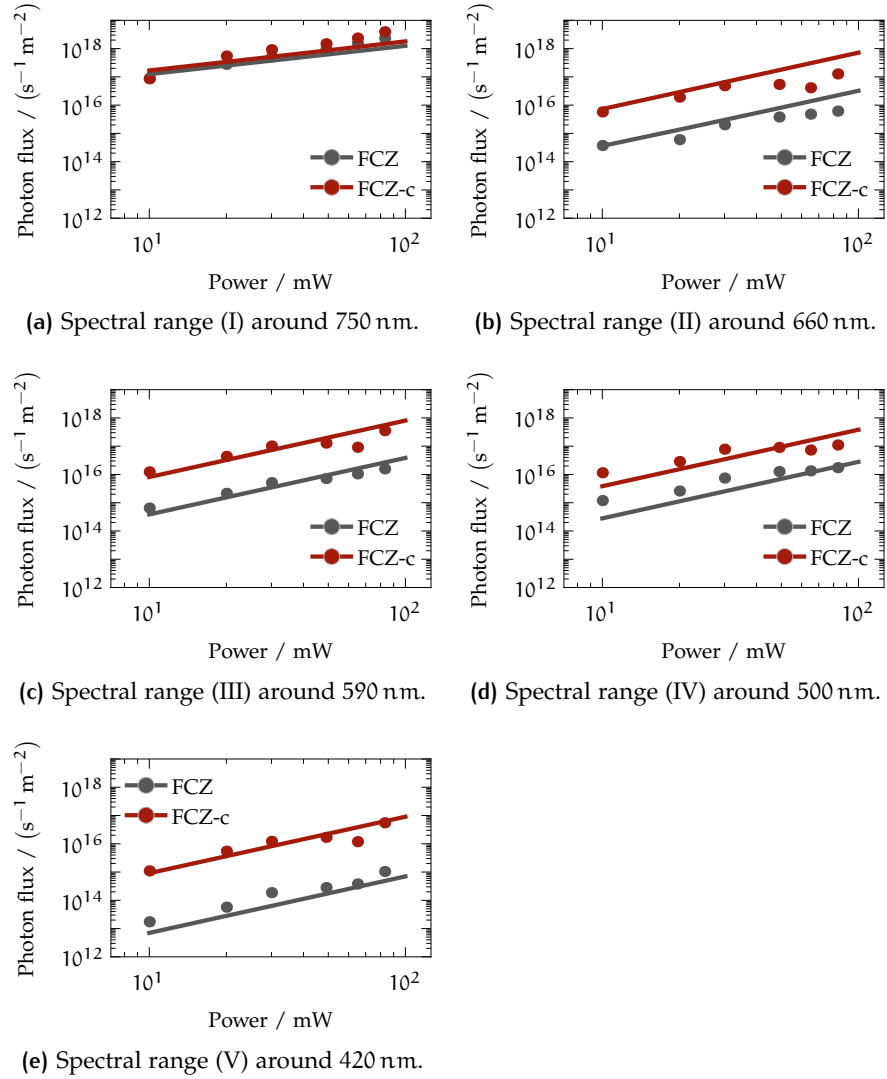


Figure 5.8: Comparison of steady-state simulation results (solid lines) to experimentally determined, integrated upconversion photon flux (data points) from FCZ5 glass and FCZ5-c glass ceramic. Excitation was carried out monochromatically at 800 nm in continuous-wave regime. The five individual figures show the power-dependence of the emissions on the exact same logscale for comparison. Each subfigure corresponds to one of the five spectral integration ranges (roman numerals) introduced in Fig. 5.6.

There are two main observations to be made. First of all, the upconversion emission intensities increase monotonically with increasing input power. Further, on the doubly logarithmic scale, the order of the process can be extracted from the slope of the graph. For levels which are receiving population from energy transfer, the quadratic power-dependence is expected

since a two-step ETU was considered in the model. This is also reflected in the experimental data, especially for the lower pumping powers. The second main observation is that the FCZ5-c upconversion emissions overcome the FCZ5 emissions by one to two orders of magnitude. Interestingly, this is the case even for the data points where there are discrepancies between simulation and experiment as both datasets appear to change well-correlated in any case.

It can be seen that the main upconversion emissions are from the green spectral region comprised of the sectors (III) and (IV) (see Fig. 5.8c and Fig. 5.8d) which are one order of magnitude above the violet/blue range (V) (Fig. 5.8e) and the red emission range (II) which is also comparably strong (Fig. 5.8b). For range (V), the intensity increase through the nanocrystals is by almost two orders of magnitude. For range (IV) it is one and for the sectors (III) and (II) it is something in between one and two orders of magnitude. The spectral range (I) (Fig. 5.8a), which is supposed to be dominated by Stokes-type emission, shows the strongest photon flux and no significant difference between glass and glass ceramic.

Deviations between experiment and simulation are of two types. In range (IV) and (II), the experimental data are systematically above or below the simulated points by less than 50%. Another systematic deviation superimposed to this is found in all graphs for the three highest pump powers, where the experimental data points drop more or less while the simulation does not.

5.4 DISCUSSION

The discussion is divided into two parts concerning at first the observations and limits of the simulations in general and at second, the nanocrystal influence on upconversion luminescence enhancement.

5.4.1 Population mechanisms

RANGE (I) With photon fluxes of $1.2 \cdot 10^{17}$ to $1.0 \cdot 10^{18} \text{ m}^{-2} \text{ s}^{-1}$ for FCZ and $1.7 \cdot 10^{17}$ to $1.5 \cdot 10^{18} \text{ m}^{-2} \text{ s}^{-1}$ for FCZ-c, range (I) around 750 nm contains the majority of the emission intensity, which is however not caused by Anti-Stokes upconversion processes. In fact, it shows almost exclusively population decay originating from the metastable level system comprised of the levels $|4\rangle$ to $|6\rangle$ that leaves the state via $|6\rangle \rightarrow |0\rangle$. It is therefore mainly populated by phonon absorption from $|4\rangle$ and $|5\rangle$ and thus shows an almost linear power dependence. It is also the reason why there is no apparent change between FCZ and FCZ-c, as, whenever there is no de-excitation dependence on phonons due to the coupling to $|4\rangle$, there must not be any emission change upon the reduction of the phonon emission rate for $|4\rangle \rightarrow |3\rangle$. Still, the experimental data exhibit a slope that is just above the expected slope of 1 as further emissions in that wavelength range also contribute to it (nonlinearly in the excitation power). These slightly underestimated contributions are most likely from $|9\rangle \rightarrow |2\rangle$ and $|11 + 10\rangle \rightarrow |3\rangle$, both at around 750 nm.

RANGES (II) TO (IV) The second highest emission intensity is found in the spectral ranges (II) to (IV) with photon fluxes between $3.8 \cdot 10^{15}$ and $5.0 \cdot 10^{17} \text{ m}^{-2} \text{ s}^{-1}$ for FCZ-c, and one to two orders of magnitude less for FCZ. Contrary to range (I), these are pure Anti-Stokes-type upconversion emissions. The major transitions are $|13 + 12\rangle \rightarrow |3\rangle$, $|11 + 10\rangle \rightarrow |2\rangle$, and $|9\rangle \rightarrow |1\rangle$ at around 660 nm in range (II), as well as $|15 + 14\rangle \rightarrow |3\rangle$, $|13 + 12\rangle \rightarrow |2\rangle$, $|11 + 10\rangle \rightarrow |1\rangle$, and $|9\rangle \rightarrow |0\rangle$ near 580 nm in range (III), and finally $|15 + 14\rangle \rightarrow |1\rangle$, $|13 + 12\rangle \rightarrow |0\rangle$ near 490 nm and $|15 + 14\rangle \rightarrow |2\rangle$, $|13 + 12\rangle \rightarrow |1\rangle$, and $|11 + 10\rangle \rightarrow |0\rangle$ near 510 nm, all in range (IV). Since the involved levels are exclusively excited via two-step upconversion processes, the slope of their power-dependencies is also two. The involved source levels $|15 + 14\rangle$, $|13 + 12\rangle$, $|11 + 10\rangle$ and $|9\rangle$ were also already shown to luminesce efficiently in Table 4.1, where their radiative quantum efficiencies η were all found to be $>1\%$ in FCZ-c. The remarkable increase of η upon nanocrystal growth for these levels is in perfect agreement to the drastic emission increase found experimentally for these spectral ranges. The reason is that the strong reduction of the phonon emission rate drastically favors the radiative decay connected to already quite significant radiative emission rates for these levels found in Table 3.6.

RANGE (V) Range (V) features the weakest emission intensities between $9.1 \cdot 10^{14}$ and $6.2 \cdot 10^{16} \text{ m}^{-2} \text{ s}^{-1}$ for FCZ-c and two orders of magnitude less for FCZ. The reason is that this level is not just reached under maximal exhaustion of the upconversion excitation energy, but it also is quickly depleted nonradiatively to contribute to emission from the stronger levels below. The transitions contributing the major part to range (V) is $|15 + 14\rangle \rightarrow |0\rangle$. This is due to the fact that 800 nm excitation at such excitation powers results in only second-order upconversion. Three-step processes as required to significantly populate even higher levels, are not found for the excitation powers used during this analysis. The remarkable change of almost two orders of magnitude of luminescence intensity upon the transition from FCZ to FCZ-c in the case of range (V) is fostered by the fact that η of $|14\rangle$ undergoes the maximum change with the nanocrystal growth.

MAJOR EFFECTS The parameter sets already involved in the model description in chapter 4 could more or less be checked individually against selective experiments. This is not the case for the new parameters introduced in this chapter, which are responsible for the Anti-Stokes emissions. Because of this all relevant simulation parameters were varied systematically to isolate their impact on the simulated power-dependent upconversion spectra, and to find certainty limits. Specifically, setting w_{ETU} to ten times its assumed value increased the upconversion photon flux in the ranges (II) to (V) by a factor of ten. Similarly, the reduction by the same amount lead to the expected decrease. From this it is concluded that ETU is the major population mechanism for upconversion emitting levels and ESA at the pump wavelength used here does play no dominant role. Upon the ten-fold increase in w_{ETU} , emission from range (I) remained approximately unchanged, which is expected given the fact that there is no significant contribution at this wavelength range from high lying levels populated by upconversion mechanisms.

Interestingly, setting w_{CR} to its 10-fold value leads to a drastic reduction of emission efficiency over all ranges. The upconverted ranges (II) to (V)

weakened by around 2 orders of magnitude, while the range (I) reduced by a factor of 10. In a simplistic scheme, this is immediately explicable by the effect CR has on the start level for ETU, namely $|4\rangle$. This level loses its population about 10 times more probable with the increased w_{CR} and hence, the population from levels thermally coupled to it, vanishes by the same amount. Moreover, the upconverted emissions that depend approximately quadratic on this population, lose excitation probability by the square of this factor. From this it is clear that CR is a significant non-radiative loss mechanism that is able to efficiently deplete $|4\rangle$ and thus defeat upconverting processes in this excitation scheme. Finally this leads to a quick conversion of the excitation energy to phonons and hence heat with rates large compared to the radiative decay rate [49].

It is found that ESA is not dominating upconversion at the excitation wavelength of 800 nm in this system. The reason for this is the spectral mismatch between the pump laser wavelength and the ESA transition $|15\rangle \leftarrow |4\rangle$. This was presented in Fig. 5.2. The excitation wavelength is better matched to the GSA transition $|5\rangle \leftarrow |0\rangle$, which is expressed by the parameter ξ in Eq. (5.1.2). For a more comprehensive focus on the possible ESA contributions to a monochromatic upconversion scheme in neodymium, further experiments at slightly larger wavelength of around 810 nm might be instructive. There, a better balance between $|5\rangle \leftarrow |0\rangle$ at 803 nm and $|15\rangle \leftarrow |4\rangle$ at approximately 815 nm should be achieved.

MINOR EFFECTS For all ranges apart from (IV) the simulation follows the experimental data points quite well. This is especially true for the lower excitation powers, but apparently breaks down slightly for some of the higher excitation powers, consistently for all upconverted emissions (ranges (I) to (IV)). A possible effect able to describe the less than expected experimental emission output with respect to the simulation would be some kind of saturation at the pump wavelength. This would imply such a significant accumulation of neodymium in excited states that the remaining ground-state population is not able to further absorb pump light with the same (unsaturated) probability anymore. The samples would then become increasingly transparent. However, such power-dependent bleaching is not found, as shown in Fig. 5.10b.

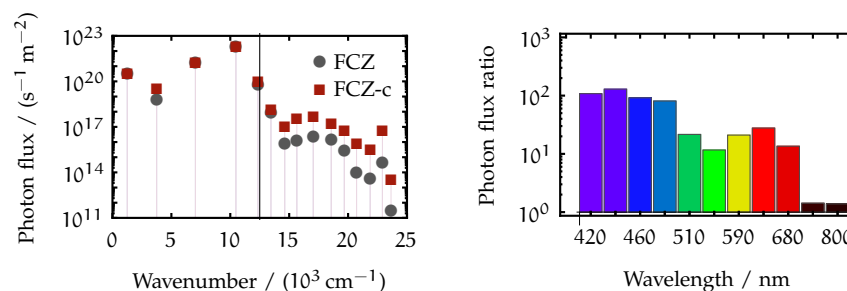
In the figure, where the transmitted power is monitored with respect to the input power launched into the sample at the laser excitation wavelength, there is no apparent deviation from the linear curve. However, although not the whole power range of Fig. 5.8 is covered in Fig. 5.10b, the remaining data points should already show a significant deviation if saturation bleaching was the problematic effect shown in the power-dependent upconversion spectra. It is furthermore suspected that temperature-dependent alterations in the laser diode's beam profile are the reason for the consistent deviations at higher pump powers. As a consequence of the high thermal load at these powers, the diode head, which is a non-symmetric element, undergoes non-symmetric thermal expansion as soon as the cooling power of the diode package is not sufficient any longer in keeping temperature profile and wavelength. Together with the symmetry of the diode itself, the symmetry of the emitted beam deteriorates with the result of changing beam parameters such as beam waist and focal position. From the beam profiles shown in appendix A.2.1 this is clearly evident. Moreover, different foci in x- and y-direction are a common problem for solid-state laser diodes that

is usually corrected for by appropriate lenses in front of the diode. It gets even worsened and is additionally amplified with the length of the beam path. As a result, the laser spot located on the samples about 1 m after the diode's output changes its position in the sample plane. For elliptic beams with different foci in x - and y -direction, the optical intensity might also change as well as the focal depth as both are determined by the axial focal positions.

5.4.2 Nanocrystal influence

MAIN LEVELS As was the case in chapter 4, the main emissions stem from the levels $|9\rangle$, $|11 + 10\rangle$, $|13 + 12\rangle$, and $|15 + 14\rangle$. More precisely, for each of the nearby levels, the lower level of each pair is the emitter equipped with the highest emission rate, due to the quick phonon-assisted population transfer. This observation is consistent with Table 4.1, where the levels $|9\rangle$, $|10\rangle$, $|12\rangle$, and $|14\rangle$ were assigned large quantum efficiencies η between around 2 to 12% in FCZ-c. It was mentioned in section 4.3.2 that these levels fulfil the proposed emission increase criteria as they have $A_{\text{SPE}} > 10^3 \text{ s}^{-1}$ and require the simultaneous emission of more than five phonons to decay via MPR. From the previous section it can therefore be concluded that the levels that were dominant for Stokes-type PL are also dominant for Anti-Stokes-type upconversion luminescence under continuous, monochromatic laser excitation.

POPULATION STORAGE With the reduced PE rate identified to be responsible for the η increase for the above-named levels, the nanocrystal growth is also expected to alter the steady-state of the neodymium ions in a way resulting in the net population to remain longer in higher lying levels. Fig. 5.9a shows the spectrally resolved photon flux of FCZ5 and FCZ5-c. The levels



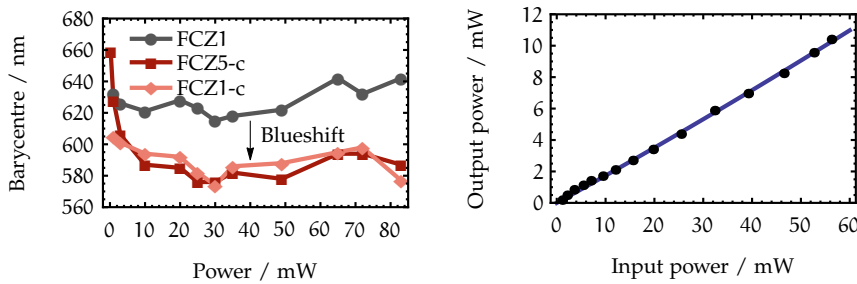
(a) Simulated spectral photon flux in stationary state. The black line separates the spectrum into upconverted (to the right) and regular (left from line) PL. (b) Ratio of spectral photon fluxes from FCZ-c and FCZ to visualize the upconversion emission increase achieved by the nanocrystals as shown in Fig. 5.9a.

Figure 5.9: Comparison of simulated spectral photon flux of FCZ5-c and FCZ5 upon continuous monochromatic excitation at 800 nm with 85 mW. Note that for both graphs, the data points show the integrated emissions at the spectral position of the nearest ground state transition.

below the upconversion wavelength border are approximately unchanged upon nanocrystal growth with the sole exception of $|2\rangle$. Above 780 nm the emissions are clearly favored in the glass-ceramic with improvements

between one and two orders of magnitude as shown in Fig. 5.9b. There, it is also shown that the strongest emission increase is achieved approximately around 440 nm and the weakest around 540 nm. This indicates that the population is indeed stored with a tendency to higher levels in the glass ceramics.

To find an experimental measure for this, the barycentre wavelength over the whole upconverted emission range between 380 nm and 780 nm was calculated with Eq. (2.4.10) for several excitation powers. The result is shown in Fig. 5.10a. In general, the power-dependent steady-state reaches a value of more or less constant barycentre wavelength at powers larger than 10 mW. Beyond that power FCZ5 approaches a mean value of around 625 nm. The glass ceramics FCZ1-c and FCZ5-c have approximately the same mean value of 585 nm after 10 mW. This huge shift of the first moment of the wavelength distribution by approximately 40 nm by the nanocrystal growth emphasizes the finding that the population is stored with a tendency towards higher levels in glass ceramics as compared to the glass sample. It is noteworthy that this effect appears regardless of the actual dopant level in the samples since FCZ1-c and FCZ5-c show nearly the same behavior in Fig. 5.10a. Note that the upconverted emission from the FCZ1 precursor glass without nanocrystals was too weak to determine a reliable barycentre wavelength and that therefore this sample is missing in the figure.



- (a) Power-dependent barycentre wavelength of upconverted emission (380 to 780 nm). The FCZ-c emissions are blueshifted by ≈ 40 nm with respect to the FCZ5 glass. Note that the upconversion emission from FCZ1 was too weak for reliable determination.
- (b) Power-dependent transmission of excitation laser diode through FCZ5-c in cw regime. As there is no evident deviation of the measurement points from the linear curve, a saturation bleaching effect is not observed.

Figure 5.10: Power-dependent barycentre wavelength and transmission upon continuous, monochromatic excitation at 800 nm.

FIGURE OF MERIT FOR SINGLE-COLOUR UPCONVERSION To quantify the efficiency yield in upconversion emission by the introduction of nanocrystals to the glass matrix, a figure of merit needs to be defined. One possibility is the definition of such (monochromatic) upconversion yield Γ_{mc} as the ratio of the upconverted photon flux from emissions at wavelengths above the upconversion wavelength (800 nm in this case) to the excitation photon flux from the laser,

$$\Gamma_{mc} = \frac{\Phi_{\lambda < 800 \text{ nm}}}{\Phi_{exc}}. \quad (5.4.1)$$

This figure has been calculated and is shown in Fig. 5.11. There, an up-

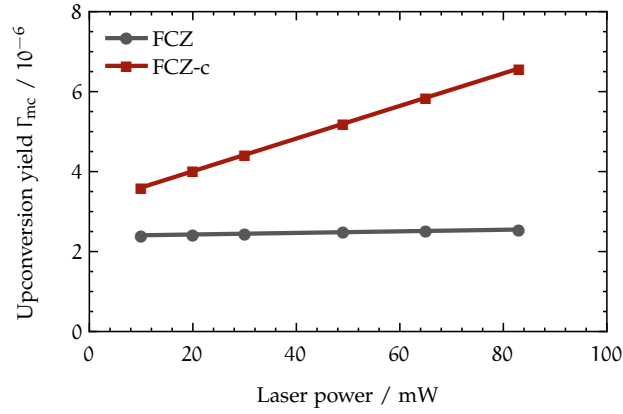


Figure 5.11: Spectral photon flux yield Γ_{mc} (defined in Eq. (5.4.1)) of FCZ and FCZ-c over monochromatic excitation power. Upconversion yield is the ratio of the emitted photon flux at wavelengths smaller than the excitation wavelength to the excitation photon flux (at the wavelength 800 nm).

conversion yield Γ_{mc} between approximately $3.5 \cdot 10^{-6}$ – $6.6 \cdot 10^{-6}$ is found for FCZ5-c, depending on the power. For the glass FCZ5, the yield is near $2.5 \cdot 10^{-6}$ and does not change much with the excitation power.

The photon flux is equal to the number of upconverted photons per excited neodymium ion under monochromatic excitation. That means that from less than 10^5 incident infrared photons approximately one visible photon is generated, which is a poor number. This low efficiency is related to the process chosen, which is the monochromatic upconversion of 800 nm light with neodymium, whose metastable level is located at an energy position equivalent to photons of wavelength 865 nm. Due to the level structure of neodymium, most of the population will quickly be transferred to the metastable level resulting in emissions mainly from the transitions $|4\rangle \rightarrow |1\rangle$ and $|4\rangle \rightarrow |0\rangle$ at 1050 and 870 nm, respectively. This is clear from Fig. 5.9a, where by far the maximal photon flux is reached for $|4\rangle$ in both samples. In the glass the efficiency is even worse than in the glass ceramic, since here almost all upconverted population relaxes back to $|4\rangle$ to emit at wavelengths longer than the excitation wavelength. Therefore Γ_{mc} is even lower in the glass and does not increase much with excitation power as the MPR-based population transfer to the metastable level largely excels the upconversion rates.

In energy level structures of rare earths like erbium the upconversion step (at $1.54 \mu\text{m}$ in the case of erbium) does not involve phonon emission at the intermediate step, and the upconverted population ends in a level with a huge energy gap and only weak phonon emission probabilities. The upconverted emission wavelength is then shorter than the excitation wavelength and nearly all excitation relaxes through this decay channel. The Γ_{mc} for erbium-based upconverters in the monochromatic scheme is therefore much more promising than for neodymium as indicated in the literature [64, 170, 171].

5.4.3 Summary

In summary, the model was successfully extended to the description of Anti-Stokes upconversion processes. In the present system, seven energy transfer, one cross relaxation and one excited state absorption process³ were found. The new parameters attached to these processes were calculated considering their spectral overlaps. The model was then tested against the power-dependence of upconverted emissions in a spectrally resolved way. It allowed fairly well simulations of the steady-state spectra upon monochromatic excitation.

Analysing the model led to the conclusions that energy transfer is the dominant upconversion mechanism. Excited state absorption on the other hand is not efficient due to the lack of optimal resonance to the pump wavelength. Cross relaxation on the other hand was found to be quite an efficient loss mechanism to the population of the metastable level. Thus, it is capable of efficiently quenching the upconverted emission, depending on the concentration of the neodymium ions. As the energy transfer upconversion emissions are also depending on this concentration, a balance needs to be found between loss and gain from more participating dopant ions, more efficient energy transfer upconversion and more loss probability via cross relaxation.

From the ratio between the photon flux at upconverted wavelengths and the excitation flux, a figure of merit for the monochromatic upconversion photon yield, Γ_{mc} was defined. The glass sample yielded values of about $2.5 \cdot 10^{-6}$ and the glass ceramic values between $4 \cdot 10^{-6}$ – $7 \cdot 10^{-6}$ upconverted photons per excitation photon. These numbers make neodymium a bad upconverter of monochromatic excitation. The reason for the poor efficiency lies in the electronic structure, where the metastable level as the main emitter is spectrally situated below the elementary upconversion step.

³ at the pumping wavelength of 800 nm

6

CONVERSION OF SOLAR RADIATION

6.1 MOTIVATION

At this point the rate equation model developed in the previous chapters is able to describe both Stokes-type photoluminescence and Anti-Stokes-type upconversion luminescence from neodymium in glasses and glass ceramics. The solutions of the differential equation system are used to calculate the spectrally resolved photon flux per wavelength interval that is emitted from the simulated samples. With the help of this system, time-dependent photoluminescence decays were successfully simulated as well as power-dependent upconversion emission spectra. Based on the results from the previous chapter, a figure of merit for the description of the upconversion emission yield, i.e. the number of upconverted VIS photons per NIR excitation photon from the laser, was calculated. Judging from this figure, neodymium-doped glasses or glass ceramics do badly as a monochromatic upconverter, which was already anticipated earlier [7, 11].

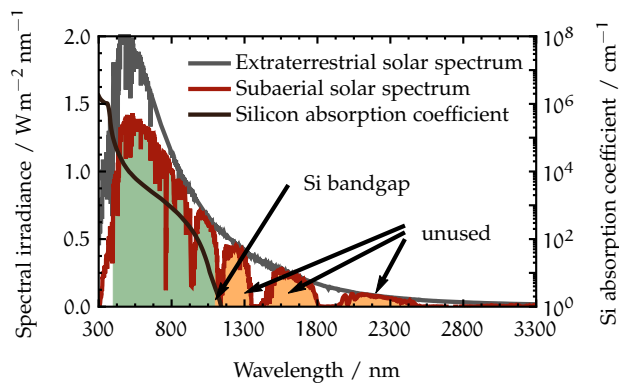


Figure 6.1: Solar spectral irradiance before (gray line) and after passage (red line) of the earth’s atmosphere (data from Ref. [172]). The black line is the absorption coefficient for silicon (data from Ref. [173]). The green filling denotes the part of the solar spectrum accessible to silicon photovoltaics, whereas the orange filling shows the unexploited, near-infrared light, a possible subject to upconversion to the visible range.

In this chapter it will be demonstrated how this situation changes upon the introduction of broadband irradiation with the near-infrared part of the solar spectrum. In contrast to the monochromatic upconversion regime based on laboratory laser excitation, this application scheme approaches in a tailored way the problem of the unexploited near-infrared sunlight present in current real-world silicon photovoltaics, where the sunlight with photon energies below the silicon bandgap (corresponding to wavelengths longer than 1100 nm) is not contributing to the photoelectric conversion (see

Fig. 6.1). The target of a photovoltaic upconverter is to make the so far unused 180 W/m^2 available at last to the silicon solar cell.¹

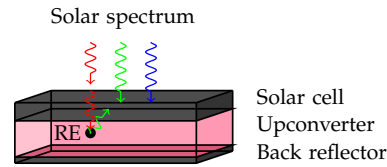


Figure 6.2: Schematic of upconverter device attached to the bottom of a bifacial silicon solar cell. The incident sunlight is absorbed well in the visible spectral range (blue and green arrows). The near-infrared part of the sunlight is transmitted and upconverted in the bottom layer. The resulting visible photons are radiated either directly back to the cell on top or via the back reflector. Inspired by Ref. [11].

In the following sections, the feasibility of an neodymium-based photovoltaic upconverter below a bifacial silicon solar cell is evaluated (see Fig. 6.2 for a schematic). As a quantitative measure, the figure of merit from the previous chapter (see Eq. (5.4.1)) is extended to encompass the number of generated VIS photons per solar NIR photon.

6.2 BROADBAND EXCITATION

6.2.1 Overlaps in steady-state neodymium

During the analysis of neodymium dynamics it turned out that numerous spectral overlaps and quasi-overlaps are to be considered for neodymium emissions in this amorphous host, due to the electronic level structure. The four J-levels of the ^4I manifold ($|0\rangle$ to $|3\rangle$) are almost equally spaced by approximately 2000 cm^{-1} . The same spacing is found even more often between higher levels including non-adjacent ones, as in between $|4\rangle$ and $|6\rangle$, $|5\rangle$ and $|7\rangle$, or between $|10\rangle$ and $|12\rangle$. Further energy spacings are also found to repeat during the level scheme. Whenever two energy differences do not match perfectly, a quasi resonance is achieved through the huge line widths from the amorphous host matrix as was discussed in section 2.5.2. A consequence of this peculiar structure is that the numerous spectral overlaps between photoluminescence emissions from different source levels had to be considered in the rate equation model (cf. Eq. (4.2.1)). In Fig. 4.4 the number of spectral overlaps was shown for emissions at a certain frequency with a mean of about two transitions over the whole spectral range between 5000 cm^{-1} and 22000 cm^{-1} .

The consequence of this electronic structure is that under steady-state conditions with all excited states populated the neodymium-doped glasses and glass ceramics are nearly opaque for broadband illumination, for example from the near-infrared part of the sunlight. The steady-state is at the same time easily reached by a combination of phonon absorption and the broadband excited-state absorptions. In Fig. 6.3 the number of ESA transitions

¹ The value of 180 W/m^2 is the power density of the subaerial solar spectrum in the spectral range between $1.1 \mu\text{m}$ to $3.5 \mu\text{m}$. This is about 20% of the total subaerial power density of the sunlight (with reference to $AM_{1.5}$ [172]).

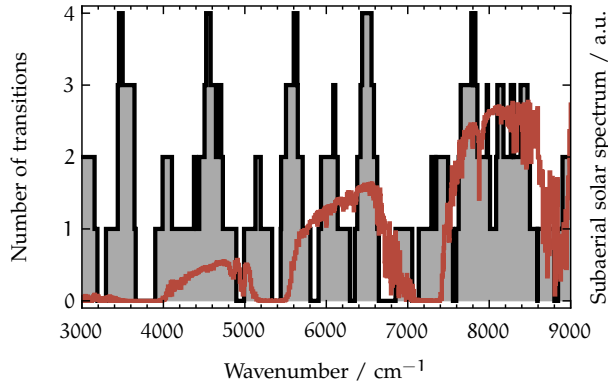


Figure 6.3: Number of ESA/GSA transitions per energy interval $\pm k_B T/2$ in steady-state neodymium.

per energy interval is given. As an estimation, two transitions are taken as quasi-resonant, whenever their spectral distance is less than $k_B T/2$. This is a rather conservative estimation given the significant line widths presented in Table 2.5. Two representing upconversion schemes, where several of these ESA transitions at different wavelengths lead to successive upconversion, are sketched in Fig. 6.4.

For photovoltaic upconversion of the light transmitted and unused by a silicon solar cell this means that unlike narrowband monochromatic upconverters, this system might prove adequate to an efficient exploitation of significant parts of the available photon spectrum.

6.2.2 Modelling broadband continuous NIR excitation

The stationary rate equation model from the previous chapter is extended to broadband pumping with the near-infrared part of the solar spectrum. For this, the multiple ESA transitions possible with the remainder of the subaerial solar spectrum [172] derived after cutting at 1100 nm were gathered (see Fig. 6.1). From the list, ESA cross sections were calculated using Eq. (5.1.2). The pump rate ρ_0 for a given ESA line was determined via the integrated solar photon flux Φ_\odot , directly from the solar spectral irradiance $F_\odot(\lambda)$ via

$$\Phi_\odot = \int \frac{F_\odot(\lambda)\lambda}{hc} d\lambda.$$

Note that $F_\odot(\lambda)$ is the subaerial solar spectral irradiance derived from reference data [172], and that it is restricted to wavelengths longer than 1100 nm. Altogether, around 40 ESA transitions with relevant σ_{ESA} were found for the steady-state neodymium under solar NIR illumination. It is noteworthy that due to the available photon energies all levels are involved. Levels $|0\rangle$ to $|10\rangle$ are occurring as source levels, levels $|2\rangle$ to $|15\rangle$ as receiving levels. The levels in both lists, $|2\rangle$ to $|10\rangle$, are both source and receiver levels.

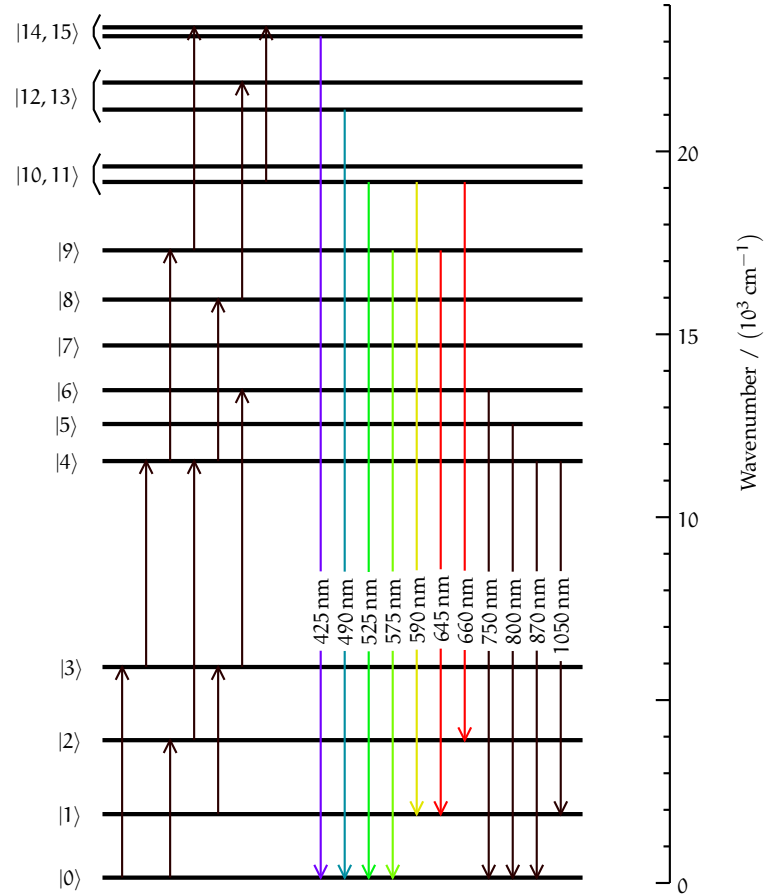


Figure 6.4: Example for a multicolour ESA-based upconversion route in stationary neodymium under continuous illumination with broadband near-infrared sunlight.

6.2.3 Concentration-dependent solar upconversion yield

It is clear from the single-colour power-dependency examination from Fig. 5.8 that the upconversion yield is strongly determined by the pump rate ρ_0 , which is itself inverse proportional to the area the incident excitation beam is focused on. The consequence is that upconverting bottom layers for silicon solar cells will not be efficient under plain sunlight. However, upon sufficient solar concentration by curved mirrors or lens systems, the upconversion yield might become notable.

It is therefore instructive to analyse the dependence of the upconversion yield on the solar concentration. Based on the definition of the monochromatic upconversion yield in Eq. (5.4.1), the broadband upconversion yield

$$\Gamma_{\odot} = \frac{\Phi_{\lambda < 1100 \text{ nm}}}{\Phi_{\odot, \lambda > 1100 \text{ nm}}}$$

is defined as the ratio of the photon flux of upconverted photons with wavelengths shorter than 1100 nm to the incident solar photon flux with wavelengths longer than 1100 nm. Note that Φ_{\odot} does not include the solar spectrum with $\lambda < 1100$ nm. The concentration factor as the number of suns is considered as a factor in the formulation of ρ_0 .

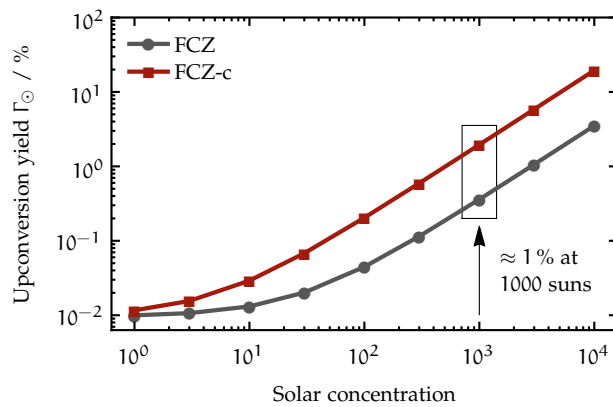


Figure 6.5: Upconversion yield vs. number of suns. From one sun, only the near-infrared spectral region above 1100 nm is taken into account.

The result of the power-dependent solar broadband upconversion is shown in Fig. 6.5.² The solar concentration was varied between 1 and 10^4 suns. For a solar concentration of 10^3 , which is about the value feasible today in solar concentrators, the system generates approximately 0.4% and 2.0% additional photons in the visible from the incident near-infrared solar excitation photons for the glass and the glass ceramic, respectively.

6.3 DISCUSSION

6.3.1 Interpretation of the results

Trupke *et al.* already mentioned in their work on solar cell efficiency improvement by upconversion that the literature does not yet include much discussion on ESA-type upconversion with more than one excitation wavelength [26]. However, in quite a contrast to the poor performance under monochromatic excitation outlined in chapter 5, the neodymium-based upconverter performs significantly different under broadband excitation with near-infrared sunlight. As already outlined by Trupke *et al.*, the reason for the different scientific focus is the huge interest in short-wavelength lasers, where merely monochromatic pumping is relevant. This initial focus on single colour upconversion in connection to the requirement that the upconverted emission should be spectrally just above the silicon bandgap did not lead to a focus on the rare earth neodymium as its basic monochromatic upconversion step is limited by the spectral position of the ESA step at 800 nm and hence useless for silicon photovoltaics.

The conclusion of Fig. 6.5 is that given sufficient solar concentration the neodymium upconverter allows for favorable upconversion of photons from nearly the whole spectral range of near-infrared sunlight left after the initial solar cell transmission. The generally low ESA cross sections of neodymium are compensated by the number of possible ESA transactions in steady-state neodymium. The performance of the neodymium-doped glass is even improved by the growth of the nanocrystals leading to an efficiency increase

² for a 1 mm thick upconverting layer

of around a factor of 5 starting at 10^2 and higher solar concentration in the glass ceramic.

6.3.2 Comparison of neodymium with other rare earths

From the results presented it must be concluded that the electronic energy level structure of neodymium is a key property for the working broadband upconversion mechanism. It is therefore instructive to compare neodymium to the other prominent RE ions to be able to decide if other RE ions might as well perform efficient under broadband solar NIR excitation.

Several criteria that are either soft or hard requirements for broadband upconversion of near-infrared light to above the silicon bandgap are defined according to which the individual RE ions will be evaluated in the following:

1. The presence of nearly equally spaced levels in the lower energy region with medium large energy gaps that are also matched by photons from the subaerial solar spectrum (around 1200 nm, 1500 nm, 2200 nm, and 3000 nm).
2. This energy level ladder ends with a large energy gap (more than about 3000 cm^{-1}). The level on top is thus metastable as its quantum efficiency will be equal to or close to unity due to inefficient multiphonon relaxation. The gap should also not be too large to not be unbridgeable by solar near-infrared photons.
3. The spectral position of the metastable level should not be too far above the silicon bandgap position not to waste too much excess energy to the kinetic energy of the charge carriers.
4. The branching ratios of the metastable level are such that the majority of the emission is emitted at wavelengths below 1100 nm.

For the detailed quantitative description of the emitting levels of the different rare earth ions, the quantum efficiency definition for an emitting level $|i\rangle$ is modified,

$$\eta_{\text{PV},i} = \frac{\beta_{ij} A_{\text{SPE},i}}{W_{\text{PE},i} + A_{\text{SPE},i} \sum_{j<i} \beta_{ij}} \quad \forall i, j : \lambda = \frac{hc}{E_i - E_j} \leq 1100 \text{ nm},$$

to account only for emission at upconverted wavelengths smaller than 1100 nm. Fig. 6.6 schematically shows the energy levels of the trivalent lanthanides. In the following paragraphs the spectra of most trivalent lanthanide rare earth ions are discussed in the order of their atomic number. The η_{PV} given are calculated assuming a ZBLAN host matrix with radiative decay rates from the literature [90, 175].

CERIUM The sole transition $|^2F_{7/2}\rangle \rightarrow |^2F_{5/2}\rangle$ in Ce^{3+} is at 5000 nm and thus allows no upconversion mechanism.

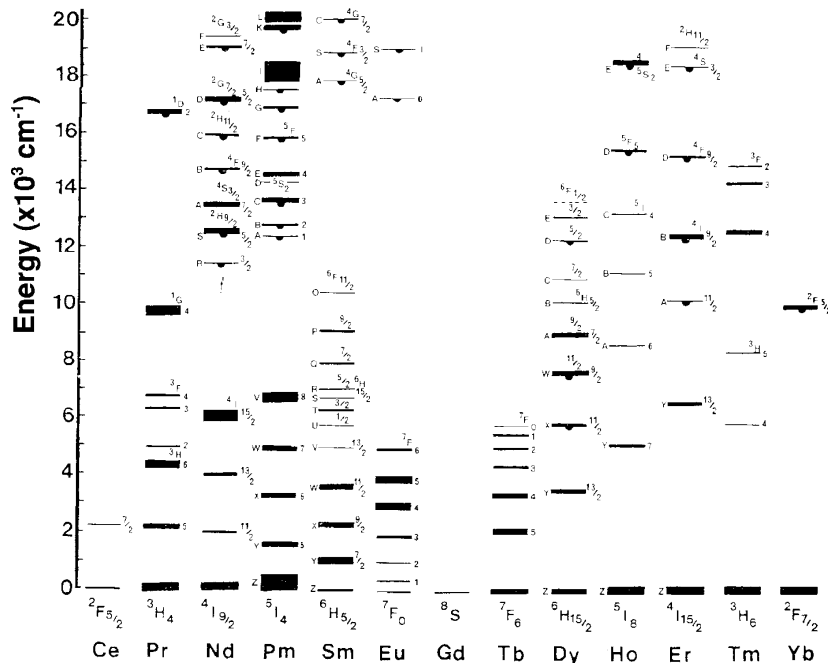


Figure 6.6: Electronic structures of several RE ions in comparison. From Ref. [174].

PRASEODYMIUM Pr^{3+} features an optimal energy level ladder structure from the ground state $^3\text{H}_4$ up to the excited state $^3\text{F}_4$ at almost 7000 cm^{-1} . On top of the adjacent large energy gap is the metastable level $^1\text{G}_4$ at 9800 cm^{-1} , whose spectral position is just above the silicon bandgap. From there most of the transitions end in $^3\text{H}_5$ and $^3\text{H}_6$ at 1300 nm and 1850 nm with branching ratios of 65% and 23%, respectively. Only 7% end in the ground state with emission at 1020 nm . Hence, there is only a poor quantum efficiency η_{PV} of 6%.

There are emissions at wavelengths $<1100\text{ nm}$ from the high lying level $^1\text{D}_2$ at 16700 cm^{-1} to $^3\text{H}_4$ (38%, 600 nm), $^3\text{H}_6$ (12%, 810 nm), $^3\text{F}_2$ (13%, 850 nm), and $^3\text{F}_4$ (25%, 1010 nm) with a total quantum efficiency of η_{PV} of 90%. However, a lot of energy is wasted to phonon emission in these cases as the starting level is 7000 cm^{-1} above the silicon bandgap. Moreover, the efficiency of the required upconversion steps are expected to be poor due to the high order required to populate the high lying level with solar near-infrared radiation.

NEODYMIUM The low-step energy ladder in Nd^{3+} starting from the ground state $^4\text{I}_{9/2}$ to the last excited state $^4\text{I}_{15/2}$ before the comparably large energy gap of 6000 cm^{-1} is suitable according to the requirements (1) and (2). The energy steps found there and above the metastable level $^4\text{F}_{3/2}$, from which most of the emissions commence, are also accessible with the solar near-infrared bands. $^4\text{F}_{3/2}$ is around 2000 cm^{-1} above the silicon bandgap. Transitions to $^4\text{F}_{11/2}$ and $^4\text{I}_{9/2}$ at 1050 nm and 870 nm with β of 48% and 41%, respectively, amount for the quantum efficiency of η_{PV} of 90%, which is rather optimal.

PROMETHIUM Pm^{3+} has an optimal energy step ladder from ${}^3\text{H}_4$ to ${}^3\text{F}_4$ at roughly 7000 cm^{-1} , followed by the large energy gap. The metastable level on top is located at around 12000 cm^{-1} . Although these structural properties are appealing, Pm^{3+} is naturally occurring only in traces of one particular isotope (${}^{147}\text{Pm}$), which is an efficient β^- -emitter³ and hence unsuitable.

SAMARIUM In Sm^{3+} a very low-energy ladder is found that ranges up to and above the silicon bandgap position. A large energy gap with a metastable level (${}^4\text{G}_{5/2}$) lies very high at more than 8000 cm^{-1} over the silicon bandgap. Hence, this ion is more suitable as a photon downconverter [176].

EUROPIUM The very low-energy ladder from the Eu^{3+} levels ${}^7\text{F}_0$ to ${}^7\text{F}_6$ at about 5000 cm^{-1} is followed by a very large energy gap of 12000 cm^{-1} under ${}^5\text{D}_0$. This exceptionally large gap is not bridgeable with near-infrared photons and there is also no apparent upconversion scheme possible here as the large gap is larger than the energy of the largest low-energy excitation step.

GADOLINIUM Gd^{3+} features no levels above the ground state ${}^8\text{S}_{7/2}$ that are within the analysed spectral range.

TERBIUM The situation in Te^{3+} is similar to the Eu^{3+} case. A suitable low-energy ladder from ${}^7\text{F}_6$ to ${}^7\text{F}_0$ at almost 6000 cm^{-1} is followed by an energy gap of 14000 cm^{-1} , which is even larger than in europium. The adjacent level ${}^5\text{D}_4$ at 20000 cm^{-1} is the possible emitter level, which is however not reachable with near-infrared photons.

DYSPROSIUM The Dy^{3+} ion shows a fairly low-step energy level ladder from ${}^6\text{H}_{15/2}$ to ${}^6\text{F}_{1/2}$ at 13500 cm^{-1} . The adjacent large gap is under the level ${}^4\text{F}_{9/2}$ at 21000 cm^{-1} . The ladder is hence going too far above the silicon bandgap for optimum conversion efficiency. The simulation is therefore comparable to the case of samarium, but shifted to even higher energies. A second metastable level, ${}^6\text{H}_{13/2}$, exists, which is the first excited state. As it is located at 3000 cm^{-1} corresponding to emission at $3.3\text{ }\mu\text{m}$ however, it is unsuitable for this application.

HOLMIUM The energy level ladder in Ho^{3+} is not optimal as the first step between ${}^5\text{I}_8$ and ${}^5\text{I}_7$ is of about 5000 cm^{-1} . The next step to ${}^5\text{I}_6$ amounts for another 3500 cm^{-1} . Following the next step is a level with a non-vanishing, but very small η_{PV} of 1%, which is due to the very low A_{SPE} of the level. Even further above is another metastable level with a promising η_{PV} , namely ${}^5\text{F}_5$ at 17000 cm^{-1} . However, this is already lying quite high and is wasting a lot of excess energy. Nonetheless it features two suitable emissions, $|{}^5\text{F}_5\rangle \rightarrow |{}^5\text{I}_8\rangle$ at 650 nm and $|{}^5\text{F}_5\rangle \rightarrow |{}^5\text{I}_7\rangle$ at 970 nm , with a faint total of η_{PV} of 2%.

³ The β^- -decay commences as ${}^{147}\text{Pm} \rightarrow {}^{147}\text{Sm} + e^- + \bar{\nu}_e$ with a half-time of approximately 2.6 years.

ERBIUM The energy level of Er^{3+} is suboptimal for broadband conversion as its first step from the ground state $^4I_{15/2}$ to $^4I_{13/2}$ is already over 6500 cm^{-1} . A comparably large gap of 3000 cm^{-1} follows on the way to $^4I_{11/2}$. At around $10\,000\text{ cm}^{-1}$ it is perfectly located just above the silicon bandgap. Moreover its very good η_{PV} of 80% comprises of the main emission at 980 nm. From this the remarkable suitability for erbium-based up-conversion of monochromatic excitation at $1.54\text{ }\mu\text{m}$ is deduced. There are also further levels such as $^4F_{9/2}$ at $15\,500\text{ cm}^{-1}$ with a good η_{PV} of around 60% from the ground-state emission at 660 nm. Another is the thermally coupled $^4S_{3/2} + ^2H_{11/2}$ with an η_{PV} of 93% owing to emissions to $^4I_{15/2}$ and $^4I_{13/2}$ at 540 nm and 830 nm, respectively. Nonetheless the ladder at the beginning has too large steps for broadband, solar near-infrared excitation.

THULIUM The energy-step ladder in Tm^{3+} is comparable to that in Ho^{3+} or Er^{3+} regarding the presence of a larger initial step from 3H_6 to 3H_4 of around 5500 cm^{-1} . This is followed by an intermediate energy gap of 2200 cm^{-1} towards 3H_5 . The metastable level 3F_4 is the next excited state at little more than $12\,000\text{ cm}^{-1}$. Due to the energy gap below of 3000 cm^{-1} and sufficient radiative decay rate, it has an η_{PV} of 87% and one usable emission at 780 nm.

YTTERBIUM A large energy gap of around $10\,000\text{ cm}^{-1}$ between $^2F_{7/2}$ to $^2F_{5/2}$ is present in Yb^{3+} , which is already above the silicon bandgap. Therefore, no near-infrared light can be converted. However, in co-doped systems, Yb^{3+} is used as an emitter which is excited by energy-transfer from the up-converting donor ion, for example by erbium [177].

6.3.3 Conclusions for neodymium in glass and glass ceramics

While the criteria above are fulfilled in a sub-optimal way by Pr^{3+} , Ho^{3+} , and Tm^{3+} , good characteristics for upconversion under the above criteria are only found for Pm^{3+} , Er^{3+} , and Nd^{3+} . However, Pm^{3+} is radioactive and Er^{3+} is only applicable as an upconverter of monochromatic excitation, while broadband excitation might only be efficient in combination with a broadband absorber that transfers the energy to it [27]. This leaves Nd^{3+} as the sole ion capable of fairly efficient broadband near-infrared upconversion to light with emission wavelengths suitable for silicon absorption.

In glass and glass ceramics, the main neodymium emissions originate from the metastable $|4\rangle$ at 870 and 1050 nm. In the case of the monochromatic excitation at 800 nm, which is the fundamental upconversion mechanism, only poor conversion efficiency was found in chapter 5. A key problem there was the fact that the main emissions in this case are of Stokes-type and not entering the figure of merit for monochromatic PV upconversion, Γ_{mc} . Despite much lower excitation flux, the efficiency with regard to conversion to below 1100 nm is much better in the broadband excitation scenario as these main emissions are now fully contributing to the figure of merit for broadband PV upconversion of sunlight, Γ_{\odot} , as only near-infrared light with wavelengths

above 1100 nm is involved in the excitation processes. Whenever a neodymium ion is excited to an energy above or equal to that of its metastable state $|4\rangle$, the subsequent decay will with a large probability of around 90 % result in an emitted photon with a wavelength suitable for silicon solar cell absorption.

Another beneficial property of neodymium is the fact that it enters the BaCl_2 nanocrystals in the FCZ-c glass ceramics. This enables for even larger population storage in excited states and higher radiative decay probabilities, and hence increases both the emission in the range below 1100 nm and the probability for further ESA excitations in the first place. This is due to the fact that the absorption probability is determined by the difference in the occupation densities and thus larger for larger preoccupation of the initial level. While the branching ratios of $|4\rangle$ determine the main emissions to be at 870 and 1100 nm, upconversion especially in the neodymium-doped glass ceramics might also be suitable for different types of solar cells with bandgaps at other spectral positions, since several intense emissions exist in the visible spectral range at 660 or 590 nm, for example. Those might be suitable to photovoltaic upconversion in amorphous silicon solar cells with bandgaps at around 14300 cm^{-1} corresponding to 700 nm [19]. However, the efficiency would surely be weak as a lot of excitation energy would be lost in this case.

6.3.4 Impact of the host properties

The main arguments for rare-earth inclusion into a glass host are the easy technological manageability with respect to a crystalline upconverter. The latter is often chemically instable, mechanically fragile, susceptible to damage by UV illumination or even thermally instable. Generally, glasses are easy, quick and cheap to manufacture. The glass ceramics combine the beneficial properties of the crystals on the rare earth relaxation mechanisms with the technological advantages inherent to a glass host.

The main difference between the FCZ glass and FCZ-c glass ceramic analysed here is the emitted spectrum of the upconverted light. In the glasses most emission is just below the wavelength corresponding to the silicon bandgap, while in the glass ceramics even shorter wavelengths in the visible are generated. Some energy is lost in the glass ceramic when visible light is generated, which generates only one charge carrier as would have a lower-energy photon. Even worse, an upconverted photon in the visible probably might have cost even more near-infrared photons than a photon at 870 or 1100 nm would have. However, the mentioned storage capacity in the steady-state and hence the ESA probability are enhanced in the glass ceramic. This property over the glass matrix even excels the beforementioned disadvantage and accounts for the Γ_{\odot} in the glass ceramics, which is about a factor of five larger than in the glass above a concentration of at least 100 suns (see Fig. 6.5).

6.3.5 Optimisation of composition

As the suitability of a neodymium-doped glass-ceramic upconverter for photovoltaic applications is now motivated, it is instructive to analyse how

the different internal and external parameters are affecting its efficiency. The internal parameters are mostly the parameters inherent to the composition of the samples. Specifically, as key parameters of the system, the volume fraction of the nanocrystals and the neodymium concentration are of interest for finding the parameter space for optimal conversion efficiency.

As their impact on the occupation numbers is not independent from each other, these parameters δ and N_0 were varied and the resulting upconversion yield Γ_{\odot} determined. The result is shown in the two-dimensional graph in Fig. 6.7, from which the linkage between the parameters is apparent. Note that the variation of the actual volume fraction is substituted to the variation of the amount of neodymium entering the nanocrystals.

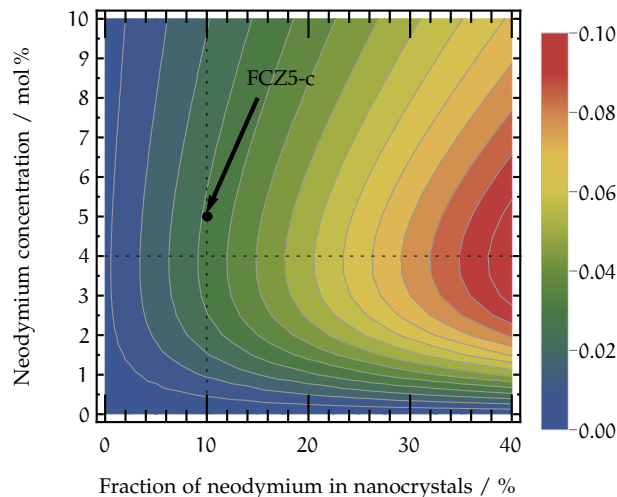
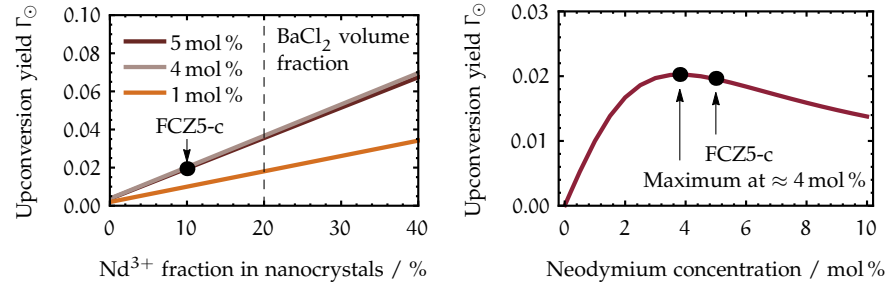


Figure 6.7: Upconversion yield from FCZ-c glass ceramic upon continuous broadband illumination with the 1000-fold near-infrared part of the solar spectrum. Along the two axis, the neodymium concentration, N_0 and the fraction of neodymium at the nanocrystals are varied. The dotted lines denote the sections along values of constant neodymium fraction and concentration shown separately in Fig. 6.8b and Fig. 6.8a, respectively.

The figure demonstrates a dramatic influence of the neodymium fraction in nanocrystals. This is expected since this fraction is profiting largely from the beneficial phonon spectrum therein. There are of course technological limits imposed to the glass preparation and a variation up until the presented 50% volume fraction is only to show the trends. It is improbable that the volume fraction can be driven so far while maintaining the remaining glass properties.

Nonetheless, from the cross section along constant neodymium dopant level (denoted by the vertical dashed line in Fig. 6.7), which is shown in Fig. 6.8a, a linear relation between neodymium fraction in nanocrystals and upconversion yield Γ_{\odot} is found. Even a small increment by 5% would already result in a 0.5% improved upconversion yield. If it were achievable to get all neodymium into the nanocrystals, a total of 1% increment of the upconversion yield would be possible. In Fig. 6.8a it is also denoted that the nanocrystal volume fraction must not be exactly equal to the neodymium fraction embedded into nanocrystals. This was already discussed in section 4.3.3. The actual fraction was found to be approximately 10% throughout the self-consistent comparison to experiments.



(a) Cuts of Fig. 6.7 along axes of different doping levels. The left black point denotes the estimated δ_{Nd} of 10% in FCZ5-c. The maximum in FCZ5-c is limited by the nanocrystal volume fraction of 20% (dashed line). (b) Cut of Fig. 6.7 along axes of constant fraction of 10% neodymium embedded into the nanocrystals. The maximum is at around 4 mol% (left point). Sample FCZ5-c is at 5 mol% (right point).

Figure 6.8: Upconversion yields Γ_{\odot} from FCZ-c upon continuous broadband illumination with the 1000-fold near-infrared of the solar spectrum. The graphs are cuts of Fig. 6.7 along axes of constant neodymium fraction in the nanocrystals (left) and constant neodymium doping levels (right).

The second cross section along constant neodymium nanocrystal fraction of 10% is shown in Fig. 6.8b. This variation of the dopant level reveals that there is an optimum concentration for maximum upconversion yield. It is at almost 4 mol% neodymium doping level. At lower levels the upconversion is inefficient since energy transfer critically depends on the doping level. At higher levels it is also becoming inefficient since the detrimental cross relaxation process stealing occupation from $|4\rangle$ becomes dominant, similar to observations in the literature [178]. The figure also shows that the doping level of the FCZ5-c sample of 5 mol% is fair but not optimal for solar broadband upconversion. For technological application the possible saving of material costs might be an important figure.

6.3.6 Optimisation of Temperature

LOW-TEMPERATURE UPCONVERSION Next to the internal, the external parameters such as the ambient temperature might be positively impacting the upconversion efficiency when steered to the right values. The temperature is related to Γ_{\odot} as it enters the energy-gap law via the relation Eq. (4.1.4) describing the temperature dependence of the phonon emission probability [140]. The expression in brackets in Eq. (4.1.4) becomes minimal when the temperature becomes minimal. To be precise, the thermal energy $k_{\text{B}}T$ must become smaller than the maximal phonon energy $\hbar\omega_{\text{max}}$ of the host. For BaCl_2 , this means $k_{\text{B}}T$ has to be further reduced from the room temperature value of approximately 205 cm^{-1} to become notably smaller than $\hbar\omega_{\text{max}} = 220 \text{ cm}^{-1}$.

To simulate low temperatures, Eq. (4.1.4) is used to convert the room temperature EGL. Furthermore, the thermal energy $k_{\text{B}}T$ enters the phonon absorption probabilities via the Boltzmann factor as shown in Eq. (4.1.5). Also, cross sections for ESA as well as the coefficients for ETU and CR are affected considerably as the strengths of spectral resonance is determined by the spectral overlap integrals. These are related strongly to the line widths.

The line widths and in particular the homogeneous contribution to the them obey an approximately quadratic temperature dependence [96, 179, 180]. For the present analysis, the temperature dependence of the line widths (in cm^{-1}) in neodymium-doped phosphate glass were taken as an estimate from Ref. [96], where

$$\Delta k_{\text{hom}}(T) \approx 1.637 \cdot 10^{-3} T^{1.863}$$

is given. The inhomogeneous contribution to the line widths was taken as constant over the temperature [179]. With these temperature dependent line widths, all related parameters were reevaluated for the broadband solar NIR excitation simulation over a temperature range of 0 to 300 K. The results that have to be treated as a prediction of the qualitative trends are graphically shown in Fig. 6.9 for a solar concentration factor of 1000.

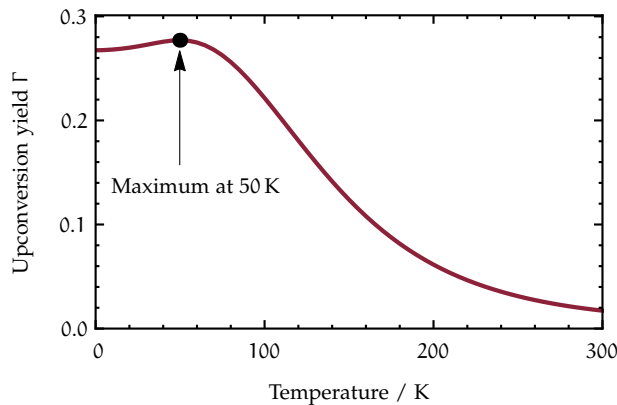


Figure 6.9: Trend of the temperature dependence of upconversion yield for FCZ-c glass ceramic upon solar near-infrared pump light from 1000 suns.

While the numbers from the figure should not be taken as exact, the huge influence of the phonon availability becomes apparent. Starting from liquid nitrogen temperature downwards, a dramatic increase in the upconversion efficiency is observed. Due to the reduced phonon mobility, the radiative decay channels become the dominant relaxation channels and hence, the emission is increased remarkably. Upon further cooling, the efficiency is dropping again as the increasingly narrow line widths become detrimental to the resonance conditions for several upconversion transitions from ESA and ETU. Furthermore, the thermal population of the lower levels, connected to the reduced phonon availability, also affects the upconversion probabilities.

LIMITS OF THE MODEL The actual accuracy of the simulation result from Fig. 6.9 is uncertain, given the fact that several drastic simplifications were made in order not to complicate the model too far. For example, the line width reduction upon temperature decrease was considered, but only for the amorphous part of the matrix, despite the fact that the situation will be considerably more complex in a glass ceramic. Furthermore, the positions of the spectral lines will change at low temperatures [95] with a possible impact on resonance conditions. This was not considered in this very simple model as was not the slight temperature dependence of the α parameter in the EGL equation Eq. (4.1.1) [149, 162]. Also, the temperature dependence of the ion-ion interactions is suspected to be significant, but was disregarded

here, as ESA is probably the dominant upconversion mechanism. Note that reduced ion-ion interaction probabilities also reduce the probability for concentration quenching by CR. Another important aspect is that the common A_{SPE} of level groups as they were calculated in section 3.2.3 will be strongly depending on temperature [100]. At the same time, the individual Einstein coefficients of isolated levels remain unchanged upon temperature changes [109]. Furthermore the assumption of equally populated ground state M_J levels, as presumed in the derivation of the JO theory, is not anymore valid at low temperatures [122], with unknown impact on the Einstein coefficients.

Nonetheless, experiments in Ref. [155] showed a transition from $\eta = 0.4$ to $\eta = 1.0$ upon the temperature reduction from room temperature to 140 K for the erbium transition $|^4S_{3/2} + ^2H_{11/2}\rangle \rightarrow |^4I_{15/2}\rangle$ in tellurite glass. This is a similarly drastic efficiency improvement upon cooling although the experiment describes a much simpler case of population dynamics as the model presented here.

Summing up, Fig. 6.9 is reflecting the expected trend towards very good quantum efficiencies of individual emission processes regardless of the energy gap below the emitting level.

CONCLUSION The temperature-dependence was only roughly implemented into the model by considering the effect of the phonon mobility change on the energy-gap laws. Although more sophisticated modifications to the room temperature model were disregarded in favor of a very simple model description, the trend towards dramatically increased upconversion yields at low temperatures is correctly obtained. However, the numbers in Fig. 6.9 should not be perceived accurate.

Regarding the photovoltaic application of the upconverter as a bottom layer in silicon solar cells, it is clear that the necessity for additional cooling would be quite a disadvantageous requirement for a cost-effective solar cell device, an application in areas of low temperatures might be an intriguing perspective. For example, application of photovoltaics in space was already presented in the literature [181, 182]. Inversely, the strong dependency of photoluminescent characteristics on the temperature might as well be exploited in sensors for monitoring ambient temperature.

6.4 SUMMARY

Based on the upconversion description self-consistently established in the previous chapters, the model was extended to continuous illumination with a broadband excitation source. Introducing the spectral region above 1100 nm from the subaerial solar spectrum, it was simulated how the neodymium-doped glasses and glass ceramics were converting the near-infrared photon flux from the sun to photons at wavelengths below 1100 nm. Embedded into a bottom layer under a bifacial solar cell, neodymium thus enables for a conversion of the otherwise lost sub-bandgap photons to the wavelengths finally absorbable by the silicon cell.

The special structure of the neodymium energy level system features low-energy steps in the first excited states and a spectral position of the metastable level just so to efficiently emit above-bandgap photons. Fostered by the numerous quasi-resonances achieved with the help of the huge line widths in the amorphous host matrix, the stationary neodymium ions exhibit multiple overlapping transitions at wavelengths above 1100 nm. In contrast to upconverting rare-earths limited to monochromatic, narrow-band upconversion such as erbium, neodymium ions in the stationary state following continuous excitation are thus able to absorb a broad range of the near-infrared part of the solar spectrum.

It must however be stressed that the results obtained are based solely on the simulation method established in the previous chapters. Experiments recording the upconverted photon flux with respect to the input flux are mandatory to proof the correctness of the model description presented here.

7

SUMMARY

Two goals were set for this work in section 1.1:

1. Motivated by the emission enhancement of neodymium-doped FCZ glass upon the growth of BaCl₂ nanocrystals therein, a model was to be developed that describes the excitation dynamics in order to determine the reason for this remarkable effect. The model had to include descriptions for both the Stokes-type photoluminescence and the Anti-Stokes-type upconversion luminescence.
2. An photovoltaic upconverting bottom layer for a bifacial silicon solar cell based on neodymium-doped glass or glass ceramic was to be analysed concerning its feasibility for enhancing silicon photovoltaics. Venues for advance material optimisation were to be evaluated.

FIRST AIM

For the description of neodymium in FCZ glasses, a rate equation system was developed that considers incident radiation in terms of ground and excited state absorption processes. The generation of photoluminescence (PL) from spontaneous emission as well as nonradiative loss mechanisms due to interactions with the matrix or with other ions were implemented. As the latter become insignificant at larger interionic distances accompanied by low concentrations, the model was initially focused on the description of weakly doped glasses without nanocrystals. The radiative decay rates (Einstein coefficients) were determined from a Judd–Ofelt analysis. They are of the order of 10^2 to 10^4 s⁻¹, depending on the transition.

Several dynamic mechanisms were excited in selective experiments and their decays monitored with time-resolved PL spectroscopy. The simulation results were found to be in good agreement with the data. From the analysis it was apparent that the multiphonon relaxation (MPR) rates in the glasses are of the order of 10^6 to 10^{11} s⁻¹, depending on the energy gap, and hence 2 to 7 orders of magnitude larger than the radiative decay rates. Thus, MPR is found to be the dominant decay mechanism in the glasses. As a consequence, a significant alteration of the dynamics is anticipated for the fraction of neodymium being enclosed by the nanocrystals.

In order to extend the description to this composite glass-ceramic matrix, an effective medium description was introduced. The resulting model was again successfully verified with selective time-resolved PL spectroscopy. The nanocrystals even enabled emissions from higher lying levels that are otherwise not seen in glasses. The increased intensity was accompanied by a corresponding strong reduction in the PL lifetimes in perfect agreement to the expectation of reduced MPR rates for the part of neodymium subject to the nanocrystalline phonon spectrum.

One notable exception is the level $|4\rangle$, which, due to its remarkable energy gap toward $|3\rangle$, decays only radiatively. As a consequence of its long-livedness (lifetime of around $400\ \mu\text{s}$), nearly the whole excited population is finally accumulating in this state on time scales of the order of $1/(\text{rate of MPR})$. Therefore this state is metastable, which is why it is serving as the starting point for upconversion processes that enable for a further excitation of ions already in an excited state.

For an experimental verification of the correct description of upconversion the power dependence of Anti-Stokes luminescence spectra upon monochromatic pumping was analysed. Therefore the focus was now set on the highly doped samples. A fair agreement between the experimental and simulated upconversion could be found in stationary and pulsed excitation scheme. It was concluded from the simulation that monochromatic upconversion of $805\ \text{nm}$ pump light with neodymium in the present samples is not very efficient. Upconversion yields of $2.5 \cdot 10^{-6}$ to $6.6 \cdot 10^{-6}$ at $85\ \text{mW}$ for the glass and the glass ceramic were determined, respectively. Nonetheless, with the self-consistent model extension accompanied to the continuous experimental verification of the respective parameters, the first aim was reached.

SECOND AIM

Proceeding further, the similar spacing between the first three excited states of neodymium and the position of the metastable level were identified as optimal prerequisites for an application of such a glass or glass ceramic as an upconverting bottom layer below a bifacial silicon solar cell. The low-step energy level ladder that extends further to higher levels of neodymium enables for multiple excitations over a broad range of photon energies present in the solar near infrared spectrum. This property is fostered by the huge line widths caused by the amorphous host matrix. As the metastable level is the main emitter, the excitation energy of at least two near-infrared photons with subbandgap wavelengths $>1100\ \text{nm}$ are converted to its main emissions at 870 and $1050\ \text{nm}$ that are just above the silicon bandgap and contribute to the generation of charge carriers in silicon. From a comparison with the other rare earth ions it turned out that although the upconversion coefficients are larger in other ions, neodymium might be the only rare earth ion able to absorb over broad bands of the solar spectrum.

A requirement for this is sufficient storage capacity in the stationary state defined by the probabilities of nonradiative deexcitation channels, mainly MPR. The storage capacity in ZBLAN-based glasses is already such that thermal occupation in the lower levels is accumulating enough to make them initial levels of efficient next excitation steps. This is improved even further in the glass ceramics by the even lower maximal phonon energies.

Within the framework of the second aim the established model was extended to broadband excitation with light from the solar spectrum. This was accomplished in analogy to the already present Anti-Stokes mechanisms and under exploitation of the multiple resonant or quasi-resonant ESA processes possible in the energy level. The unused light passing a silicon solar cell was used in concentrated form as the pump light. At a reasonable solar concentration of 1000, efficiencies of 0.4 and 2% upconverted photon

flux (<1100 nm) per near-infrared flux (>1100 nm) were generated. These comparably good figures are possible due to the electronic structure of neodymium. In contrast to erbium with only 3 levels participating in the thus monochromatic upconversion step, neodymium can be excited by several combinations of different photon energies.

The simulation tool was further used to determine the influence of the material and environmental parameters. It was found that the efficiency of the converter might be further increased if it becomes possible to get more neodymium into the nanocrystals without negatively affecting the optical properties of the system. Furthermore it turned out that, contrary to erbium, where the upconversion efficiency increases up to at least 10 mol % doping level, neodymium shows an efficiency maximum at the lower concentration of 4 mol %, where the optimal balance between the energy transfer and the detrimental cross relaxation processes is present. This should be taken into account to optimise the spending of materials.

In another, strongly simplifying simulation the influence of the ambient temperature was analysed. Due to the strong dependency of the phonon emission probability on the temperature, phonon-based loss channels are minimized. This leads to a strong increase in efficiency upon cooling. However, the effect is compensated at temperatures below 100 K by the reduction of the initial thermal population and the fact that the ESA-spectrum of the stationary neodymium is continuously bleaching out. The reason lies in the reduction of the homogeneous line widths leading to reduced efficiency of the broadband absorption.

However, one remark should not go unnoticed. Looking at the good conversion results at 1000-fold concentrated solar excitation it is nonetheless clear that such intense pumping would introduce around $1000 \times 180 \text{ W/m}^2$ into the sample, from which the major part is naturally converted to heat. Therefore, a real-world upconverter will probably become rather inefficient or might even become damaged as its temperature rises. It would hence appear that such a system is only realistic in a cooled environment, for example attached to solar cells in space. Regardless of this practical limitation, the two aims of the work were fulfilled.

OUTLOOK

As soon as experiments verify the good conversion results of broadband near-infrared sunlight, the already discussed application in photovoltaics should be tested in detail. This requires building a prototype of a bifacial solar cell with an upconverting bottom layer between cell and back-reflector. The real-world performance will then be accessible by measuring the generated shortcut current under concentrated sunlight in comparison to that generated from a cell without the upconverter.

Towards optimal performance, the system could be engineered further by the manipulation of other parameters. As the rate equation model is implemented as a computer program and equipped with a graphical user interface, the conversion figures of other rare earth ions or the performance of neodymium in other host matrices can be easily implemented by adjusting the appropriate parameter sets.

A

DETAILS

A.1 EQUATION SYSTEM

The general form of the differential equation system is given in the following for the simulation of monochromatic excitation.

$$\begin{aligned}\partial_t N_1 &= -W_{PE,1}N_1 + W_{PE,2}N_2 + W_{PA,1}N_0 - W_{PA,2}N_1 \\ &\quad - A_{SPE,1}N_1 + \sum_{i=2}^{15} A_{SPE,i}\beta_{i,1}N_i \\ &\quad + w_{ETU3a} \left(N_4^2 - N_1N_{12} \right) + w_{ETU3b} \left(N_4^2 - N_1N_{13} \right) \\ \partial_t N_2 &= -W_{PE,2}N_2 + W_{PE,3}N_3 + W_{PA,2}N_1 - W_{PA,3}N_2 \\ &\quad - A_{SPE,2}N_2 + \sum_{i=3}^{15} A_{SPE,i}\beta_{i,2}N_i \\ &\quad + w_{ETU2a} \left(N_4^2 - N_{10}N_2 \right) + w_{ETU2b} \left(N_4^2 - N_{11}N_2 \right) \\ \partial_t N_3 &= -W_{PE,3}N_3 + W_{PE,4}N_4 + W_{PA,3}N_2 - W_{PA,4}N_3 \\ &\quad - A_{SPE,3}N_3 + \sum_{i=4}^{15} A_{SPE,i}\beta_{i,3}N_i \\ &\quad + w_{ETU1} \left(N_4^2 - N_3N_9 \right) \\ &\quad + 2w_{CR} \left(N_0N_4 - N_3^2 \right) \\ \partial_t N_4 &= -W_{PE,4}N_4 + W_{PE,5}N_5 + W_{PA,4}N_3 - W_{PA,5}N_4 \\ &\quad - A_{SPE,4}N_4 + \sum_{i=5}^{15} A_{SPE,i}\beta_{i,4}N_i \\ &\quad - \xi\rho_0 e^{(-t/\tau_0)^2} \sigma_{ESA} (N_4 - N_{15}) \\ &\quad - w_{CR} \left(N_0N_4 - N_3^2 \right) \\ &\quad - 2w_{ETU1} \left(N_4^2 - N_3N_9 \right) \\ &\quad - 2 \left(w_{ETU3a} \left(N_4^2 - N_1N_{12} \right) + w_{ETU3b} \left(N_4^2 - N_1N_{13} \right) \right) \\ &\quad - 2 \left(w_{ETU4a} \left(N_4^2 - N_0N_{14} \right) + w_{ETU4b} \left(N_4^2 - N_0N_{15} \right) \right) \\ &\quad - 2 \left(w_{ETU2a} \left(N_4^2 - N_{10}N_2 \right) + w_{ETU2b} \left(N_4^2 - N_{11}N_2 \right) \right)\end{aligned}$$

$$\begin{aligned}
\partial_t N_5 &= + (1 - \xi) \rho_0 e^{(-t/\tau_0)^2} \sigma_{GSA} (N_0 - N_5) \\
&\quad - W_{PE,5} N_5 + W_{PE,6} N_6 + W_{PA,5} N_4 - W_{PA,6} N_5 \\
&\quad - A_{SPE,5} N_5 + \sum_{i=6}^{15} A_{SPE,i} \beta_{i,5} N_i \\
\partial_t N_6 &= - W_{PE,6} N_6 + W_{PE,7} N_7 + N_5 W_{PA,6} - W_{PA,7} N_6 \\
&\quad - A_{SPE,6} N_6 + \sum_{i=7}^{15} A_{SPE,i} \beta_{i,6} N_i \\
\partial_t N_7 &= - W_{PE,7} N_7 + W_{PE,8} N_8 + N_6 W_{PA,7} - W_{PA,8} N_7 \\
&\quad - A_{SPE,7} N_7 + \sum_{i=8}^{15} A_{SPE,i} \beta_{i,7} N_i \\
\partial_t N_8 &= - W_{PE,8} N_8 + W_{PE,9} N_9 + N_7 W_{PA,8} - W_{PA,9} N_8 \\
&\quad - A_{SPE,8} N_8 + \sum_{i=9}^{15} A_{SPE,i} \beta_{i,8} N_i \\
\partial_t N_9 &= - W_{PE,9} N_9 + W_{PE,10} N_{10} + W_{PA,9} N_8 - W_{PA,10} N_9 \\
&\quad - A_{SPE,9} N_9 + \sum_{i=10}^{15} A_{SPE,i} \beta_{i,9} N_i \\
&\quad + w_{ETU1} (N_4^2 - N_3 N_9) \\
\partial_t N_{10} &= - W_{PE,10} N_{10} + W_{PE,11} N_{11} + W_{PA,10} N_9 - W_{PA,11} N_{10} \\
&\quad - A_{SPE,10} N_{10} + \sum_{i=11}^{15} A_{SPE,i} \beta_{i,10} N_i \\
&\quad + w_{ETU2a} (N_4^2 - N_{10} N_2) \\
\partial_t N_{11} &= - W_{PE,11} N_{11} + W_{PE,12} N_{12} + W_{PA,11} N_{10} - W_{PA,12} N_{11} \\
&\quad - A_{SPE,11} N_{11} + \sum_{i=12}^{15} A_{SPE,i} \beta_{i,11} N_i \\
&\quad + w_{ETU2b} (N_4^2 - N_{11} N_2) \\
\partial_t N_{12} &= - W_{PE,12} N_{12} + W_{PE,13} N_{13} + W_{PA,12} N_{11} - W_{PA,13} N_{12} \\
&\quad - A_{SPE,12} N_{12} + \sum_{i=13}^{15} A_{SPE,i} \beta_{i,12} N_i \\
&\quad + w_{ETU3a} (N_4^2 - N_1 N_{12}) \\
\partial_t N_{13} &= - W_{PE,13} N_{13} + W_{PE,14} N_{14} + W_{PA,13} N_{12} - W_{PA,14} N_{13} \\
&\quad - A_{SPE,13} N_{13} + \sum_{i=14}^{15} A_{SPE,i} \beta_{i,13} N_i \\
&\quad + w_{ETU3b} (N_4^2 - N_1 N_{13}) \\
\partial_t N_{14} &= - W_{PE,14} N_{14} + W_{PE,15} N_{15} + W_{PA,14} N_{13} - W_{PA,15} N_{14} \\
&\quad - A_{SPE,14} N_{14} + A_{SPE,15} \beta_{15,14} N_{15} \\
&\quad + w_{ETU4a} (N_4^2 - N_0 N_{14})
\end{aligned}$$

$$\begin{aligned}
\partial_t N_{15} = & -W_{PE,15} N_{15} + W_{PA,15} N_{14} \\
& -A_{SPE,15} N_{15} \\
& + \xi_{\rho_0} e^{(-t/\tau_0)^2} \sigma_{ESA} (N_4 - N_{15}) \\
& + w_{ETU4b} \left(N_4^2 - N_0 N_{15} \right)
\end{aligned}$$

The equations shown here do not fully represent the exact equation set used for each of the simulations and were modified accordingly throughout the process of self-consistently establishing the model and coefficients. For the stationary state, the $\partial_t N_j$ are set to zero and the time-dependent exponentials in the GSA and ESA terms are set to unity. The time-dependencies of the $N_j = N_j(t)$ are implicitly presumed. In general, they are also dependant on the spatial coordinates (r, z) .

A.2 LASER PARAMETERS

A.2.1 Determination of beam waists from beam profiling

The determination of the optical intensity $I(r, z)$ involves the precise measurement of the beam waist w_0 as it enters $I(r, z)$ quadratically. This was accomplished by beam profiling at the sample holder site in the photoluminescence (PL) setup. The individual graphs in Fig. A.1 show example beam profiles measured for beams from the different excitation sources: the direct second-harmonic (SHG) from the fs laser (Fig. A.1a), the signal beam from the optical parametric amplifier (OPA) itself pumped by the fs laser (Fig. A.1b), and the cw laser diode (Fig. A.1c). In Fig. A.1d it is shown how fitting Gaussian functions to the cuts along horizontal and vertical directions through the beam center yields the respective beam waist.

The figures demonstrate that the SHG beam has the best Gaussian shape. Deviations occur for the OPA signal as several nonlinear optical conversion steps distributed over several metres of beam path are involved therein. The largest deviation from the Gaussian shape is however found for the cw laser diode. The asymmetric shape of the emitter leads to asymmetric emission, which exhibits an inherent asymmetric diffraction of the beam. This is fostered by the fact that thermal load is also asymmetrically distributed over the emitter and leads to a different beam shape via the temperature dependence of the refractive index $\partial_T n$. The result is a Gaussian beam with respect to the horizontal and vertical direction, but without radial symmetry (elliptical beam). Also, horizontal and vertical direction may have different foci and focal positions.

A.2.2 Pulse durations: FROG

The pulse durations of the fs excitation source were measured using the Frequency Resolved Optical Gating (FROG) technique [183, 184] of the SHG

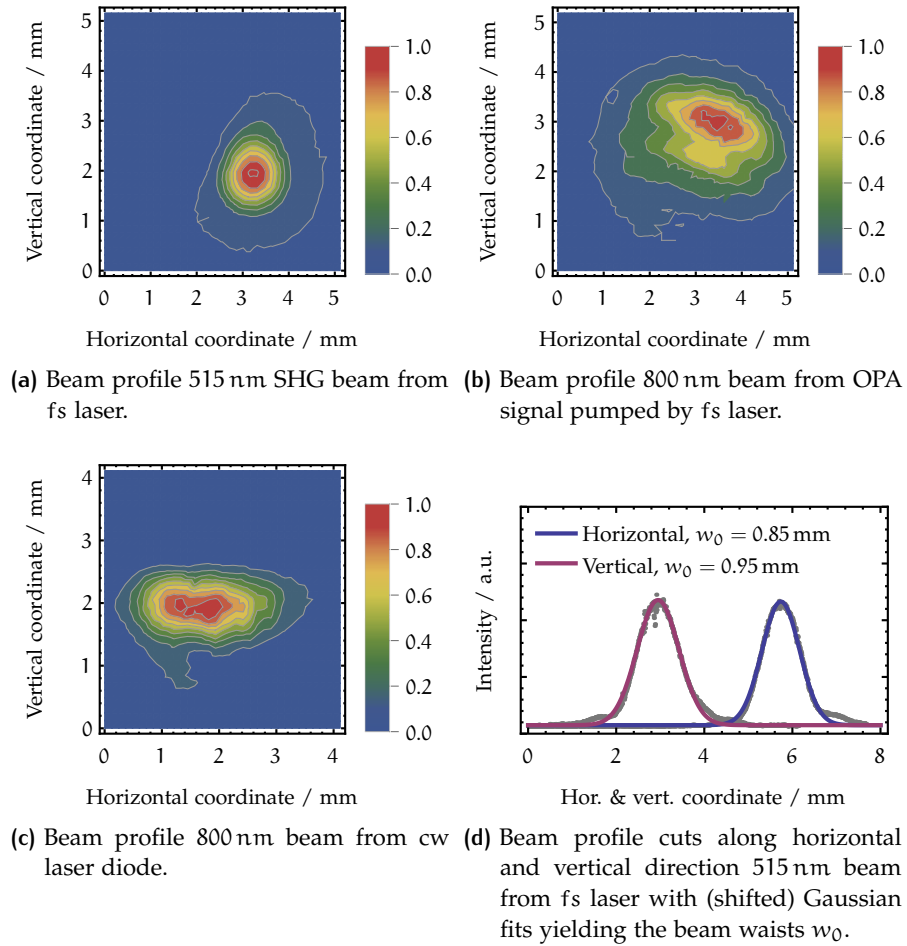


Figure A.1: Beam profiles of laser sources.

type. The SHG-FROG technique is very similar to an autocorrelation of a fs pulse with itself. However, the SHG intensity, measured with respect to the delay between two pulses, is detected with a spectrometer. From the additional data, which exhibits several redundancies, all pulse characteristics can be deduced with phase-retrieval algorithms. In contrast to autocorrelation, this also includes the pulse phase and does not impose any prerequisites on the pulse.

Fig. A.2 shows the experimental FROG traces from the fs laser fundamental and SHG beam, as well as from the signal beam that was further converted in the optical parametric amplifier. The latter represents for all excitation wavelengths between 650 to 1000 nm, as all of them were generated from the signal beam that does not change much over this range. Figure A.2d additionally shows the normalised electric field of the signal beam after phase-retrieval. A Gaussian fit is shown for comparison. The pulse durations were determined to be 190.0 fs for the fundamental, 186.5 nm for the SHG, and 165.4 fs for the signal pulses.

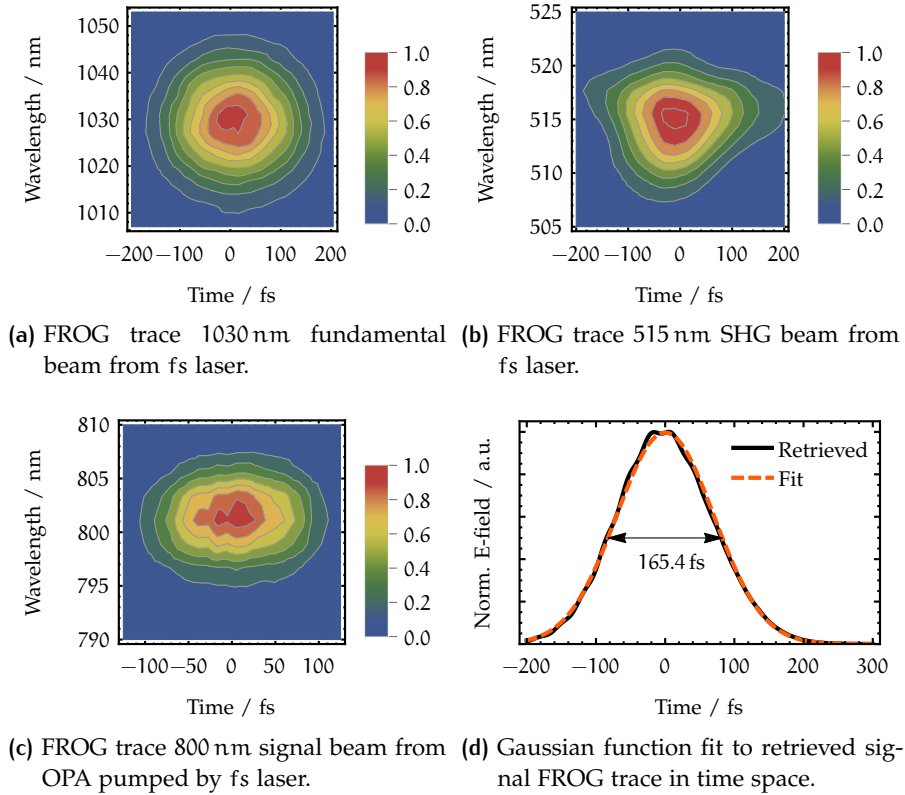


Figure A.2: FROG traces of laser sources.

A.2.3 Control of repetition rate with frequency division

The repetition rate of the fs laser was arbitrarily chosen by controlling the output Pockels cell of the regenerative amplifier such that a defined number of pulses may exit as a pulse packet. The frequency of the pulse packets is arbitrary as long as it is below the inherent laser frequency of the amplification stage. The main part of this frequency division system is the computer program, controlling several counter channels on a *National Instruments* multifunction computer extension card.¹ The main part of the computer program is shown in listing A.1. A brief description of the work flow is given here. Details on the driver functions of the *DAQmx* driver library are given in its documentation.²

Listing A.1: C code for the initialisation of the frequency division with *NI-DAQmx*.

```
char chan[256] = "Dev1/ctro"; // output (A)
char chan_int_out[256] = "/Dev1/Ctr1InternalOutput";
char chan2[256] = "Dev1/ctr1"; // output (B)
char triggerSource[256] = "/Dev1/PFI8"; // start trigger
TaskHandle thLaserCounter = 0;
TaskHandle thLaserCounter2 = 0;

int fnConfSimRR() {
    double duty, initdelay, newf, freq;
    int divider_ticks, error;
```

¹ It is a *NI PCIE-6341-X* connected to the laser over BNC wires at an *BNC-2110* connector.

² *NI-DAQmx* in version 9.6.2 was used from within *NI LabWindows/CVI 2010, SP1*.

```

// Config
newf = 100; // target rate of pulse packets in Hz
freq = 1000; // base rate (rate within a packet)
divider_ticks = RoundRealToNearestInteger(freq/newf);

// Create counter A.
DAQmxCreateTask("", &thLaserCounter);
DAQmxCreateCOPulseChanTicks(thLaserCounter, chan2, "",
    triggerSource, DAQmx_Val_Low, 0, divider_ticks,
    divider_ticks);
DAQmxSetExportedSignalAttribute(thLaserCounter,
    DAQmx_Exported_CtrOutEvent_OutputBehavior, DAQmx_Val_Pulse
);
DAQmxCfgImplicitTiming(thLaserCounter, DAQmx_Val_ContSamps,
    1000);

// Create Counter B.
DAQmxCreateTask("", &thLaserCounter2);
initdelay = 0;
duty = 0.01;
DAQmxCreateCOPulseChanFreq(thLaserCounter2, chan, "",
    DAQmx_Val_Hz, DAQmx_Val_Low, initdelay, newf, duty);
DAQmxCfgDigEdgeStartTrig(thLaserCounter2, chan_int_out,
    DAQmx_Val_Rising);
DAQmxSetStartTrigRetriggerable(thLaserCounter2, TRUE);

return 0;
}

```

Counter (A) is synced to the laser clock (sync) and outputs pulses any `divider_ticks` input pulses (ratio between `freq` and `newf`). This effectively divides the laser frequency. It is set to behave in pulsed form as opposed to toggle behavior and thus `lowticks = highticks = divider_ticks` only generates `divider_ticks` output pulses instead of twice that. Counter (A) is either run continuously (laser permanently on) or with a finite set of samples (`fnLaserPulse`). Its internal output triggers (B) who gives the final output to the shutter.

Counter (B) is a single pulse (no timing specified), retriggerable counter output channel that outputs a pulse with respect to (A). Its output is connected to the pulsepicker input of the laser and opens the Pockels cell accordingly.

A.3 THEORETICAL DETAILS

A.3.1 Metastable level branching ratios

Table A.1 shows the branching ratios β_{ij} for transitions starting from the metastable level ($i = 4$) in dependence of the thermal treatment step. The

data was also published separately along with all other branching ratios from the Judd-Ofelt analysis [112].

Table A.1: Branching ratios for transitions starting from the metastable level |4) in dependence of the thermal treatment step.

sample	$\beta_{4,3}$	$\beta_{4,2}$	$\beta_{4,1}$	$\beta_{4,0}$
FZ	0.01	0.10	0.48	0.41
FCZ	0.00	0.08	0.44	0.47
FCZ-c, 240 °C	0.00	0.08	0.44	0.48
FCZ-c, 250 °C	0.00	0.08	0.43	0.48
FCZ-c, 260 °C	0.00	0.07	0.41	0.51
FCZ-c, 270 °C	0.00	0.07	0.40	0.53

A.3.2 Conversion of electric signals to experimental photon flux

Figure A.3 gives an overview over the conversion steps. The description starts with the photon generation in the sample for clarity, whereas the conversion steps are carried out in the reverse order starting with the PMT signal.

First of all, the photons generated in the sample are collected by a parabolic mirror, which naturally captures only a limited solid-angle $d\Omega$ from the isotropically emitted PL light. With the mirror parameters, the full signal can however be calculated.

The equation for the isosceles triangle between the mirror edges and the sample position,

$$(2w_0)^2 = 2r^2(1 - c_\gamma),$$

where $2w_0$ is the beam diameter, gives the aperture angle. It is further $r^2 = f^2 - w_0^2$ with f the focal length of the mirror. Inserting the equations into each other gives c_γ . The solid angle follows as

$$\Omega = 4\pi \sin^2 \frac{\omega}{2},$$

where $\omega = \arccos c_\gamma$. Using $f = 30$ cm and $2w_0 = 2.8$ cm gives the intensity fraction passing the solid angle with respect to the total 4π distribution as approximately $2 \cdot 10^3$.

From the photon flux, the power density $H = \Phi \times h\nu$ is available. Reflection losses at all intermediate mirrors, as well as losses from the involved filters and the sample surface need to be considered as wavelength dependent transmission factors. The losses through the monochromator slits can then be estimated. Consider the Gaussian intensity distribution (from Eq. (4.1.7)) generated by the laser pump beam in cartesian coordinates,

$$I(x, y, z) = I_0 \frac{w_0}{w(z)} \exp\left(-2 \frac{x^2 + y^2}{w^2(z)}\right).$$

Integrating it over the slit plane (y between $-\zeta$ and ζ with 2ζ the slitwidth) and normalising it with the integral over \mathbb{R}_2 gives the transmission through the slit. The result is the Gaussian error function, $\text{erf}(\sqrt{2}\zeta/w_0)$. With a

slitwidth of 300 μm , a total of 2% of a 2.5 cm wide detection beam is transmitted into the monochromator.

After application of the grating efficiency curve (between approximately 20 and 70%) to deal with its spectral dependencies, multiplication with the detector area (10 mm \times 10 mm) and insertion of the PMT sensitivity curve factors (between approximately 10^1 and 10^2) and PMT gain factor (around $5 \cdot 10^5$ at 1.5 kV) finally gives the PMT signal in detector units.

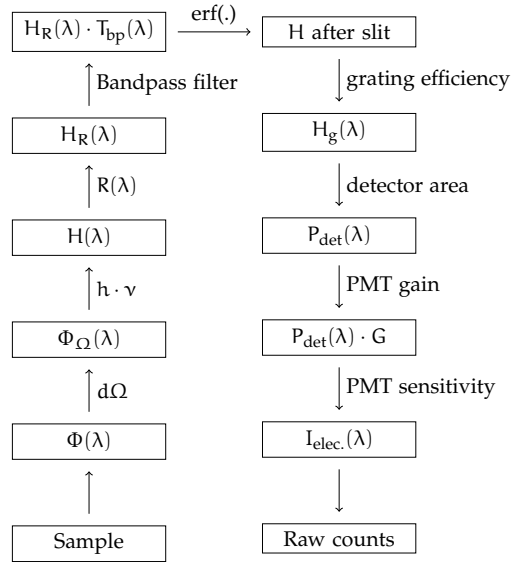


Figure A.3: Conversion steps involved for the determination of the experimental spectral photon flux from the electric signals of the detection apparatus in Fig. 2.8.

A.4 ERROR ESTIMATION

A.4.1 Significance of errors in volume fraction for Rayleigh scattering size determination

At the time of this writing there is no detailed value for the actual volume fraction of BaCl_2 crystals within the differently heat treated samples available. There is only the assumption that due to the amount of added chemical constituents there can only be less than or equal to 20% crystalline BaCl_2 . On the other hand, Ref. [7] estimates a volume fraction of 20% from transmission electron microscopy measurements (TEM) for similar samples, but with unknown accuracy. Therefore, the volume fraction estimation as used in the Rayleigh scattering analysis in section 2.4.1 is based on slightly vague assumptions.

Nonetheless, an estimation of the significance of possible errors in the volume fraction can be made. Following Eq. (2.4.5), the volume fraction δ_i enters the extinction coefficient α_{Rayleigh} as in

$$\alpha_{\text{Rayleigh}} \propto \delta_i (1 - \delta_i) d^3 .$$

If an error, namely $\Delta\delta_i$, is introduced, this gives

$$\frac{\alpha_{\text{Rayleigh}}}{d^3} \propto \delta_i(1 - \delta_i) + \Delta\delta_i(1 - \Delta\delta_i - 2\delta_i).$$

For $\Delta\delta_i < \delta_i$ one can neglect $\Delta\delta_i^2$ and assuming δ_i to be roughly 0.2 one can write

$$d^3 \propto \frac{\alpha_{\text{Rayleigh}}}{(0.2 + \Delta\delta_i)(0.8 - \Delta\delta_i)} \approx \frac{\frac{\alpha_{\text{Rayleigh}}}{0.16}}{1 + \frac{0.6}{0.16}\Delta\delta_i}.$$

With $\sqrt[3]{1 + \Delta\delta_i} \approx 1 + \frac{\Delta\delta_i}{3}$ and the geometric series one obtains a measure for the influence of errors in δ_i for errors in d

$$d \propto \sqrt[3]{\frac{\alpha_{\text{Rayleigh}}}{0.16}} \left(1 - \frac{0.6\Delta\delta_i}{3 \cdot 0.16}\right). \quad (\text{A.4.1})$$

$\Delta\delta_i \rightarrow 0$ yields the expected case for no error in d . With Eq. (A.4.1) errors for d can be calculated, some of which have been listed in Table A.2. For particle

Table A.2: Calculations of the error in the particle size d under the assumption of erroneous estimation of the volume fraction δ_i .

Significance of errors in δ_i	
$(\Delta\delta_i/d)/\%$	$(\Delta d/d)/\%$
75	19
50	13
40	10
30	8
20	5
10	3
5	1

sizes of for example 25 nm this means an error of 50 % in δ_i . This is $\delta_i = 0.3$ instead of 0.2. Thus, there will be a misdetermination of d to yield 28 nm, very much in the expected margin of error of this method, where the main error comes from the fit quality, measurement calibration and corrections. That means that the errors introduced by a slightly off volume fraction are not significant for the size determination. Hence, a rough estimation of δ_i suffices for this purpose.

BIBLIOGRAPHY

- [1] B. Bendow, M. G. Drexhage and H. G. Lipson, *J. Appl. Phys.* **52**, 1460 (1981) [10.1063/1.329781](#).
- [2] B. Bendow, P. K. Banerjee, M. G. Drexhage, J. Goltman, S. S. Mitra and C. T. Moynihan, *J. Am. Ceram. Soc.* **65**, C8 (1982) [10.1111/j.1151-2916.1982.tb09929.x](#).
- [3] S. Aasland, M.-A. Einarsrud, T. Grande and P. F. McMillan, *J. Phys. Chem.* **100**, 5457 (1996) [10.1021/jp952866a](#).
- [4] I. D. Aggarwal and G. Lu, *Fluoride Glass Fibre Optics* (Academic Press, London, UK, 1991), [10.1002/adma.19920041019](#).
- [5] M. Poulain, M. Poulain and J. Lucas, *Materials Research Bulletin* **10**, 243 (1975) [10.1016/0025-5408\(75\)90106-3](#).
- [6] C. Pfau, U. Skrzypczak, M. Miclea, C. Bohley, P.-T. Miclea and S. Schweizer, *MRS Proc.* **1404** (2012) [10.1557/opl.2012.502](#).
- [7] B. Ahrens, P. Löper, J. C. Goldschmidt, S. Glunz, B. Henke, P.-T. Miclea and S. Schweizer, *Phys. Status Solidi A* **205**, 2822 (2008) [10.1002/pssa.200880452](#).
- [8] U. Skrzypczak, M. Miclea, A. Stalmashonak, B. Ahrens, B. Henke, G. Seifert, J. A. Johnson and S. Schweizer, *Phys. Status Solidi C* **8**, 2649 (2011) [10.1002/pssc.201084131](#).
- [9] M. Shojiya, M. Takahashi, R. Kanno, Y. Kawamoto and K. Kadono, *Appl. Phys. Lett.* **72**, 882 (1998) [10.1063/1.120924](#).
- [10] B. Ahrens, C. Eisenschmidt, J. A. Johnson, P. T. Miclea and S. Schweizer, *Appl. Phys. Lett.* **92**, 061905 (2008) [10.1063/1.2837542](#).
- [11] B. Ahrens, "Down- and Up-Conversion in Fluorozirconate-Based Glasses and Glass Ceramics for Photovoltaic Application", PhD thesis (University Paderborn, Germany, 2009).
- [12] C. Pfau, C. Bohley, P.-T. Miclea and S. Schweizer, *J. Appl. Phys.* **109**, 083545 (2011) [10.1063/1.3580281](#).
- [13] C. Bohley, J.-M. Wagner, C. Pfau, P.-T. Miclea and S. Schweizer, *Phys. Rev. B* **83**, 024107 (2011) [10.1103/PhysRevB.83.024107](#).
- [14] B. Henke, F. Pientka, J. A. Johnson, B. Ahrens, P.-T. Miclea and S. Schweizer, *J. Phys.: Condens. Matter* **22**, 155107 (2010) [10.1088/0953-8984/22/15/155107](#).
- [15] B. Henke, B. Ahrens, J. A. Johnson, P.-T. Miclea and S. Schweizer, *Proc. SPIE* **7411**, 74110E (2009) [10.1117/12.825275](#).
- [16] B. Henke, B. Ahrens, P.-T. Miclea, C. Eisenschmidt, J. A. Johnson and S. Schweizer, *J. Non-Cryst. Solids* **355**, 1916 (2009) [10.1016/j.jnoncrysol.2009.04.050](#).
- [17] G. Soundararajan, C. Koughia, A. Edgar, C. Varoy and S. Kasap, *J. Non-Cryst. Solids* **357**, 2475 (2011) [10.1016/j.jnoncrysol.2010.11.053](#).

- [18] M. A. Green, *Solar Cells; Operating Principles, Technology and Systems Application*. (Prentice-Hall, Englewood Cliffs, NJ, 1982).
- [19] W. G. J. H. M. van Sark, A. Meijerink and R. E. I. Schropp, in *Third Generation Photovoltaics*, edited by V. Fthenakis (InTech, 2012), [10.5772/39213](#).
- [20] M. Wolf, *Energ. Convers.* **11**, 63 (1971) [10.1016/0013-7480\(71\)90074-X](#).
- [21] T. Trupke, M. A. Green and P. Würfel, *J. Appl. Phys.* **92**, 1668 (2002) [10.1063/1.1492021](#).
- [22] B. S. Richards, *Sol. Energ. Mat. Sol. C.* **90**, 1189 (2006) [10.1016/j.solmat.2005.07.001](#).
- [23] J. Zhou, Y. Teng, S. Ye, X. Liu and J. Qiu, *Opt. Mater.* **33**, 153 (2010) [10.1016/j.optmat.2010.08.008](#).
- [24] J.-M. Meijer, L. Aarts, B. M. van der Ende, T. J. H. Vlugt and A. Meijerink, *Phys. Rev. B* **81**, 035107 (2010) [10.1103/PhysRevB.81.035107](#).
- [25] V. K. Malyutenko and V. V. Bogatyrenko, *Phys. Rev. B* **76**, 113201 (2007) [10.1103/PhysRevB.76.113201](#).
- [26] T. Trupke, M. A. Green and P. Würfel, *J. Appl. Phys.* **92**, 4117 (2002) [10.1063/1.1505677](#).
- [27] C. Strümpel, M. McCann, G. Beaucarne, V. Arkhipov, A. Slaoui, V. Švrček, C. del Cañizo and I. Tobias, *Sol. Energ. Mat. Sol. C.* **91**, 238 (2007) [10.1016/j.solmat.2006.09.003](#).
- [28] M. Haase and H. Schäfer, *Angew. Chem. Int. Edit.* **50**, 5808 (2011) [10.1002/anie.201005159](#).
- [29] N. Bloembergen, *Phys. Rev. Lett.* **2**, 84 (1959) [10.1103/PhysRevLett.2.84](#).
- [30] F. Auzel, *Chem. Rev.* **104**, 139 (2004) [10.1021/cr020357g](#).
- [31] W. Zou, C. Visser, J. A. Maduro, M. S. Pshenichnikov and J. C. Hummelen, *Nature Photonics* **6**, 560 (2012) [10.1038/nphoton.2012.158](#).
- [32] J. de Wild, A. Meijerink, J. K. Rath, W. G. J. H. M. van Sark and R. E. I. Schropp, *Energy Environ. Sci.* **4**, 4835 (2011) [10.1039/C1EE01659H](#).
- [33] B. M. van der Ende, L. Aarts and A. Meijerink, *Phys. Chem. Chem. Phys.* **11**, 11081 (2009) [10.1039/B913877C](#).
- [34] H.-Q. Wang, M. Batentschuk, A. Osvet, L. Pinna and C. J. Brabec, *Adv. Mater.* **23**, 2675 (2011) [10.1002/adma.201100511](#).
- [35] G. Conibeer, *Mater. Today* **10**, 42 (2007) [10.1016/S1369-7021\(07\)70278-X](#).
- [36] C. Zhang, Y. Yuan, S. Zhang, Y. Wang and Z. Liu, *Angew. Chem. Int. Edit.* **50**, 6851 (2011) [10.1002/anie.201100769](#).
- [37] A. Stepuk, D. Mohn, R. N. Grass, M. Zehnder, K. W. Krämer, F. Pellé, A. Ferrier and W. J. Stark, *Dent. Mater.* **28**, 304 (2012) [10.1016/j.dental.2011.11.018](#).
- [38] M. Nyk, R. Kumar, T. Y. Ohulchansky, E. J. Bergey and P. N. Prasad, *Nano Lett.* **8**, 3834 (2008) [10.1021/nl802223f](#).
- [39] M. Wang, C.-C. Mi, W.-X. Wang, C.-H. Liu, Y.-F. Wu, Z.-R. Xu, C.-B. Mao and S.-K. Xu, *ACS Nano* **3**, 1580 (2009) [10.1021/nn900491j](#).

- [40] Y. Yang, Q. Shao, R. Deng, C. Wang, X. Teng, K. Cheng, Z. Cheng, L. Huang, Z. Liu, X. Liu and B. Xing, *Angew. Chem. Int. Edit.* **51**, 3125 (2012) [10.1002/anie.201107919](#).
- [41] G. Tian, Z. Gu, L. Zhou, W. Yin, X. Liu, L. Yan, S. Jin, W. Ren, G. Xing, S. Li and Y. Zhao, *Adv. Mater.* **24**, 1226 (2012) [10.1002/adma.201104741](#).
- [42] T. J. Whitley, C. A. Millar, R. Wyatt, M. C. Brierley and D. Szebesta, *Electron. Lett.* **27**, 1785 (1991) [10.1049/el:19911110](#).
- [43] A. J. Silversmith, W. Lenth and R. M. Macfarlane, *Appl. Phys. Lett.* **51**, 1977 (1987) [10.1063/1.98316](#).
- [44] E. Downing, L. Hesselink, J. Ralston and R. Macfarlane, *Science* **273**, 1185 (1996) [10.1126/science.273.5279.1185](#).
- [45] B. Henderson and G. F. Imbusch, *Optical Spectroscopy of Inorganic Solids* (Oxford University Press Inc., New York, NY, 1989).
- [46] C. Strümpel, M. McCann, P. Fath, C. Del Canizo and I. Tobias, in 20th European Photovoltaic Solar Energy Conference (2005).
- [47] C. Strümpel, M. McCann and G. Hahn, in *EU PVSEC Proc.* (2008), pp. 645–647, [10.4229/23rdEUPVSEC2008-1DV.2.17](#).
- [48] X. Zhu and N. Peyghambarian, *Adv. Optoelectron.* **2010**, 501956 (2010) [10.1155/2010/501956](#).
- [49] M. J. F. Digonnet, *Rare-Earth-Doped Fiber Lasers and Amplifiers*, 2nd ed. (Marcel Dekker, Inc., New York, NY, 2001).
- [50] V. K. Bogdanov, “Energy exchange processes in erbium-doped fluoride glasses”, PhD thesis (Victoria University Melbourne, Australia, 1999).
- [51] R. M. Almeida and J. D. Mackenzie, *J. Chem. Phys.* **74**, 5954 (1981) [10.1063/1.441033](#).
- [52] S. Schweizer, L. W. Hobbs, M. Secu, J.-M. Spaeth, A. Edgar and G. V. M. Williams, *Appl. Phys. Lett.* **83**, 449 (2003) [10.1063/1.1593228](#).
- [53] S. Schweizer, L. W. Hobbs, M. Secu, J.-M. Spaeth, A. Edgar, G. V. M. Williams and J. Hamlin, *J. Appl. Phys.* **97**, 083522 (2005) [10.1063/1.1872193](#).
- [54] A. Shalav, B. S. Richards, T. Trupke, K. W. Krämer and H. U. Güdel, *Appl. Phys. Lett.* **86**, 013505 (2005) [10.1063/1.1844592](#).
- [55] M. Pollnau, P. J. Hardman, W. A. Clarkson and D. C. Hanna, *Opt. Commun.* **147**, 203 (1998) [10.1016/S0030-4018\(97\)00524-5](#).
- [56] S. R. Lüthi, M. Pollnau, H. U. Güdel and M. P. Hehlen, *Phys. Rev. B* **60**, 162 (1999) [10.1103/PhysRevB.60.162](#).
- [57] M. Pollnau, T. Graf, J. E. Balmer, W. Lüthy and H. P. Weber, *Phys. Rev. A* **49**, 3990 (1994) [10.1103/PhysRevA.49.3990](#).
- [58] M. Pollnau, D. R. Gamelin, S. R. Lüthi, H. U. Güdel and M. P. Hehlen, *Phys. Rev. B* **61**, 3337 (2000) [10.1103/PhysRevB.61.3337](#).
- [59] V. K. Bogdanov, D. J. Booth, W. E. K. Gibbs, J. S. Javorniczky, P. J. Newman and D. R. MacFarlane, *Phys. Rev. B* **63**, 205107 (2001) [10.1103/PhysRevB.63.205107](#).
- [60] V. K. Bogdanov, D. J. Booth and W. E. K. Gibbs, *J. Non-Cryst. Solids* **321**, 20 (2003) [10.1016/S0022-3093\(03\)00084-X](#).

- [61] V. K. Bogdanov, D. J. Booth and W. E. K. Gibbs, *J. Non-Cryst. Solids* **333**, 56 (2004) 10.1016/j.jnoncrysol.2003.09.052.
- [62] D. Chen, Y. Wang, Y. Yu, E. Ma and F. Liu, *J. Phys. Chem. Sol.* **68**, 193 (2007) 10.1016/j.jpccs.2006.10.009.
- [63] D. Chen, Y. Wang, E. Ma, Y. Yu and F. Liu, *Opt. Mater.* **29**, 1693 (2007) 10.1016/j.optmat.2006.09.002.
- [64] S. Fischer, B. Fröhlich, H. Steinkemper, K. W. Krämer and J. C. Goldschmidt, *Sol. Energ. Mat. Sol. C.* **122**, 197 (2014) 10.1016/j.solmat.2013.12.001.
- [65] C. A. v. Welsbach, *Monatsh. Chem. Verw. Tl.* **6**, 477 (1885) 10.1007/BF01554643.
- [66] S. Gagnon and T. Jefferson, *The Element Neodymium*, National Accelerator Facility - Office of Science Education, (2014) <http://education.jlab.org/itselemental/ele060.html>.
- [67] F. Szabadvary, in *Handbook on the Physics and Chemistry of Rare Earths*, Vol. 11, edited by J. K. A. Gschneidner and L. Eyring (Elsevier B. V., Amsterdam, The Netherlands, 1988), pp. 33–80, 10.1016/S0168-1273(88)11005-2.
- [68] National Risk Management Research Lab., *Rare Earth Elements: A Review of Production, Processing, Recycling, and Associated Environmental Issues*. Technical report EPA 600/R-12/572 (US Environmental Protection Agency, 2012).
- [69] B. G. Wybourne, *Spectroscopic Properties of Rare Earths* (John Wiley & Sons, Inc., New York, NY, 1965).
- [70] A. Langhamer, *The legend of Bohemian glass: a thousand years of glass-making in the heart of Europe* (Tigris, Zlín, Czech Republik, 2003), p. 273.
- [71] W. Seifritz, *Fusion Sci. Technol.* **20**, 295 (1992).
- [72] P. Scherrer, *Göttinger Nachrichten Math. Phys.* **2**, 1 (1918).
- [73] P. N. Prasad, *Nanophotonics* (John Wiley & Sons, Inc., Hoboken, NJ, 2004), 10.1002/0471670251.
- [74] U. Holzwarth and N. Gibson, *Nat. Nanotechnol.* **6**, 534 (2011) 10.1038/nnano.2011.145.
- [75] U. Skrzypczak, C. Pfau, C. Bohley, G. Seifert and S. Schweizer, *J. Non-Cryst. Solids* **363**, 205 (2013) 10.1016/j.jnoncrysol.2012.12.039.
- [76] W. Kraus and G. Nolze, *J. Appl. Crystallogr.* **29**, 301 (1996) 10.1107/S0021889895014920.
- [77] A. Haase and G. Brauer, *Z. Anorg. Allg. Chem.* **441**, 181 (1978) 10.1002/zaac.19784410120.
- [78] T. Gloriant, M. Gich, S. Suriñach, M. D. Baró and A. L. Greer, *Mater. Sci. Forum* **343-346**, 365 (2000) 10.4028/www.scientific.net/MSF.343-346.365.
- [79] J. W. Dunning, *Particle Growth in Suspensions*, edited by A. L. Smith (Academic Press, London, UK, 1973), pp. 3–28.
- [80] T. Suzuki, H. Kawai, H. Nasu, S. Mizuno, H. Ito, K. Hasegawa and Y. Ohishi, *J. Opt. Soc. Am. B* **28**, 2001 (2011) 10.1364/JOSAB.28.002001.
- [81] J. H. Choi, A. Margaryan, A. Margaryan and F. G. Shi, *J. Lumin.* **114**, 167 (2005) 10.1016/j.jlumin.2004.12.015.

- [82] H. Takebe, K. Yoshino, T. Murata, K. Morinaga, J. Hector, W. S. Brocklesby, D. W. Hewak, J. Wang and D. N. Payne, *Appl. Optics* **36**, 5839 (1997) [10.1364/AO.36.005839](#).
- [83] H. Takebe, Y. Nageno and K. Morinaga, *J. Am. Ceram. Soc.* **78**, 1161 (1995) [10.1111/j.1151-2916.1995.tb08463.x](#).
- [84] J. Lucas, M. Chanthanasinh, M. Poulain, M. Poulain, P. Brun and M. J. Weber, *J. Non-Cryst. Solids* **27**, 273 (1978) [10.1016/0022-3093\(78\)90130-8](#).
- [85] W. T. Carnall, P. R. Fields and K. Rajnak, *J. Chem. Phys.* **49**, 4424 (1968) [10.1063/1.1669893](#).
- [86] L. Wetenkamp, T. Westendorf, G. West and A. Kober, *Mater. Sci. Forum* **32-33**, 471 (1988) [10.4028/www.scientific.net/MSF.32-33.471](#).
- [87] H. H. Li, *J. Phys. Chem. Ref. Data* **9**, 161 (1980) [10.1063/1.555616](#).
- [88] J. C. M. Garnett, *Phil. Trans. R. Soc. Lond. A* **203**, 385 (1904) [10.1098/rsta.1904.0024](#).
- [89] C. F. Bohren and D. R. Huffman, *Absorption and Scattering of Light by Small Particles* (Wiley, Weinheim, Germany, 1998), [10.1002/9783527618156](#).
- [90] R. Caspary, *Applied Rare-Earth Spectroscopy for Fiber Laser Optimization* (Shaker, Aachen, Germany, 2003).
- [91] M. P. Shepilov, *Opt. Mater.* **30**, 839 (2008) [10.1016/j.optmat.2007.03.004](#).
- [92] M. P. Shepilov, personal communication, 2014.
- [93] F. Pellé and F. Auzel, *J. Alloy. Compd.* **300-301**, 131 (2000) [10.1016/S0925-8388\(99\)00743-4](#).
- [94] C. Pfau, "Low phonon energy glass ceramics for efficient rare-earth luminescence", PhD thesis (Martin Luther University Halle-Wittenberg, Germany, 2014).
- [95] T. Kushida, *Phys. Rev.* **185**, 500 (1969) [10.1103/PhysRev.185.500](#).
- [96] J. M. Pellegrino, W. M. Yen and M. J. Weber, *J. Appl. Phys.* **51**, 6332 (1980) [10.1063/1.327621](#).
- [97] D. Piatkowski and S. Mackowski, *Opt. Mater.* **34**, 2055 (2012) [10.1016/j.optmat.2012.04.007](#).
- [98] M. J. Weber, "Laser Program, Annual Report", in, Vol. 1, edited by L. W. Coleman, W. F. Krupke and J. R. Strack, UCRL-50021-80 (Lawrence Livermore National Laboratory, UC Livermore, 1980), pp. 2–328.
- [99] K. Binnemans, H. De Leebeeck, C. Görrler-Walrand and J. L. Adam, *Chem. Phys. Lett.* **303**, 76 (1999) [10.1016/S0009-2614\(99\)00216-X](#).
- [100] L. A. Riseberg and H. W. Moos, *Phys. Rev.* **174**, 429 (1968) [10.1103/PhysRev.174.429](#).
- [101] M. M. Mann and L. G. DeShazer, *J. Appl. Phys.* **41**, 2951 (1970) [10.1063/1.1659342](#).
- [102] B. Walsh, in *Advances in Spectroscopy for Lasers and Sensing*, edited by B. Di Bartolo and O. Forte (Springer, Amsterdam, The Netherlands, 2006), pp. 403–433, [10.1007/1-4020-4789-4_21](#).

- [103] W. T. Carnall, P. R. Fields and B. G. Wybourne, *J. Chem. Phys.* **42**, 3797 (1965) [10.1063/1.1695840](#).
- [104] W. T. Carnall, P. R. Fields and K. Rajnak, *J. Chem. Phys.* **49**, 4412 (1968) [10.1063/1.1669892](#).
- [105] A. A. Kaminskii, G. Boulon, M. Buoncristiani, B. D. Bartolo, A. Kornienko and V. Mironov, *Phys. Status Solidi A* **141**, 471 (1994) [10.1002/pssa.2211410228](#).
- [106] B. R. Judd, *Phys. Rev.* **127**, 750 (1962) [10.1103/PhysRev.127.750](#).
- [107] G. S. Ofelt, *J. Chem. Phys.* **37**, 511 (1962) [10.1063/1.1701366](#).
- [108] W. B. Fowler and D. L. Dexter, *Phys. Rev.* **128**, 2154 (1962) [10.1103/PhysRev.128.2154](#).
- [109] I. R. Mitchell, "A spectroscopic study of Nd³⁺ and Pr³⁺ doped fluorozirconate glass", PhD thesis (Victoria University Melbourne, Australia, 1999).
- [110] X. Qiao, X. Fan, J. Wang and M. Wang, *J. Non-Cryst. Solids* **351**, 357 (2005) [10.1016/j.jnoncrysol.2004.11.021](#).
- [111] U. Skrzypczak, C. Pfau, C. Bohley, G. Seifert and S. Schweizer, *J. Phys. Chem. C* **117**, 10630 (2013) [10.1021/jp312677u](#).
- [112] U. Skrzypczak, C. Pfau, C. Bohley, G. Seifert and S. Schweizer, *Dataset Pap. Phys.* **2013**, 236421 (2013) [10.1155/2013/236421](#).
- [113] J. Wan, L. Cheng, J. Sun, H. Zhong, X. Li, W. Lu, Y. Tian, B. Wang and B. Chen, *Physica B* **405**, 1958 (2010) [10.1016/j.physb.2010.01.051](#).
- [114] D. K. Sardar, R. C. Velarde-Montecinos and S. Vizcarra, *Phys. Status Solidi A* **136**, 555 (1993) [10.1002/pssa.2211360228](#).
- [115] W. F. Krupke, *IEEE J. Quantum Elect.* **7**, 153 (1971) [10.1109/JQE.1971.1076623](#).
- [116] W. F. Krupke, *IEEE J. Quantum Elect.* **10**, 450 (1974) [10.1109/JQE.1974.1068162](#).
- [117] M. J. Weber, D. C. Ziegler and C. A. Angell, *J. Appl. Phys.* **53**, 4344 (1982) [10.1063/1.331214](#).
- [118] R. Reisfeld, M. Eyal and C. K. Jørgensen, *J. Less-Common Met.* **126**, 187 (1986) [10.1016/0022-5088\(86\)90279-1](#).
- [119] K. Binnemans, D. Verboven, C. Görller-Walrand, J. Lucas, N. Duhamel-Henry and J. L. Adam, *J. Non-Cryst. Solids* **204**, 178 (1996) [10.1016/S0022-3093\(96\)00406-1](#).
- [120] R. Balda, J. Fernández, A. Mendioroz, J. L. Adams and B. Boulard, *J. Phys.: Condens. Matter* **6**, 913 (1994) [10.1088/0953-8984/6/4/011](#).
- [121] L. Wetenkamp, G. F. West and H. Többen, *J. Non-Cryst. Solids* **140**, 35 (1992) [10.1016/S0022-3093\(05\)80737-9](#).
- [122] R. D. Peacock, in *Structure and Bonding*, Vol. 22, edited by J. D. Dunitz, P. Hemmerich, J. A. Ibers, J. B. Neilands and R. J. P. Williams, Rare Earths (Springer, Berlin, Germany, 1975), pp. 83–122, [10.1007/BFb0116556](#).
- [123] Y. V. Orlovskii and T. T. Basiev and I. N. Vorob'ev and V. V. Osiko and A. G. Papashvili and A. M. Prokhorov, *Laser Phys.* **6**, 448 (1996).
- [124] M. J. Weber, *Phys. Rev. B* **8**, 54 (1973) [10.1103/PhysRevB.8.54](#).

- [125] D. E. McCumber, *Phys. Rev.* **134**, A299 (1964) 10.1103/PhysRev.134.A299.
- [126] W. J. Miniscalco and R. S. Quimby, *Opt. Lett.* **16**, 258 (1991) 10.1364/OL.16.000258.
- [127] R. M. Martin and R. S. Quimby, *J. Opt. Soc. Am. B* **23**, 1770 (2006) 10.1364/JOSAB.23.001770.
- [128] Z. Burshtein, *Opt. Eng.* **49**, 091005 (2010) 10.1117/1.3483907.
- [129] H. Yin, P. Deng, J. Zhang and F. Gan, *Mat. Lett.* **30**, 29 (1997) 10.1016/S0167-577X(96)00166-8.
- [130] M. J. F. Digonnet, E. Murphy-Chutorian and D. G. Falquier, *IEEE J. Quantum Elect.* **38**, 1629 (2002) 10.1109/JQE.2002.805111.
- [131] Y. Nageno, H. Takebe and K. Morinaga, *J. Am. Ceram. Soc.* **76**, 3081 (1993) 10.1111/j.1151-2916.1993.tb06612.x.
- [132] M. J. Weber, R. A. Saroyan and R. C. Ropp, *J. Non-Cryst. Solids* **44**, 137 (1981) 10.1016/0022-3093(81)90138-1.
- [133] C. K. Jørgensen and R. Reisfeld, *J. Less-Common Met.* **93**, 107 (1983) 10.1016/0022-5088(83)90454-X.
- [134] R. Reisfeld and C. K. Jørgensen, in *Handbook on the Physics and Chemistry of Rare Earths*, Vol. 9, edited by J. K. A. Gschneidner and L. Eyring (North-Holland, Amsterdam, The Netherlands, 1987), p. 187, 10.1016/S0168-1273(87)09004-4.
- [135] R. Reisfeld, *Ann. Chim. (Paris)* **7**, 147 (1982).
- [136] A. Naruse, Y. Abe and H. Inoue, *J. Ceram. Soc. Jpn.* **76**, 36 (1968) 10.2109/jcersj1950.76.870_36.
- [137] Y. C. Ratnakaram and A. V. Reddy, *J. Non-Cryst. Solids* **277**, 142 (2000) 10.1016/S0022-3093(00)00297-0.
- [138] C. Brecher, L. A. Riseberg and M. J. Weber, *Phys. Rev. B* **18**, 5799 (1978) 10.1103/PhysRevB.18.5799.
- [139] M. J. Weber, J. D. Myers and D. H. Blackburn, *J. Appl. Phys.* **52**, 2944 (1981) 10.1063/1.329034.
- [140] L. A. Riseberg and M. J. Weber, in *Progress in Optics*, Vol. 14, edited by E. Wolf (Elsevier, New York, NY, 1977), pp. 89–159, 10.1016/S0079-6638(08)70251-8.
- [141] L. A. Riseberg, W. B. Gandrud and H. W. Moos, *Phys. Rev.* **159**, 262 (1967) 10.1103/PhysRev.159.262.
- [142] P. Goldner and F. Auzel, *J. Appl. Phys.* **79**, 7972 (1996) 10.1063/1.362347.
- [143] J. A. Caird, W. T. Carnall and J. P. Hessler, *J. Chem. Phys.* **74**, 3225 (1981) 10.1063/1.441517.
- [144] R. R. Jacobs and M. J. Weber, *IEEE J. Quantum Elect.* **12**, 102 (1976) 10.1109/JQE.1976.1069101.
- [145] D. Piątkowski, *J. Non-Cryst. Solids* **353**, 1017 (2007) 10.1016/j.jnoncrysol.2007.01.013.
- [146] U. Skrzypczak, C. Pfau, G. Seifert and S. Schweizer, *J. Phys. Chem. C* **118**, 13087 (2014) 10.1021/jp5021033.
- [147] U. Skrzypczak, C. Pfau, G. Seifert and S. Schweizer, *Proc. SPIE* **9140**, 91400J (2014) 10.1117/12.2051764.

- [148] M. P. Hehlen, R. I. Epstein and H. Inoue, *Phys. Rev. B* **75**, 144302 (2007) [10.1103/PhysRevB.75.144302](#).
- [149] F. E. Auzel and F. Pellé, *Proc. SPIE* **3416**, 74 (1998) [10.1117/12.323402](#).
- [150] L. Gomes, A. F. H. Librantz and S. D. Jackson, *J. Appl. Phys.* **107**, 053103 (2010) [10.1063/1.3311561](#).
- [151] M. D. Shinn, W. A. Sibley, M. G. Drexhage and R. N. Brown, *Phys. Rev. B* **27**, 6635 (1983) [10.1103/PhysRevB.27.6635](#).
- [152] C. Pfau, U. Skrzypczak, B. Ahrens and S. Schweizer, *J. Phys.: Condens. Matter* **26**, 025406 (2014) [10.1088/0953-8984/26/2/025406](#).
- [153] T. Miyakawa and D. L. Dexter, *Phys. Rev. B* **1**, 2961 (1970) [10.1103/PhysRevB.1.2961](#).
- [154] T. F. Soules and C. B. Duke, *Phys. Rev. B* **3**, 262 (1971) [10.1103/PhysRevB.3.262](#).
- [155] R. Reisfeld, in *Structure and Bonding*, Vol. 22, edited by J. D. Dunitz, P. Hemmerich, J. A. Ibers, J. B. Neilands and R. J. P. Williams, Rare Earths (Springer, Berlin, Germany, 1975), pp. 123–175, [10.1007/BFb0116557](#).
- [156] F. Auzel, *Phys. Rev. B* **13**, 2809 (1976) [10.1103/PhysRevB.13.2809](#).
- [157] R. Reisfeld, in *Radiationless processes*, edited by B. DiBartolo and V. Goldberg (Springer, New York, NY, 1981), pp. 489–498, [10.1007/978-1-4613-3174-2_15](#).
- [158] C. B. Layne, W. H. Lowdermilk and M. J. Weber, *Phys. Rev. B* **16**, 10 (1977) [10.1103/PhysRevB.16.10](#).
- [159] S. Aasland and T. Grande, *Chem. Pap.* **52**, 21 (1998).
- [160] S. Berciaud, L. Cagnet and B. Lounis, *Phys. Rev. Lett.* **101**, 077402 (2008) [10.1103/PhysRevLett.101.077402](#).
- [161] J. L. Doualan, C. Maunier, D. Descamps, J. Landais and R. Moncorgé, *Phys. Rev. B* **62**, 4459 (2000) [10.1103/PhysRevB.62.4459](#).
- [162] F. Auzel and F. Pellé, *Phys. Rev. B* **55**, 11006 (1997) [10.1103/PhysRevB.55.11006](#).
- [163] J. M. F. van Dijk and M. F. H. Schuurmans, *J. Chem. Phys.* **78**, 5317 (1983) [10.1063/1.445485](#).
- [164] O. L. Malta and L. D. Carlos, *Quim. Nova* **26**, 889 (2003).
- [165] J. Koetke and G. Huber, *Appl. Phys. B* **61**, 151 (1995) [10.1007/BF01090936](#).
- [166] P. Le Boulanger, J.-L. Doualan, S. Girard, J. Margerie and R. Moncorgé, *Phys. Rev. B* **60**, 11380 (1999) [10.1103/PhysRevB.60.11380](#).
- [167] L. C. Courrol, E. P. Maldonado, L. Gomes, N. D. V. Jr., I. M. Ranieri and S. P. Morato, *Opt. Mater.* **14**, 81 (2000) [10.1016/S0925-3467\(99\)00111-1](#).
- [168] L. Fornasiero, T. Kellner, S. Kück, J. P. Meyn, P. E.-A. Möbert and G. Huber, *Appl. Phys. B* **68**, 67 (1999) [10.1007/s003400050587](#).
- [169] S. L. Oliveira, D. F. de Sousa, A. A. Andrade, L. A. O. Nunes and T. Catunda, *J. Appl. Phys.* **103**, 023103 (2008) [10.1063/1.2826908](#).
- [170] S. Fischer, H. Steinkemper, P. Löper, M. Hermle and J. C. Goldschmidt, *J. Appl. Phys.* **111**, 013109 (2012) [10.1063/1.3674319](#).

- [171] S. Fischer, A. Ivaturi, B. Fröhlich, M. Rüdiger, A. Richter, K. W. Krämer, B. S. Richards and J. C. Goldschmidt, *IEEE J. Photovolt.* **4**, 183 (2014) [10.1109/JPHOTOV.2013.2282744](#).
- [172] American Society for Testing and Materials (ASTM), *Terrestrial Reference Spectra for Photovoltaic Performance Evaluation*, tech. rep. ASTM G173-03(2012) (ASTM West, Conshohocken, PA, 2003), [10.1520/G0173-03R12](#).
- [173] M. A. Green and M. J. Keevers, *Prog. Optics* **3**, 189 (1995) [10.1002/pip.4670030303](#).
- [174] G. H. Dieke and H. M. Crosswhite, *Appl. Opt.* **2**, 675 (1963) [10.1364/AO.2.000675](#).
- [175] K. Tanimura, M. D. Shinn, W. A. Sibley, M. G. Drexhage and R. N. Brown, *Phys. Rev. B* **30**, 2429 (1984) [10.1103/PhysRevB.30.2429](#).
- [176] F. Steudel, S. Loos, B. Ahrens and S. Schweizer, *Proc. SPIE* **9140**, 91400I (2014) [10.1117/12.2052185](#).
- [177] J. F. Philipps, T. Töpfer, H. Ebdorff-Heidepriem, D. Ehrt and R. Sauerbrey, *Appl. Phys. B* **74**, 233 (2002) [10.1007/s003400200804](#).
- [178] G. Chen, C. Yang and P. N. Prasad, *Accounts Chem. Res.* **46**, 1474 (2013) [10.1021/ar300270y](#).
- [179] R. M. Martin and R. S. Quimby, *Appl. Phys. Lett.* **90**, 221104 (2007) [10.1063/1.2743953](#).
- [180] J. Hegarty and W. M. Yen, *Phys. Rev. Lett.* **43**, 1126 (1979) [10.1103/PhysRevLett.43.1126](#).
- [181] G. F. X. Strobl, G. LaRoche, K.-D. Rasch and G. Hey, in *High-Efficient Low-Cost Photovoltaics*, Vol. 140, edited by V. Petrova-Koch, R. Hezel and A. Goetzberger, Springer Series in Optical Sciences (Springer, Heidelberg, Germany, 2009), pp. 7–27, [10.1007/978-3-540-79359-5_2](#).
- [182] S. Bailey and R. Raffaele, in *Practical Handbook of Photovoltaics*, edited by A. McEvoy, T. Markvart and L. Castañer, 2nd ed. (Elsevier Advanced Technology, Oxford, UK, 2012), pp. 863–880, [10.1016/B978-0-12-385934-1.00027-1](#).
- [183] R. Trebino, K. W. DeLong, D. N. Fittinghoff, J. N. Sweetser, M. A. Krumbügel and B. A. Richmann, *Rev. Sci. Instrum.* **68**, 3277 (1997) [10.1063/1.1148286](#).
- [184] R. Trebino, *Frequency-Resolved Optical Gating: The Measurement of Ultrashort Laser Pulses* (Kluwer, Boston, MA, 2000).

ACKNOWLEDGEMENTS

Several people worked together with me on this work or contributed in another way. I would like to take this opportunity to thank...

- ★ PD Dr. Gerhard Seifert for patiently taking over my supervision. I am deeply grateful for the unlimited provision of help on all scientific matters.
- ★ Prof. Dr. Stefan Schweizer for giving the motivation of the work and for introducing me to his scientific subject.
- ★ Prof. Dr. Ralf B. Wehrspohn for remotely observing the dissertation and giving several inspiring directions in beforehand.
- ★ Prof. Dr. Jörg Schilling for reading my manuscript and for giving valuable advice.
- ★ Dr. Christian Bohley for the serious and passionate collaboration, as well as for thoroughly proof-reading approximately 38 000 words.
- ★ Dr. Charlotte Pfau und Dr. Bernd Ahrens for giving away their samples to me, which was highly appreciated.
- ★ Dr. Manuela Miclea for letting me benefit from her professional experience during my first scientific walking attempts.
- ★ My sons and wife for everything.

EIDESSTATTLICHE ERKLÄRUNG

Hiermit erkläre ich an Eides statt, dass ich die vorliegende Arbeit selbstständig und ohne Fremde Hilfe verfasst, keine anderen als die angegebenen Quellen und Hilfsmittel benutzt habe, und, dass alle Stellen der Arbeit, die wörtlich oder sinngemäß aus anderen Quellen übernommen wurden, als solche kenntlich gemacht sind. Diese Dissertation wurde bislang an keiner weiteren Institution vorgelegt. Es handelt sich um den ersten Promotionsversuch.

H. Ulrich Skrzypczak
Halle (Saale), den 15. Juli 2014

Ulrich Skrzypczak

Lebenslauf

■ Persönliches

Geburtsdatum 17.12.1984
Geburtsort Stralsund
Familienstand verheiratet, zwei Söhne

■ Schulausbildung

1999–2004 **Internatsgymnasium**, *Landesschule Pforta*, Schulpforte,
nach bestandener Aufnahmeprüfung naturwissenschaftlicher Zweig. Abitur (Note 2,3).

■ Studium

2004–2009 **Studium**, *Medizinische Physik*, Martin-Luther-Universität Halle-Wittenberg.
2009 **Diplomprüfungen**, Experimentelle Physik (Note 1,3), Theoretische Physik (Note 1,3), Wahlpflichtfach Nichtlineare Optik (Note 1,3) und Medizinische Strahlenphysik (Note 2,0).
2009 **Diplomarbeit**, *FG für Optik und zeitaufgelöste Spektroskopie*, „Nichtlineare optische Spektroskopie an biologischen Geweben“ (Note 1,0), Bereich Femtosekundenlaserbasierte refraktive Hornhautchirurgie.
Betreuung Prof. Dr. Heinrich Graener und Prof. Dr. Franz Fankhauser

■ Wissenschaftliche Arbeit

2006–2007 **Wiss. Hilfskraft**, *Institut für Analysis*, Prof. Dr. Siegfried Carl.
Seminare zu Analysis I-II
2007–2008 **Wiss. Hilfskraft**, *Institut für Physik*, Prof. Dr. Heinrich Graener, FG Optik.
Veränderungen von Silbernanopartikeln in Gläsern durch Bestrahlung mit Femtosekundenlasern, optische Spektroskopie, Programmierung, Konstruktion Messaufbauten
2008 **Wiss. Hilfskraft**, *Institut für Physik*, JProf. Dr. Jan Kantelhardt, Theoretische Physik.
Softwaregestützte Interpretation von medizinischen Schlafdaten zur Langzeitkorrelationen
2008 **Wiss. Hilfskraft**, *Institut für Physik*, Prof. Dr. Jamal Berakdar, Theoretische Physik.
Tutor Mathematische Physik für Studienanfänger

- 2009–2014 **Wiss. Mitarbeiter**, *Zentrum für Innovationskompetenz SiLi-nano*, Prof. Dr. Stefan Schweizer und PD Dr. Gerhard Seifert, Nachwuchsgruppe Light-to-Silicon.
Zeitaufgelöste Spektroskopie von Selten-Erdionen in Gläsern und Glaskeramiken, nichtlineare optische Spektroskopie
- 2015 **Promotion**, “*Rate equation analysis of nanocrystal-enhanced upconversion in neodymium-doped glasses*”, zum Dr. rer. nat. (summa cum laude).

Lehrtätigkeit

- WS08 Tutor Mathematische Physik für Studienanfänger
SS10 Physikalisches Grundpraktikum für Naturwissenschaftler
WS10 Übung zur Vorlesung Experimentalphysik für Biologen
SS11 Betreuung 2 Studenten im Rahmen ihrer Bachelorarbeiten Physik
SS11 Physikalisches Grundpraktikum für Pharmazeuten
WS11 Übung zur Vorlesung Experimentalphysik für Biologen
SS13 Betreuung 1 Student im Rahmen der Bachelorarbeit Physik
WS13 Betreuung 3 Studenten im Rahmen ihrer Masterarbeiten Physik
SS14 Physikalisches Grundpraktikum für Pharmazeuten
WS14 Betreuung 1 Student im Rahmen der Bachelorarbeit Physik
WS14 Betreuung 1 Student im Rahmen der Masterarbeit Physik

Eigene Konferenzbeiträge

- 2014 **SPIE Photonics Europe 2014**, *Brüssel*, Rate Equation Analysis of Nanocrystal-Enhanced Upconversion in Neodymium-Doped Glass Ceramics, Vortrag.
- 2012 **8th International Conference on Luminescent Detectors and Transformers of Ionizing Radiation (LUMDETR)**, *Halle (Saale)*, Optical properties of Nd³⁺ in ZBLAN containing BaCl₂ nanocrystals of different sizes, Poster.
- 2011 **DPG-Frühjahrstagung Kondensierte Materie**, *Dresden*, z-Scan characterization of zwitterionic chromophores for optoelectronic switching, Vortrag.
- 2010 **7th International Conference on Photo-Excited Processes and Applications (ICPEPA-7)**, *Kopenhagen*, z-Scan characterization of zwitterionic chromophores for optoelectronic switching, Vortrag.
- 2010 **DPG-Frühjahrstagung Kondensierte Materie**, *Regensburg*, Time-resolved optical spectroscopy on Er-doped fluorozirconate-based glasses for efficient up-conversion, Vortrag.
- 2009 **Conference on Lasers and Electro-Optics (CLEO)**, *München*, Anisotropic non-linear optical properties of metal nanocomposite glass, Poster.

Publikationen

- U. Skrzypczak, G. Seifert und S. Schweizer, "Highly Efficient and Broadband Upconversion of NIR Sunlight with Neodymium-Doped Glass Ceramics", *Adv. Opt. Mater.* **3**, (invited article), 541 (2015).
- U. Skrzypczak, C. Pfau, G. Seifert und S. Schweizer, "Comprehensive rate equation analysis of upconversion luminescence enhancement due to BaCl₂ nanocrystals in neodymium-doped fluorozirconate-based glass ceramics", *J. Phys. Chem. C* **118**, 13087 (2014).
- U. Skrzypczak, C. Pfau, G. Seifert und S. Schweizer, "Rate Equation Analysis of Nanocrystal-Enhanced Upconversion in Neodymium-Doped Glass Ceramics", *Proc. SPIE* **9140**, 91400J (2014).
- C. Pfau, U. Skrzypczak, B. Ahrens und S. Schweizer, "Multiphonon relaxation in rare-earth doped fluorozirconate-based glasses containing BaCl₂ nanocrystals", *J. Phys.: Condens. Matter* **26**, 025406 (2014).
- U. Skrzypczak, C. Pfau, C. Bohley, G. Seifert und S. Schweizer, "Influence of BaCl₂ nanocrystal size on the optical properties of Nd³⁺ in fluorozirconate glass", *J. Phys. Chem. C* **117**, 10630 (2013).
- U. Skrzypczak, C. Pfau, C. Bohley, G. Seifert und S. Schweizer, "Judd-Ofelt calculations for Nd³⁺-doped fluorozirconate-based glasses and glass ceramics", *Dataset Pap. Phys.* **2013**, 236421 (2013).
- U. Skrzypczak, C. Pfau, C. Bohley, G. Seifert und S. Schweizer, "Particle size monitoring of BaCl₂ nanocrystals in fluorozirconate glasses", *J. Non-Cryst. Solids* **363**, 205 (2013).
- C. Pfau, U. Skrzypczak, M. Miclea, C. Bohley, P.-T. Miclea u. a., "Low phonon energy BaCl₂ nanocrystals in Nd³⁺-doped fluorozirconate glasses and their influence on the photoluminescence properties", *Mater. Res. Soc. Symp. Proc.* **1404**, mrsf11/1404/w02/10 (2012).
- M. Miclea, U. Skrzypczak, F. Fankhauser, S. Faust, H. Graener u. a., "Applanation-free femtosecond laser processing of the cornea", *Biomed. Opt. Express* **2**, 534 (2011).
- U. Skrzypczak, M. Miclea, A. Stalmashonak, B. Ahrens, B. Henke u. a., "Time-resolved investigations of erbium ions in ZBLAN glass and glass ceramics", *Phys. Status Solidi C* **8**, 2649 (2011).
- U. Skrzypczak, G. V. M. Williams, M. Miclea, D. Bhuiyan, S. Janseens u. a., "Z-scan characterization of zwitterionic chromophores for optoelectronic switching", *Appl. Phys. A* **104**, 947 (2011).
- M. Miclea, U. Skrzypczak, S. Faust, F. Fankhauser, H. Graener u. a., "Nonlinear refractive index of porcine cornea studied by z-scan and self-focusing during femtosecond laser processing", *Opt. Express* **18**, 3700 (2010).
- A. Stalmashonak, G. Seifert, A. A. Unal, U. Skrzypczak, A. Podlipensky u. a., "Toward the production of micropolarizers by irradiation of composite glasses with silver nanoparticles", *Appl. Opt.* **48**, 37 (2009).